Dissertation
submitted to the
Combined Faculties for the Natural Sciences and for Mathematics
of the Ruperto-Carola University of Heidelberg, Germany
for the degree of
Doctor of Natural Sciences

	presented by
Diplom-Physiker:	**Samo Fišinger**
born in:	**Maribor**
	Oral examination: 17.12. 2003

Mechanical Properties of Individual Molecules:

An Interface between the Structure and the Function of the Molecules

Referees: Prof. Dr.rer.nat. Bogdan Povh
Prof. Dr.rer.nat. Markus Sauer

Die optische Pinzette mit einer 3D Positionsdetektion wurde zur Untersuchung mechanischer Eigenschaftem individueller Moleküle benutzt. Die Moleküle Avidin und Biotin wurden als ein Modelsystem zum etablieren unserer Methode hergenommen. Die optische Pinzette ermöglicht einerseits eine genaue Positionierung der Beads an der Oberfläche und andererseits eine Definition der lokalen Randbedingungen für die Reaktion. Unter diesen experimentellen Bedingungen wurde die mitllere zum Binden des Beads an die Oberfläche benötigte Zeit als Funktion der Dichte von Biotin an der Oberfläche gemessen. Ein auf Diffusion basiertes Modell wurde benutzt um aus der gemessenen Reaktionszeit die effektive Grösse der molekularen Bindungszentren abzuschätzen. Die auf diese Weise abgeschätzte Grösse der molekularen Zentren stimmt mit der Grösse eines einzelnen Bovine Serum Albumin Moleküls überein. Die lateralen Schwankungen gebundener Beads wurden auch zur Karakterisierung der Bindung zwischen dem Bead und der Oberfläche benutzt. Es war möglich zwischen einzelnen und mehrfachen molekularen Bindungen zu unterscheiden. Die gleiche Methode wurde auch zur Untersuchung mechanischer Eigenschaften des SNARE-Komplexes benutzt. Der SNARE-Komplex besteht aus drei Proteinen: syntaxin, synaptobrevin und SNAP-25. Die mechanischen Eigenschaften der Wechselwirkungen zwischen einzelnen Bauteilen des SNARE-Komplexes wurden gemessen und analysiert. Insgesamt wurden vier Kombinationen der SNARE-Proteine untersucht. Der molekulare Bindungsassay zeigte qualitative Unterschiede zwischen verschiedenen molekularen Wechselwirkungen. Insbesondere wurde bei der Wechselwirkung zwischen zwei syntaxin Molekülen und einem SNAP-25 Molekül ein einzigartiges Muster beobachtet: ein kontinuierliches Abnehmen der lateralen Positionsfluktuationen wurde von einer Rotation begleitet. Diese spiralenförmige Dynamik wurde als Formation eines individuellen SNARE-Komplexes interpretiert.

Optical tweezers with a 3D position detection were used to investigate the mechanical properties of individual molecules. The molecular receptor-ligand pair of avidin and biotin was used as a model system to establish our technique. Optical tweezers created the possibility to position the microsphere into close proximity of the surface and to define the local boundary conditions for the interaction. Under these experimental conditions we measured the average binding time of the bead to the surface as a function of the density of biotin on the surface. A diffusion based model was used to estimate the effective size of the molecular binding center from the average reaction time. The size of the molecular binding center as determined by our method is in good agreement with the size of an individual Bovine Serum Albumin molecule. The lateral position fluctuations of the bound bead were also used to determine the type of the contact. It was possible to distinguish between individual and multiple molecular bonds. The same method was applied to the study of mechanical properties of the SNARE-complex. The SNARE-complex consists of three proteins: syntaxin, synaptobrevin and SNAP-25. We measured and analyzed the mechanical properties of the interactions between four combinations between the building blocks of the SNARE-complex. Altogether, four different protein combinations were measured. The molecular binding assay showed qualitative differences between different molecules. In particular, the interaction between two syntaxin molecules and a single SNAP-25 molecule showed a unique pattern: a continuous decrease in lateral position fluctuations was accompanied by a rotation. This spiralling was interpreted in terms of an individual SNARE-complex formation.

For my family.

Contents

Chapter 1

Introduction

Biophysics is at the interface between biology and physics. Although the goal of any scientific field is to clarify certain fundamental questions, every scientific discipline approaches the question in a different way. The difference in the nature of the pursued scientific question can be so huge that it makes any kind of comparison impossible. On the other hand, if the differences are not too divergent, it might be possible to find a way for the integration of seemingly different scientific worlds and arrive at a new scientific insight.

In biology the central aim is to describe and characterize biochemical processes which are essential for living organisms. On the one hand, the results are often descriptive because of the difficulty in constructing and performing such experiments which would yield high data output. On the other hand, there are many essential parameters, which have to be simultaneously determined.

Modern molecular biology is typically performed on experimental length scales of the cell, *i.e.* on a μm length scale. A great experimental challenge consists in the construction of experiments in order to obtain more detailed information about the structure and the function of molecules. For example, research on molecular structure needs a spatial resolution on the order of $\mathring{A}$. This is achieved by x-ray crystallography or nuclear magnetic resonance, where the measured signal is averaged over an ensemble of molecules. The resulting structure provides a temporal snapshot of the molecular state.

Physics is a scientific discipline which is concerned with conceptual and quantitative level of description. Mathematics is a suitable language for scientific model description which has been widely adopted in physics. The aim in describing a natural phenomenon in these terms is to use as few independent

parameters as possible. Since biological systems are very heterogenous it is a great challenge to find a mathematical description which reflects this complex behavior.

Measurements performed on ensembles of molecules have provided amazing amount of information and insight into various phenomena. The molecular structure of proteins has brought significant insight into the function of protein molecules. Calorimetric methods have given very good estimations about the binding affinities for different molecules. These achievements have been accomplished despite the fact, that physical parameters in these measurements are averaged over very many molecules.

Certain physical quantities cannot be measured in an ensemble of molecules in solution. The most prominent among these parameters is definitely *force*. In general, mechanical properties of molecules cannot be determined and manipulated in a measurement performed on an ensemble of molecules.

The structure of the proteins is believed to determine the function of the molecule completely. Although there are many possible conformations which a protein can adopt the protein adopts a single final three-dimensional structure. The search for a single three-dimensional structure is referred to as the *protein folding problem* [26]. The reaction might be kinetically biased if the protein is following some well defined pathway on the energy landscape. However, a theory of protein folding which is based on general consensus is not yet available.

The interpretation of the data which were obtained from a measurement on an ensemble of molecules is based on certain assumptions about the molecular composition of the system. Another question about the role of molecular fluctuations - about the relationship between molecular fluctuations and molecular function - is then raised. This type of questions can be addressed within the framework of experiments which allow for resolution of individual molecules.

Individual molecules can also be viewed as ultimate components of molecular biology. They act as molecular machines which carry out specific tasks. Naturally, the question about the mechanism which is underlying this highly specific molecular recognition processes comes to mind.

In a typical cell there are several tens of thousands species of molecules which have to interact in a very specific manner. Because of intense molecu-

lar crowding, high heterogeneity and nonlinear local geometrical constraints one can ask what mechanism enables this marvellous cellular clockwork to function so precisely. Therefore, detailed knowledge about mechanical properties of individual molecules might bring important contribution to the understanding of the whole cellular organism.

In contrast to *in vitro* bulk experiments, intercellular space does not contain only dissolved protein molecules. There are also other structural elements, such as membranes, which determine the local cellular geometry. Experiments performed on the bulk of protein molecules demand a purified sample of molecules. The behavior of a protein molecule in the vicinity of a surface may significantly differ from its behavior in bulk solution. With a highly interwoven cellular structure, which consists of several organelles, it appears very probable that protein surface interactions play an important role in the cell.

The most prominent cellular structure where the surface interactions play a fundamental role are certainly lipid membranes, which contain proteins. These membrane proteins are mobile and are able to organize into clusters, e.g. *rafts*. Membrane proteins can perform various functions: signal transduction, molecular pumping, channelling through the membrane, etc. Although molecular components of the interactions are well known, it is often unclear what kind of mechanism is responsible for a given interaction. For example, it has been proposed that the SNARE complex plays a central role during the fusion process [35]. Although the structure of the molecular complex is well known it is not yet clear if the formation of the SNARE complex can exert necessary force to cause the membrane fusion.

In summary, there are many biological phenomena which are still lacking in proper understanding. Because of many independent degrees of freedom such systems display high levels of complexity. Therefore, detailed understanding of individual components is necessary before a better general picture can be drawn.

Chapter 2

Aim of the Thesis

The goal of the thesis is to establish a novel experimental technique to measure mechanical properties of individual biomolecules. The experimental apparatus is based on the idea of optical tweezers with a three dimensional position detection. Thermal position fluctuations of a microscopic particle are used to measure the mechanical properties of a molecular contact which is formed between the two surfaces.

Optical tweezers open two new experimental possibilities. First, thermal position fluctuations can be measured with a very high precision. From these measurements one can infer about the mechanical properties of an individual molecule. Second, this experimental technique allows also for mechanical manipulations on individual molecules. For example, by applying *a force* to pull on an individual molecular complex, one can in principle obtain information about the energy landscape governing the interaction between the molecules. Essentially, this means that one can define new reaction coordinates at the level of individual molecules.

The thesis has been divided into three parts: I *The Cell*, II *Thermally Activated Phenomena*, III *Experimental Procedures and Results*. This structure has been chosen because I felt it suits best to the interdisciplinary requirements of my work. In particular, I attempted to make it readable for physicists, chemists and biologists.

Therefore, an introduction to *the cell* is given in the first part of the thesis. This part is divided into two conceptual blocks: proteins and membranes. Proteins are defined and their structures are classified. The relationship between structure of a protein and its function is outlined in detail. The question of how a protein can find the final conformation in a relatively short amount

of time, known as the *protein folding problem*, is also addressed. Membrane biophysics represents the other half of the inner workings of the cell. They represent a locally two dimensional system. The properties of proteins studied in solution can differ from those of proteins studied in the presence of a membrane. Membrane fusion requires also proteins. However, it is still unclear at present stage what kind of molecular mechanism can explain the fusion process. There are different biophysical models which have been proposed to explain this phenomenon.

Experiments on individual biomolecules can be performed in aqueous solution. Thermal fluctuations play a fundamental role on these time and length scales and one has to introduce a proper theoretical framework to classify these phenomena. Part 4 of my thesis is concentrated towards an introduction of the relevant theoretical descriptions. An introduction to different forms of the Langevin equation is given in section 4.1. Also, a model for diffusion controlled reactions is developed in section 4.2. The application of this model is discussed in experimental part of the thesis in section 7.1.4.

Part III of the thesis is dedicated to the experiments. A description of experimental techniques and procedures which were developed during my thesis is given in chapter 6. Chapter 7 describes the experiments which were performed on individual molecules.

In section 6.1 I describe optical tweezers with a three dimensional position detection system (PFM). This is followed by the description of individual components in our experimental setup and those physical principles which are fundamental to the functioning of optical tweezers. Section 5.1 deals with the emergence of optical forces in a single gradient laser trap. In section 6.2 there is a description of the position detection system whose calibration is explained in section 6.3. Finally, I conclude the chapter with the experimental test for the stability of our experimental setup in section 6.4. It is shown that the mechanical stability of the position detection system is below 5nm on the time scale of several minutes. Such an accuracy is sufficient for the experiments with individual molecules which are described in the following sections.

In section 7.1 I introduce the molecular model system which was used to establish the experimental technique. First, a procedure for specific molecular surface preparation was developed. Furthermore, this procedure has been refined to show a quantitative test for the molecular specificity of the binding reaction in section 7.1.4 which is based on a prediction from mathematical model developed in section 4.2. Finally, in section 7.1.6 I show the results

which were interpreted in terms of *mapping of binding sites on an individual protein*. This section also describes the experiments where an individual avidin-biotin bond was repeatedly formed and ruptured.

Section 7.2 is dedicated to the SNARE complex. This section is opened with a general introduction to the function and structure of the SNARE complex during the membrane fusion process. It is followed by a description of experimental procedures for molecular sample preparation in section 7.2.1. The experimental results are presented in section 7.2.2 and the last section deals with the results which point towards a direct observation of an individual SNARE complex formation.

Summary and Discussion can be found in chapter 8.

Part I

The Cell

Chapter 3

Cell Constituents and their Interactions

The cell is an essential building block of plants and animals. Generally, there are two types of cells: prokaryotic and eukaryotic. The main difference between the two types is manifested in the order of cell organization and complexity. In general prokaryotic cells display much less internal structure than eukaryotic ones, the main difference between the two consisting in the presence of a nucleus in the latter type [2]. Due to the utmost importance of eukaryotic cells in current biological research I will concentrate on the description of their constituents.

Every cell is bounded by a lipid membrane. The interior of the cell consists of different membrane-bounded organelles and the cytosol. Among the most prominent membrane-bounded organelles is the cell nucleus. It contains most of the DNA molecule within the cell and serves as a store of genetic information.

Energy requirements of the cell are satisfied by mitochondria. Its very distinct structure, as revealed by electron microscopy, is marked by a folded inner membrane with large accessible surface. In the interior of mitochondria the energy is extracted from food molecules by oxidation in order to produce ATP (adenosine triphosphate) which serves as basic fuel for biochemical processes. Byproduct of this reaction is CO_2. In addition, mitochondria contain their own DNA and are able to replicate independently.

This holds also for chloroplasts which can be found only in cells of plants and algae. They show even more complicated structure than mitochondria and also function as energy producers. However, they are able to extract en-

ergy directly from the sun. Light is converted by a molecule called chlorophyll into ATP and oxygen is released as a waste product.

Besides the above mentioned organelles there are other intracellular compartments created by internal membranes in the cytoplasm. Their function is mainly concerned with the import of raw materials and the export of waste products. The endoplasmic reticulum (ER) is a very extended structure. Most of the material destined for secretion is made there. Golgi apparatus is involved in biochemical modification of materials. Lysosomes and peroxisomes are smaller membrane-bound organelles and act as containers for certain reactions. Transport of materials among different single membrane-bounded organelles is accomplished by vesicles.

The largest single compartment in the cell is certainly the cytosol. It can be defined as the entity which remains when all membrane-bound compartments have been removed from the cell. Its physico-chemical structure approaches more a concentrated aqueous gel than that of a simple solution. It contains a high concentration of large and small molecules. It is here that most biochemical reactions occur. The most important synthetic aspect is the production of proteins. The entities responsible for it are large molecules called ribosomes. A part of cytosol is highly structured into filaments and is called cytoskeleton. There are two major types of filaments: actin and microtubules. Actin filaments are thinner polymers consisting of actin proteins, Microtubules emerge as polymerized filaments from proteins called tubulin. Main function of the cytoskeleton is to maintain and change the shape of the cell, guide its movements and define mechanical strength. It is the most straightforward manifestation of mechanical properties of polymers directly relevant to cell function.

The hereditary information is stored in the DNA molecule. During the phase of transcription the double helix opens up and the base sequence of each strand is transcribed to the messenger RNA (mRNA). Single stranded mRNA from the cell nucleus is then transported to ribosomes located in the cytosol. The ribosome consists of tRNA and rRNA. rRNA is responsible for the three dimensional structure of the ribosome. Hence its name: "the structural RNA". It takes over the difficult task of mechanically fitting the mRNA to tRNA. Finally, tRNA translates the information encoded in the mRNA into amino acids.

There are 20 different types of amino acids which serve as building blocks

for proteins. Proteins carry out a number of fundamental functions in the cell. Considering the enormous diversity of proteins, closely packed in a very small volume within the cell, it is astonishing how they manage to carry out their specific tasks. The current understanding of molecular cellular mechanisms assumes that the three dimensional structure of the proteins is responsible for the specificity of molecular interactions.

3.1 Protein structures

Protein structures can be classified according to their complexity into four different categories: primary-, secondary-, tertiary-structure and higher levels. There are several physical forces, mainly non-covalent in nature, which determine the final structure of the protein. Although these forces can be ultimately understood in terms of electrostatic forces [32, page 11], it is common to classify them into seemingly different phenomena. The reason for this being the inability to solve the Schrödinger equation for such complex systems, which is discussed further in Section 3.2.

In this Section I give definitions for the above mentioned classes of protein structures. A more detailed description can be found elsewhere [18, 59, 15].

3.1.1 Primary structure

Amino acids are connected into a polypeptide chain by the peptide bond. The peptide bond is a covalent C-N bond (see Figure 3.1).The sequential order of the amino acids in the peptide chain is being referred to as the *primary structure*.

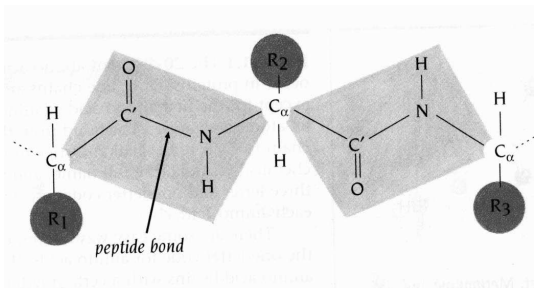

Figure 3.1: The peptide bond. It connects individual amino acid units covalently into a polypeptide chain. The peptide bond is formed when the α-carboxyl group of one amino acid is joined with the α-amino group of another amino acid. The result of the reaction is a chain connected by a covalent bond as shown in the picture above. The byproduct of the reaction is one water molecule per one peptide bond.

The polypeptide backbone can rotate around the axis defined by the covalent bonds between backbone atoms. There are only two angles which need to be specified per peptide unit. The rotation around the peptide bond between a nitrogen and a carbon atom (C-N) is defined by the angle ϕ. The

other possible rotation of the backbone can take place between the two carbon atoms (C_α-C') and is defined by the angle ψ (see Figure 3.2).

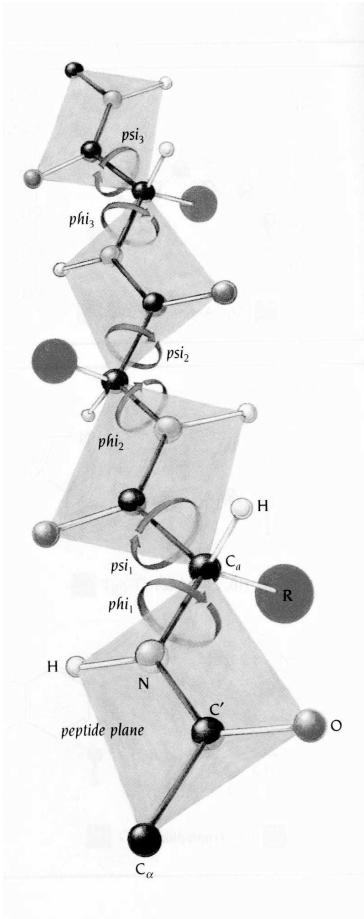

Figure 3.2: Polypeptide backbone. Schematically representing the degrees of freedom for a polypeptide backbone. The notation for carbon atoms C_α and C' denotes their relative position along the polypeptide chain.

3.1.2 Secondary structure

One level higher in the hierarchical classification of protein structures there is *secondary structure*. The elements belonging to this class are spatially well defined structures of the backbone. More specifically, the dihedral angles of the backbone, ϕ and ψ, can occupy only well defined values [59]. There are several types of secondary structure elements. The most frequently appearing in proteins is α-Helix. More seldom, but still abundantly present, is the

β-sheet. The allowed values for backbone dihedral angles in these secondary structure elements are shown in a 2-D map (see Figure 3.3 on page 16). Also present, though very rare, are *reverse turns*, 3_{10}- and π-Helices.

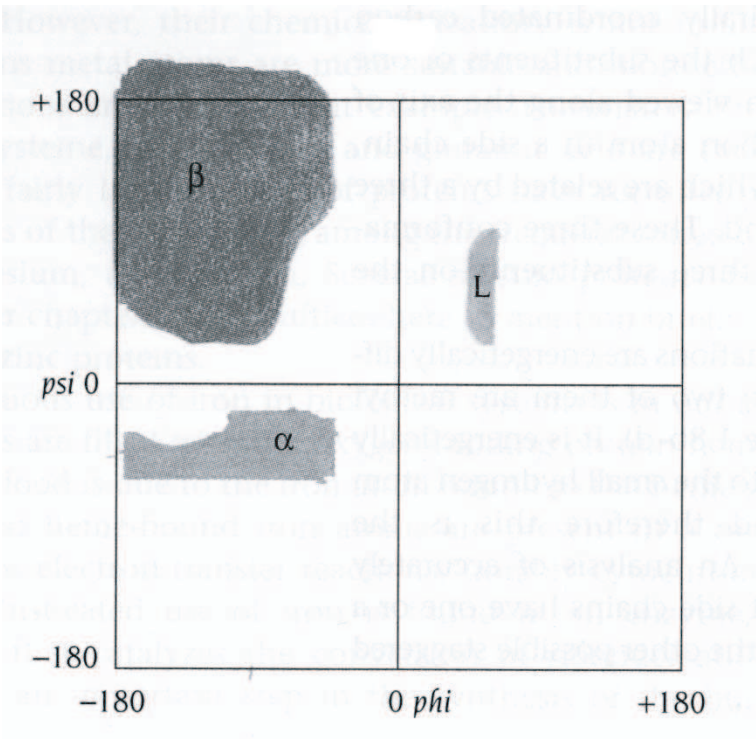

Figure 3.3: Ramachandran plot. The two dimensional graph shows the allowed regions for backbone dihedral angles ϕ and ψ. Each region is labelled by its corresponding structural element: α-helix, β-sheet and **L** for left-handed α-helix.

3.1.3 α-Helix

The emergence of an α-helical structure can be understood as a phase transition between an unfolded random-coil state and the α-helical state [23]. The theoretical description of the Helix-Coil transition is based on a modified *Ising model* known also as the *Zimm-Bragg* model [59, pages 254-260]. The main assumption here is that a nucleus of at least four neighboring amino acids spontaneously and cooperatively jumps from the random-coil state into the α-helical state mainly due to emergent hydrogen bonds. Finally, the nucleus is extended to a full length α-helix by additionally formed hydrogen bonds as shown in Figure 3.4.

Although the above theory has been constructed for homopolymeric peptide chains, it readily captures essential features of α-helical polypeptide chains. In order to achieve a better description one has to take into consideration further energetic contributions which naturally arise in heteropolymeric polypeptide chains (see for example [23, 39, 48, 49, 50, 51, 16]).

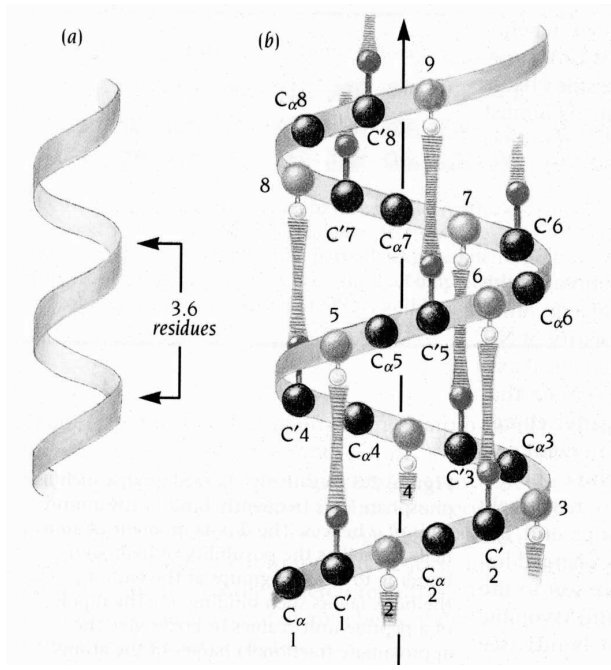

Figure 3.4: α-Helix. The illustration (a) shows the basic α-helical configuration of the backbone dihedral angles. A segment of 3.6 residues is needed to achieve a full 2π rotation around the vertical axis. (b) The hydrogen bond is being formed between one amino acid and the fourth next one along the polypeptide chain. This gives rise to the typical geometry of an α-helix. Dark spheres represent carbon atoms, bright spheres stand for nitrogen atoms and small spheres, with springs attached, show hydrogen atoms which participate in hydrogen bonds.

3.1.4 β-sheet

This structural element is also, similarly to the α-helix, energetically stabilized through mainly hydrogen bonds. The main difference between the two elements consists in their respective geometrical architecture. In β-sheets, hydrogen bonds can be formed between pairs of amino acids which are situated very far apart along the polypeptide chain. The consequence of such *global interactions* is lesser stability of β-sheets.

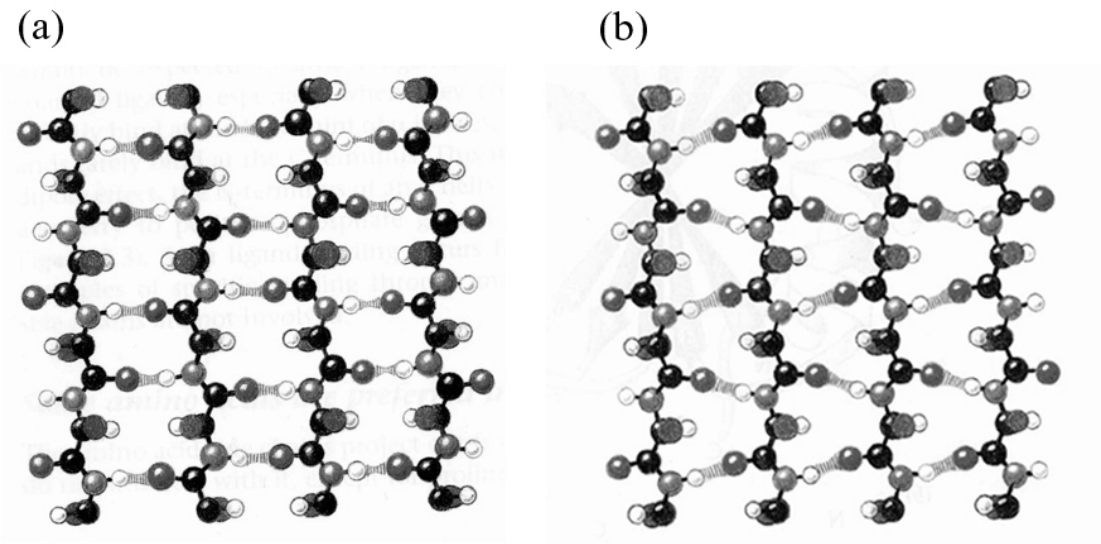

Figure 3.5: β-sheets. The neighboring amino acids in the three dimensional structure of a β-sheet are separated very far apart along the polypeptide chain. There are two geometrical configurations which enable stabilizing hydrogen bond interactions. (a) A parallel β-sheet. (b) An antiparallel β-sheet.

3.1.5 Tertiary structure

The tertiary structure of a protein consists of several interconnected secondary structure elements. Such structural units are usually responsible for biologically specific functions. They are also commonly referred to as *protein domains*.

3.1.6 Higher Levels

Globular proteins are made of several domains and are able to fulfil different biological functions in the cell. Figure 3.6 depicts the three dimensional structure of an enzyme. One can clearly see the composition of several identical elements of well defined tertiary structure.

In summary, amino acids are the building blocks of proteins. They are covalently connected through the peptide bond to form polypeptide chains. The hydrogen bond is the major force directing the geometry of various structural elements. Its relative weakness is especially convenient for the architecture of biological molecules. It enables fast creation and decomposition of structural elements participating in dynamic biological processes.

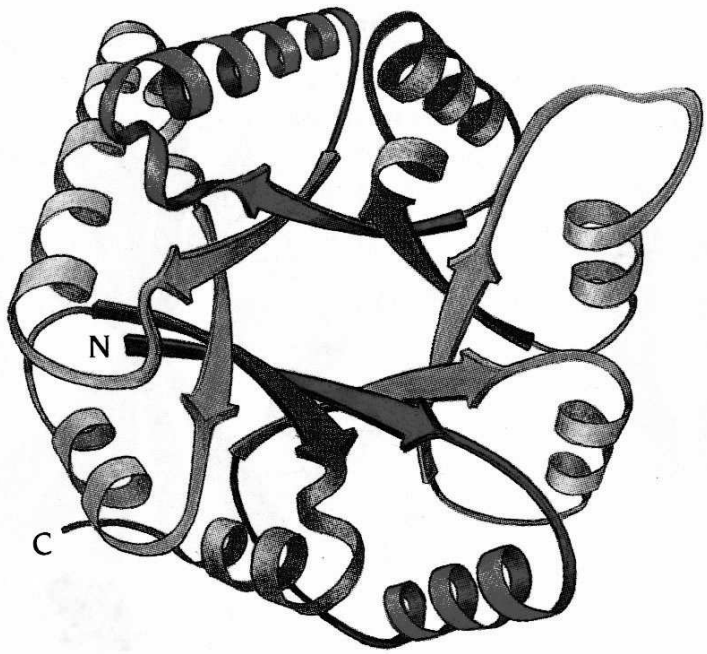

Figure 3.6: Tertiary structure and higher levels. A schematic representation of a three dimensional structure of an enzyme (Triphosphatisomerase), showing a symmetric composition of four domains with well defined tertiary structure.

3.2 Protein folding

During the synthesis of proteins on the ribosome the amino acids are attached into a long chain via the covalent peptide bond. The sequence of the amino acids in the protein chain is also referred to as the primary structure of the protein. The initially random conformation of the chain folds in most cases[1] spontaneously into the final well-ordered three dimensional structure. The physical forces driving this process are non-covalent in nature [23]. However, a coherent picture for protein folding is still missing and it represents a challenge for physicists.

Proteins are typically 50-500 monomers (amino acids) long. When submerged into a liquid system they can be viewed as classical string like objects undergoing thermal fluctuations. These fluctuations are not dominated only by nearest neighbor interactions along the chain, but are also influenced by

[1]There are examples where the cell machinery is required to assist a protein in its search for the *correct* conformation. Molecules assisting during folding are referred to as chaperones [30].

the interactions between distant monomers which can approach each other as the chain folds. The phenomenon is three dimensional in nature.

Why is protein folding considered a problem? It is possible to characterize the conformational space of a protein as consisting of discrete isomers. The interesting parameter is then the average number of accessible conformations per monomer unit. If we denote this number by γ then the total number $\mathfrak{A}$ of possible conformations which a protein can adopt can be estimated as:

$$\mathfrak{A} = \gamma^N \tag{3.1}$$

The exponential dependence of accessible conformational states on the number of monomers N poses a serious problem. If a protein were to perform an extensive search of the conformational space it would require much longer to reach the native state than the experimentally observable time scales of $1ms - 1s$. This problem was first explicitly formulated by Levinthal and is known as the *Levinthal paradox* [40, 41]. One common answer, which is popular with many biologists, states that the evolution has selected those proteins which fold fast enough. Instead of giving an answer, it simply postpones the original question to: "How did the evolution select those proteins?"

The basis for the current understanding of the protein folding from a physical perspective has been developed in polymer physics [52]. According to this picture there is a qualitative difference between the unfolded coil state and folded globule. Furthermore, the transition between the two states is viewed as a phase transition. This means, that there is a discontinuity in one of the thermodynamic variables as $N \to \infty$.

Briefly, it is essentially the chain connectivity which provides for long-range correlations in the coil state. This is also true for dilute and semi-dilute solutions of coils [52]. However, in the globule state there are attractions between monomers and/or external pressure which are strong enough to suppress these long-range correlations. Thus, the ***single-molecule*** globule is a thermodynamically stable uniform system whose interior resembles that of a concentrated polymer solution or a melt.

If a *single-molecule* is a thermodynamically stable system with a well defined structure, it opens the possibility to experimentally probe physical properties at the level of an individual molecule.

3.3 Protein-Protein interactions

Proteins in the cell interact specifically and form complexes. In general, these types of interactions are non-covalent in nature. There are several cases where the binding partners undergo major conformational change upon binding. For example, chaperones are molecules which assist in correcting the structure of misfolded proteins. Binding of the molecular chaperone to the target protein is accompanied by a conformational change in the target protein. Motor proteins also represent a typical class of molecules whose function is directly manifested by a conformational change. More precisely, the movement along the microtubule is directly associated with a conformational change. The order of magnitude of such steps is typically 8nm. The important point here is that the molecules interact along an interface. The biological function is thus also dependent on the detailed properties of the molecular surface.

3.4 Membrane fusion

As already mentioned in Chapter 3 membrane fusion plays a vital role for the proper functioning of the cell.

The membrane itself consists of lipids. A lipid molecule is composed of a hydrophilic head and a hydrophobic tail as shown in Figure 3.7. Molecules which unite hydrophobic and hydrophilic properties are called *amphipathic*. In aqueous environment lipids can spontaneously self assemble and form lipid bilayers.

Bilayers are most commonly formed by phospholipids, where a hydrophilic head group is linked to two hydrophobic carbon tails by a phosphate group. However, the amphipathic property can be found also in sterols and glycolipids, which can also form lipid bilayers.

From physical perspective, lipid bilayer can be thought of as two dimensional fluids. Their properties can be studied on two different classes of synthetic bilayers. First class are small closed spherical vesicles, called liposomes. They can be easily created *in vitro*. Second, it is possible to immobilize a thin lipid film on an appropriate surface. Thus, one can measure local viscous properties, which depend further on the structure of the membrane.

The degree of bilayer fluidity depends mainly on three factors as illustrated in Figure 3.8 (D):

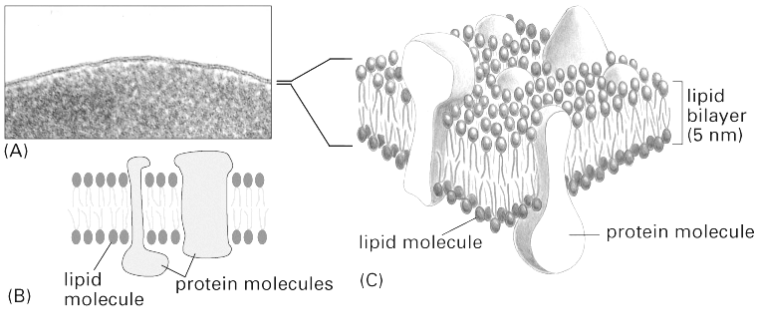

Figure 3.7: Structure of a membrane. (A) An electron micrograph of a plasma membrane seen in cross section. (B) A two dimensional schematic drawing of a membrane with proteins. (C) A three dimensional schematic drawing of a membrane with proteins.

(a) Lateral diffusion of phospholipids (flexion)
(b) Flip-Flop (occurs very rarely)
(c) Rotation of lipids

All the above mentioned factors depend further on structural composition of lipids. First, the length of a carbon tail varies typically between 14 and 24 carbon atoms. Shorter chains form less bonds within the bilayer than longer ones. Consequently, the bilayer is more fluid. Second, carbon atoms in the tail can be connected by single or by double covalent bonds (see Figure 3.8 (E)). If the atoms in the chain are connected with a double bond there appears a kink along the chain. Thus, there is less packing between opposite tails and the bilayer is again more fluid. In this case, the tails are *unsaturated* with respect to hydrogens. The opposite, that is the *saturated* case, appears when there are no double bonds along the carbon chain. The tail remains straight and there is more packing between opposite chains in the bilayer, resulting in decreased fluidity.

Although general properties of membranes can be understood from synthetic bilayers, biological membranes display a more complicated structure.

For example, the cell generates lipid asymmetry. The composition is different on the side facing the interior of a compartment than the one facing the exterior.

Furthermore, approximately 50% of the membrane mass is constituted by proteins. They carry out different specific tasks which can be classified

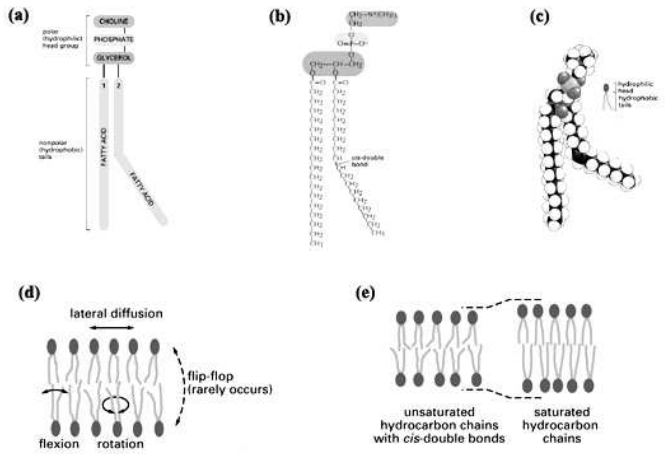

Figure 3.8: Mobility in lipid bilayers. Phospholipid molecules are most common constituents of membranes. They are represented in **(a)** schematically, **(b)** by a chemical formula, **(c)** as a space filling model. Fluidity of a lipid membrane depends on several factors. Three different possibilities for a movement of phospholipid molecules are shown in **(d)**, whereas the influence of *cis*-double bonds is illustrated in **(e)**.

into different categories such as: transporters, linkers, receptors, enzymes, etc.

Proteins are attached to the membrane in different ways. Most commonly they are extended across the membrane. Other membrane proteins are located entirely outside the layer and are attached to the membrane only by covalent bonds. Some proteins are located only on the one side of the membrane. They have been designed to specifically interact with proteins from other membranes. The SNARE complex belongs to this latter class.

Membrane proteins also display structure (see Figure 3.9). Typically, proteins cross the bilayer in form of an α-helix. Much less commonly to be found in membrane proteins are β-barrels. In contrast to cytosolic proteins, membrane proteins are much more difficult to crystalize: therefore the structure is known for relatively few.

3.5 Physics of bilayer fusion

Bilayer fusion is dominated by the hydrophobic effect, which guarantees that solvent-exposed non-polar surfaces are minimized during the process. The

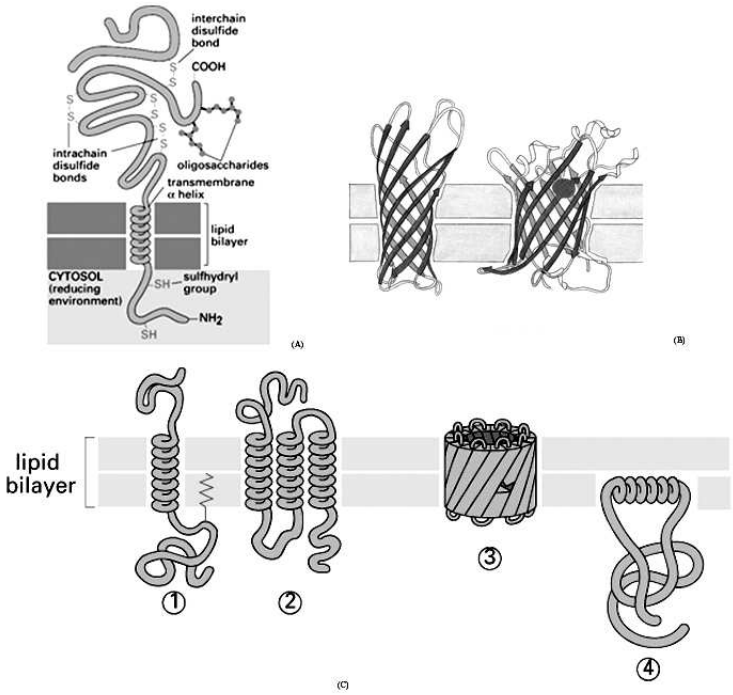

Figure 3.9: Membrane Proteins. There are several possible ways for a protein to associate with a membrane. The protein can cross the membrane in form of an α-helix (A) or as a β-sheet (B). Different combinations of the above are also possible as shown in (C). Some proteins are attached only on the one side of the membrane, they do not cross it.

energy barriers of membrane fusion have been estimated from recent experiments [35]. According to the Arrhenius law one can limit the upper barrier, including intermediates, to approximately 40kT.

Although several physical models have been proposed to explain the bilayer fusion [37, 36, 43, 35], only the **stalk** model is currently accepted to adequately describe the fusion process. Essentially, this model classifies the fusion process into several steps, as illustrated in Figure 3.10. First, the opposing bilayers, which are initially flat, are brought into close contact. When the bilayers are positioned close enough, an initial perturbation of the membranes occurs. This step is followed by the formation of the stalk. Fourth, the stalk has to expand. Finally, the pore is formed in the membrane.

There are several approaches towards a physical description of bilayer fu-

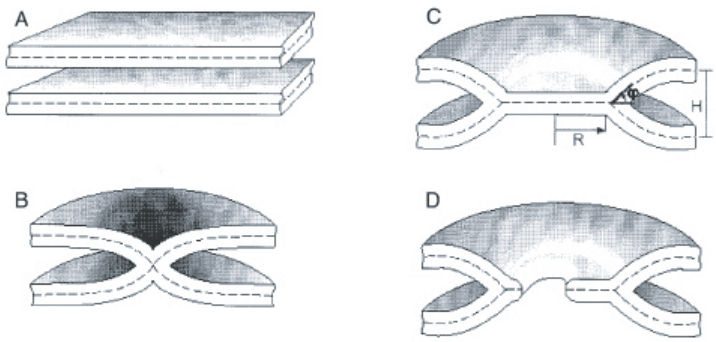

Figure 3.10: Stalk Model for bilayer fusion. Individual steps in the pathway of membrane fusion. **(a)** Initially flat membranes. **(b)** The formation of a fusion stalk. **(c)** The expansion of a fusion stalk. **(d)** Formation of a fusion pore.

sion, which are briefly discussed in the following subsection.

3.5.1 Continuum models

Continuum models treat the membrane as a homogenous elastic surface. The success of this approach consisted mainly in explaining the large variety of shapes that vesicles can adopt under different conditions. Furthermore, a successful phenomenological description of the cubic phase of the membrane indicated that the elastic theory might be adequate for the stalk model of membrane fusion as well [35]. However, energy barriers derived from the initial stalk models result in several 100kT for bilayer fusion. This number is essentially an order of magnitude too high and cannot properly explain the process.

It was not until recently [37], that a modified version of the stalk model has been proposed with the aim of resolving *the energy crisis*. The resulting energy barrier for bilayer fusion is approximately 50kT, as would be expected for membrane fusion *in vivo*. The proper correction of the original model is achieved by introducing bending and tilting of lipid molecules (see Figure 3.11).

Briefly, the elastic properties of a monolayer are determined by the hydrocarbon chains [31]. The major contributions to the elastic energy come

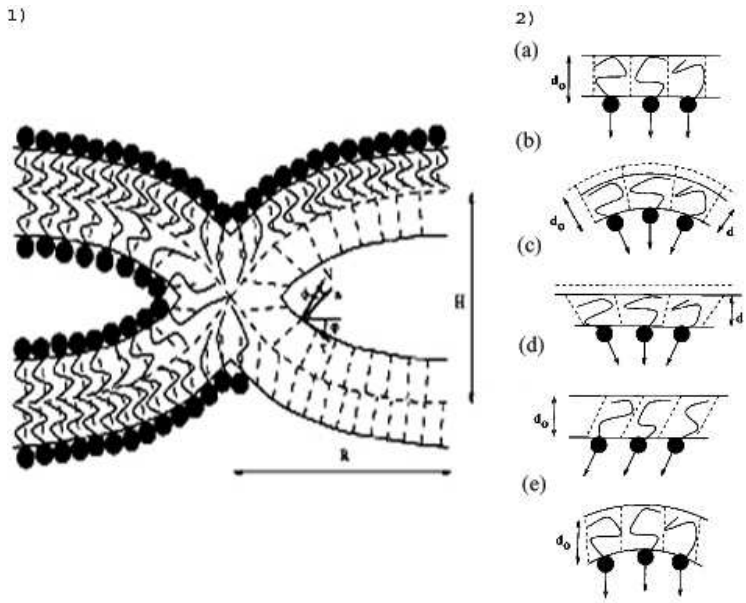

Figure 3.11: Tilting and bending of lipid molecules. 1) A representation of two dimensional cross section of stalk formation during membrane fusion. $\mathbf{N}$ is the unit vector of the normal to the bilayer surface, $\mathbf{n}$ is the vector along the hydrocarbon chain, τ is the tangential unit vector, φ is the tangential angle, ϕ is the tilt angle. 2) A schematic drawing of possible hydrocarbon chain orientations in the membrane. a) The initially undeformed state. b) Bending with vanishing tilt. c) Splay resulting from changing tilt in a flat monolayer. d) Homogeneous tilt of the chains. e) Mutual compensation of bending and tilt.

from the splay of the chains and from the tilt of the molecules with respect respect to the monolayer surface.

There are two geometric contributions to the energy of splay. First, the monolayer surface can bend and the hydrocarbon chains remain parallel to the surface normal, $\mathbf{n} = \mathbf{N}$ (Figure 3.11 b). Second, the vector $\mathbf{n}$, which is pointing in the direction of the hydrocarbon chain, can vary along a flat monolayer surface, $\mathbf{n} \neq \mathbf{N}$. Any further combination of these two deformations will also result in a splay.

Mathematically, the splay of hydrocarbon chains, denoted by J, is defined according to the equation 3.2:

$$J \equiv div\ \mathbf{n} \tag{3.2}$$

Here, $div\ \mathbf{n}$ is the divergence of the molecular director $\mathbf{n}$ along the mono-

layer surface. Hence, the energy per unit area stored in the dividing surface can be written according to [37]:

$$f_s = \frac{1}{2} \cdot \kappa \cdot (div\ \mathbf{n} - J_s) \tag{3.3}$$

where J_s is the spontaneous splay and κ is the splay modulus. The major assumption in this model is that the hydrophobic moiety is small compared to the monolayer thickness δ, $|div\ \mathbf{n}| \cdot \delta < 1$ [37].

The spontaneous splay modulus, J_s, has been experimentally estimated in the range from $-0.1\ nm^{-1}$ for slightly negative curvatures in common lipids such as DOPC, to $-0.35\ nm^{-1}$ for strongly negative curvatures as observed in DOPE. Lysolipids, especially lysophosphatidylcholine (LPC), have a spontaneous splay in the mid range of approximately $-0.26\ nm^{-1}$ [37]. Also, the splay modulus κ has been measured for monolayers. Typically, it has value of $\kappa = 10\ kT$.

The energy of the monolayer is not described fully by the splay but is affected also by the tilt of the hydrocarbon chains. The tilt can be characterized by a vector $\mathbf{t}$, defined as:

$$\mathbf{t} \equiv \frac{\mathbf{n}}{\mathbf{n} \cdot \mathbf{N}} - \mathbf{N} \tag{3.4}$$

which is always parallel to the dividing surface. The *tilt* energy can be then approximated as:

$$f_t = \frac{1}{2} \cdot \kappa_t \cdot \mathbf{t}^2 \tag{3.5}$$

where the quadratic approximation is valid for small $\mathbf{t}$, i.e. $|\mathbf{t}| < 1$. κ_t has been estimated from experiments on lipid phase transitions [37] with a value of $\kappa_t = 0.04\ N/m$.

The total energy per unit area of a monolayer, f_{tot}, consists of the energies of splay, Eq. 3.3, and uniform tilt, Eq. 3.5. It is defined with respect to the initial state having a vanishing splay, $J = 0$, and a vanishing tilt, $\mathbf{t} = 0$. We obtain:

$$f_{tot} = \frac{1}{2} \cdot \kappa \cdot (div\ \mathbf{n} - J_s) + \frac{1}{2} \cdot \kappa_t \cdot \mathbf{t}^2 - \frac{1}{2} \cdot \kappa \cdot J_s^2 \tag{3.6}$$

The total elastic energy of a monolayer, F_{mon}, can then be calculated from f_{tot} by integrating over the area A of the dividing surface:

$$F_{mon} = \int f_{tot}\, dA \tag{3.7}$$

In summary, the essential physical properties of lipid fusion process can be explained by the stalk hypothesis. The problems of unrealistically high energy barriers have recently been overcome by including tilting and bending of the hydrocarbon chains into the theory.

However, continuum models still have their own problems. Many models studied so far contain a presence of infinite curvatures along the reaction pathway. Such singularities have no physical meaning and should be avoided. The formation of a fusion pore occurs on a length scale of several nanometers and on a microsecond time scale. The matter is additionally complicated by the presence of several different energy barriers with their corresponding time scales. The molecular structure of the bilayer also implies that finite size effects and thermal fluctuations play an important role during the fusion process. It is here that continuum models run into difficulties.

High computer power has recently enabled more detailed simulations of the bilayer fusion reaction pathway. They can be classified into two different groups: *Coarse grained models* and *Atomistic models*.

3.5.2 Coarse grained models

These models include the finite size effects that arise from the molecular composition of a lipid membrane. Although interaction forces are parameterized from descriptions with full atomic detail, the model itself does not include every atomic detail in the simulation. This compensation increases the time scale of the simulation, albeit at the expense of details.

3.5.3 Atomistic models

Atomistic models are based on molecular dynamics simulations, where the interaction forces of all atoms are computed in detail. Hence, the simulations rest on fewer assumptions than continuum models and coarse grained models. Although these simulations have recently brought many advances [35], one can trace the physical system over relatively short time spans (approximately 10 - 20 ns). This time scale is believed to be the rate-limiting step for the formation of an intact lipid bilayer. However, primary steps during membrane

fusion occur on longer time scales. Therefore, major improvements in simulations are expected in the near future to come from larger computational power.

3.6 Protein-mediated membrane fusion

Biological membranes are more complex than pure lipid bilayers due to the presence of proteins. Similarly, the membrane fusion process does not involve only lipids, but it requires also specific proteins. As mentioned earlier in section 3.5, the energy barrier for membrane fusion is not very high. Therefore it may be surpassed by local fluctuations and perturbations. It is also not clear, whether there is a single pathway for membrane fusion as suggested by the stalk hypothesis or whether there is a greater diversity in pathways. Currently, there are several models which have been proposed and they differ in the nature of transition state, interaction of proteins with the membrane and significance of protein conformational changes for membrane fusion (see Figure 3.12).

3.6.1 Proteinaceous fusion

Proteinaceous fusion pores are thought to consist of oligomeric transmembrane proteins with a hydrophilic channel in the middle. According to this model, formation of a fusion pore takes place at the onset of membrane fusion. In many experiments it has been observed that an aqueous connection forms before lipids can diffuse from one membrane to the other [35]. The proteinaceous model can explain this observation, because the formation of a fusion pore precedes membrane fusion.

The important steps in the pathway as proposed by this model are illustrated in Figure 3.12a. Initially, subunits have to assemble into a ring like oligomer. Upon a membrane contact, *trans*-complexes of oligomers can form and the central aqueous pore can open. Subsequently the pore is enlarged by a radial spread of subunits constituting the complex and lipid molecules can start to diffuse into the pore. Finally, the *trans*-connections among the subunits break up and the fusion process is completed.

The major problem of this model consists in the last step. It is difficult to imagine how the breaking up of the pore can happen. Also, a consistent

biophysical description for this model is not yet available.

3.6.2 Fence models

The similarity between the fence model and proteinaceous model consists in the fact, that both require a formation of oligomeric rings (see Figure 3.12b). However, there are also important differences between the two models. In the fence model, there is a patch of lipids present in the middle of the ring from the onset of the fusion process. The role of proteins is then to control the flow of lipid molecules during the process. Fusion is essentially lipid based and there is no *a priori* need for ring like oligomers in order for fusion to take place. Fence models have been discussed for several viral proteins [35].

3.6.3 Scaffold models

The basic idea for the scaffold model arose from the observation that flickering of fusion pores occurs not only during protein-mediated membrane fusion but also during the fusion of protein free bilayers. Hence, the role of the proteins has been proposed to bring the opposing bilayers into close contact (see Figure 3.12c). This may occur with the proteins exerting mechanical force in order to overcome the energy barrier. It should be noted that this idea is very similar in nature to the one proposed for the SNARE model (see 3.6.5 below).

Interestingly, the model does not require that scaffold proteins participate in the transition states. They are considered to be purely lipidic in nature. Furthermore, the model does not relate the spanning of the membrane to the scaffold proteins.

3.6.4 Local perturbation models

An interesting phenomenon occurs when amphiphilic peptides are added in μM concentrations to liposomes in aqueous solution. They cause spontaneous fusion of liposomes at room temperature. The kinetics of the reaction is orders of magnitude faster than in liposomes which were reconstituted with SNARE proteins (see below 3.6.5).

The proposed mechanism for such *peptide-induced* local perturbation of the membrane assumes that the peptide undergoes a conformational change

after membrane insertion (see Figure 3.12). It should be noted that the membrane fusion is equally efficient if the peptides are present only on one of membrane surfaces. This reaction suggests that the energy landscape of membrane fusion is rather flat. In this case, the fusion process does not appear to be very specific as long as the membranes are in close proximity. Amphiphilic peptides have been found in many viral proteins.

3.6.5 Membrane fusion mediated by Proteins: the SNARE complex

Eukaryotic cells possess many different classes of proteins which are active in processes involving membrane fusion. This is valid in both cases; extracellular and intracellular. An example for extracellular membrane fusion is unification of a sperm with an egg. Inside the cell, there are mitochondria and peroxisomes which are equipped with their own set of proteins which carry out membrane fusion.

The secretory pathway in the cell has been rigorously studied. There are several dozens of proteins that have been identified to be essential for docking and fusion. Partial reactions have been well studied [35]. The **SNAREs** are at present the best universal candidate to explain membrane fusion in the secretory pathway. However, it is still controversial whether they catalyse the reaction or whether the membrane merger is dominated by other factors.

How does membrane fusion according to the *SNARE-hypotheses* then proceed? First, complementary sets of SNARE proteins have to be present in both membranes. The proteins in opposing membrane than interact with each other. Consequently, a trans-complex forms. This simply ties the membranes together and it can also cause fusion. The remaining steps are very similar to the scaffold model (see Figure 3.12c).

There is extensive experimental evidence which shows that SNAREs are essential for membrane fusion [35]. When proteoliposomes are reconstituted with SNAREs *in vitro*, they start to fuse. The kinetics of the reaction is very slow. Furthermore, it has been observed *in vivo* and *in vitro* [35], that fusion is inhibited or reduced after replacing the trans-membrane domains with lipid anchors. The same occurs also upon the introduction of flexible linkers.

In summary, SNAREs are essential for membrane fusion in eukaryotic cells. The open question is about their specific task during the process. Are they required for the catalysis of membrane fusion or are they involved in setting up the fusion site? A close look at the structure of the complex, see section 7.14 for details, shows that the size of the SNARE complex could vary between several nanometers when folded and around 10nm when unfolded. If the function of the SNARE complex is not exclusively related to the setting up of the fusion site, it would be expected that a conformational change during the complex formation could exert some mechanical force to overcome the energetic barrier. The conformational change is expected to be on the order of several nanometers or more.

Thus, the complex is definitely worthy of a detailed analysis at the level of individual molecules. By analyzing an individual complex in isolation, one could directly determine the reaction time scale for complex formation as well as its mechanical properties. In this manner one can contribute in elucidating the complex process of membrane fusion.

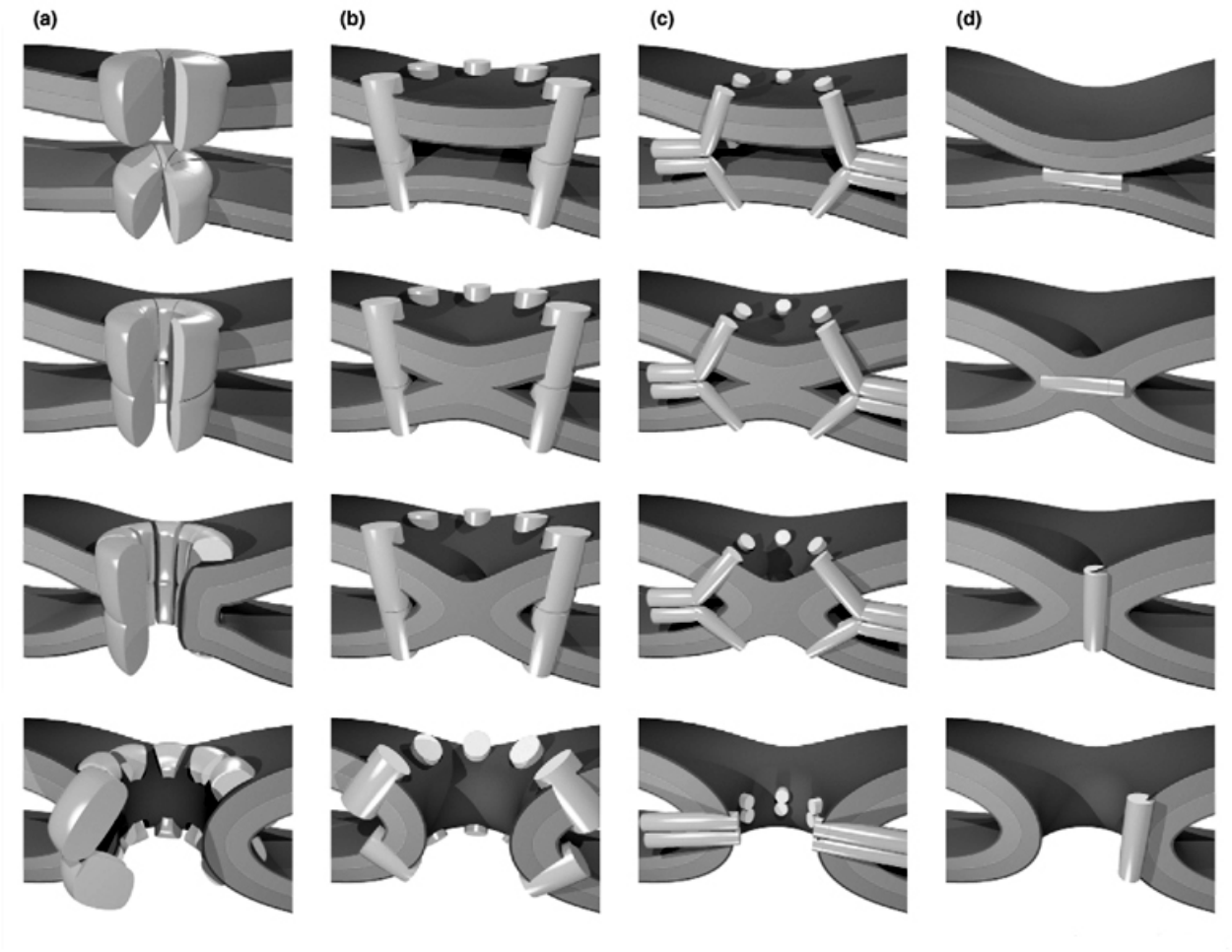

Figure 3.12: Proposed models for protein-mediated membrane fusion. (a) The proteinaceous model assumes that an oligomeric transmembrane complex with a hydrophilic channel in the middle opens at the beginning of the fusion. During the process the subunits dissociate radially, with lipids filling up the void. (b) The fence model is essentially lipid based. The role of proteins is to form a ring which controls the flow of lipids. (c) The scaffold model is also lipid based. Unlike in the fence model, proteins play an essential role in bringing the membranes into close contact, possibly by exerting mechanical force. (d) Amphiphilic peptides can induce membrane fusion, but the mechanism is not yet clear. Most likely, they lower the activation energy barrier for the bilayer fusion by causing a local perturbation. Since this process is more leaky, it is unlikely that in this case the fusion process follows a well structured path.

Part II

Theoretical Concepts

Chapter 4

Thermally activated phenomena

4.1 The Langevin equation

In my experiments the movement of a microsphere, which is suspended in aqueous solution, is constrained in an optical trap as explained in chapter 6. There forces which act on the trapped microsphere can be classified into two groups: optical and thermal. This section is mainly concerned with the mathematical description of the contributions from the thermal fluctuations of water molecules which generate the random force on a trapped microsphere. A mathematical form which captures the essentials of this phenomenon can be expressed through the Langevin equation. Below I give the definitions and results to selected problems.

The equation of motion of a particle can be written in general:

$$m\,\frac{d\mathbf{u}}{dt} \;=\; \mathbf{F}, \tag{4.1}$$

where m is the particle mass, $\mathbf{u}$ is particle velocity and $\mathbf{F}$ is an instantaneous force acting on the particle. If there is no source of noise in the system then the equation 4.1 is identical to the Newton's equation of motion. However, in our system some noise is present because the thermal position fluctuations of the trapped bead are caused by the constant bombardment from surrounding water molecules. Therefore, one should write for the force in equation 4.1:

$$\mathbf{F} \;=\; \mathbf{F}_{det} + \mathbf{R}(\mathbf{t}), \tag{4.2}$$

where $\mathbf{F}_{det}$ is deterministic part of the force and $\mathbf{R}(\mathbf{t})$ represents some random

force. An example for the deterministic part of *the force* is frictional force $\mathbf{F}_u = -\gamma\mathbf{u}$, where γ denotes the frictional coefficient. In aqueous solutions γ stands for Stokes drag. By using the Stokes law this can be further modified $\gamma = 6\pi a\eta$; where a is the radius of the microsphere and η is the viscosity. If the particle is additionally trapped in the potential V then a general Langevin equation can be written:

$$m\,\frac{d\mathbf{u}}{dt} \;=\; -\nabla V - \gamma\mathbf{u} + \mathbf{R}(\mathbf{t}). \tag{4.3}$$

By using the following definition:

$$\frac{d\mathbf{x}}{dt} \;=\; \frac{\mathbf{p}}{m} \;\equiv\; \mathbf{u}(t), \tag{4.4}$$

the equation 4.3 can be rewritten:

$$\frac{d\mathbf{p}}{dt} \;=\; -\nabla V - \gamma\frac{\mathbf{p}}{m} + \mathbf{R}(\mathbf{t}). \tag{4.5}$$

In the following I will describe a general solution to the problem which can be described in terms of equations 4.4 and 4.5. I will restrict myself to one dimension — the three dimensional case is treated in an analogous manner [38]. First, I consider the case with no external potential. This is followed by the solution of the equation where an external potential is present. In subsection 4.1.1 I also analyze the situation where the friction of a microsphere is relatively large so that the inertial term can be neglected.

In the first case, where no external potential is present, the Langevin equation can be written:

$$m\frac{du}{dt} \;=\; -\gamma u + R(t). \tag{4.6}$$

First, we make a Fourier expansion for:

$$\begin{aligned} R(t) \;&=\; \sum_{n=-\infty}^{n=\infty} R_n\, e^{i\omega_n t} \\ u(t) \;&=\; \sum_{n=-\infty}^{n=\infty} u_n\, e^{i\omega_n t}, \end{aligned} \tag{4.7}$$

where R_n and u_n are coefficients in the Fourier expansion of random processes, R(t) and u(t), respectively. In general, one can expand a stationary random process $\mathbf{z}(t)$ into a Fourier series with coefficients a_n, such that [38]:

$$\mathbf{a_n} \;=\; \frac{1}{T}\int_0^T \mathbf{z}(t)\,\exp^{-i\omega_n t}\,dt. \tag{4.8}$$

The power spectrum of a process is defined as:

$$I(\omega) \;=\; \lim_{T\to\infty}\frac{T}{2\,\pi}\,\langle|a_n|^2\rangle, \tag{4.9}$$

where an expression for $\langle|a_n|^2\rangle$ follows directly from equation 4.8:

$$\langle\,|a_n|^2\,\rangle \;=\; \frac{1}{T^2}\int_0^T\int_0^T dt_1\,dt_2\langle z(t_1)\,z^*(t_2)\rangle\,\exp^{-i\,\omega_n\,(t_1-t_2)}\,. \tag{4.10}$$

By substituting 4.7 into 4.6 we obtain the following relations for the n-th component in the expansion series:

$$u_n\,(i\omega_n+\frac{\gamma}{m}) \;=\; \frac{R_n}{m} \tag{4.11}$$

The equation 4.9 gives the following relation:

$$I_u(w) \;=\; \frac{1}{\omega^2+(\frac{\gamma}{m})^2}\cdot\frac{I_R(\omega)}{m^2}, \tag{4.12}$$

where we obtained a relation between power spectra of velocity and noise.

The presence of an external potential does not alter the situation significantly. If the potential in equation 4.5 can be approximated by a harmonic potential, $V=\kappa x$, the Langevin equation can be written:

$$\frac{d^2x}{dt^2}+\frac{\gamma}{m}\frac{dx}{dt}+\omega_0^2\,x \;=\; \frac{1}{m}\,I_R(t), \tag{4.13}$$

where $\omega_0^2=\gamma/\kappa$. An analogous harmonic derivation can be applied to obtain a relation between the power spectra of position and noise [38]:

$$I_x(\omega) \;=\; \frac{1}{(\omega_0^2-\omega^2)^2+(\frac{\gamma}{m})^2\,\omega^2}\cdot\frac{I_R(\omega)}{m^2}. \tag{4.14}$$

In the next section 4.1.1 I focus on the form of the Langevin equation which approximates the circumstances in my experiments very well.

4.1.1 The Langevin equation in the limit of low Reynolds numbers

Thermal fluctuations of microspheres were confined in an optical trap in my experiments. A hydrodynamical characterization of these microspheres shows that they have low Reynolds numbers. Therefore the inertial term in the Langevin equation 4.3 can be neglected and we have to solve the following equation:

$$-\kappa x - \gamma \frac{dx}{dt} + R(t) \;=\; 0. \tag{4.15}$$

Let X_n and R_n be the coefficients in the Fourier expansion of $x(t)$ and $R(t)$, respectively. By substituting the expansions of $x(t)$ and $R(t)$ in the equation 4.15 we obtain a relation for the Fourier coefficients X_n and R_n:

$$X_n \;=\; \frac{1}{\kappa + i\omega_n\gamma}\, R_n, \tag{4.16}$$

which leads immediately to an expression for the power spectra:

$$I_x(\omega) \;=\; \frac{1}{\kappa^2 + \omega^2\gamma^2}\, I_R(w). \tag{4.17}$$

It is common to write the equation 4.17 in the following form:

$$I_x(\omega) \;=\; \frac{1}{\omega_C^2 + \omega^2} \cdot \frac{I_R(w)}{\gamma^2}, \tag{4.18}$$

where $w_C = k/\gamma$ stands for the Corner frequency. Because the experimental observable is the frequency f and not ω one often encounters the above equation in the form:

$$I_x(f) \;=\; \frac{1}{4\,\pi^2\,(f_C^2 + f^2)} \cdot \frac{I_R(f)}{\gamma^2}. \tag{4.19}$$

In the presence of white noise we can write: $I_R(f) = I_R = const$. The coefficient I_R can be obtained in this case from the fluctuation dissipation theorem: $I_R = 4\gamma k_B T$ [27]. Therefore the power spectral density takes the form:

$$I_x(f) \;=\; \frac{k_B T}{\gamma\,\pi^2\,(f_C^2 + f^2)}. \tag{4.20}$$

It is interesting to note that the above expression shows to different regimes. For $f << f_C$ the power spectrum $I_x(f)$ is basically a constant: $I_x(0) \approx 4\gamma k_B T/\kappa^2$. This part reflects the confinement of the microsphere in the optical trap. In the case $f >> f_C$ the power spectral density falls off as $1/f^2$,

which is typical for free diffusion. In conclusion, on short time scales the microsphere behaves as a free diffusing particle and on long time scales the microsphere feels the influence of the laser trap.

4.2 The effect of geometry on reactions governed by diffusion

In this section I consider the effects of local geometry on the average passage time needed for the specific molecular reaction to occur. The emphasis is given to the situations that are similar to the circumstances in my experiments. We chose a model with two major contributions to the average passage time of the specific binding reaction (see section 7.1.4): **(a)** the specific molecular surface coverage and **(b)** the dimension of the diffusion space with the boundary conditions. Below, I give a brief description of the experiment which is followed by the model for the average passage time. By measuring the average passage time for the reaction to occur and by knowing the surface density of avidin molecules one can estimate the size of *a reactive molecular binding site* on the glass surface and compare them with the calculated estimates (see section 7.1.4).

The molecular reaction occurred between avidin and biotin — a receptor protein and a ligand molecule, respectively. Avidin molecules were covalently immobilized on the surface of a polystyrene microsphere. Biotin molecules were covalently attached to BSA[1] molecules and subsequently immobilized on the glass surface by adsorption (see section 7.1). There were on average 8 biotin molecules per individual BSA molecule. The microsphere was trapped in the optical trap. Since the sphere experiences thermal position fluctuations it behaves as a Brownian particle. Therefore one can characterize the movement of the microsphere by a diffusion constant. Because avidin molecules are covalently attached to the surface of the microsphere, they diffuse with the same diffusion constant as the microsphere. The surface density of biotin binding sites has been estimated in section 7.1. There is 1 binding site per circle of area with a radius of 1nm — a very dense packing of avidin molecules on the surface of the microsphere. The surface density of avidin molecules is kept constant during the experiment, while the surface density of biotin molecules is varied.

[1]BSA — Bovine Serum Albumin

The average time τ for a molecule to reach its destination from the diffusion space can be expressed as:

$$\tau^{(n)} = \frac{r^2}{D^{(n)}} \cdot \mathrm{f}^{(n)}(r/q). \tag{4.21}$$

Here, n is the dimensionality of the diffusion space, r is the size of the diffusion space and q is the size of the small destination area (see figure 4.1). A further assumption is that the problem contains some spherical or cylindrical symmetry [1, 28], which is a suitable approximation to the situation defined by our experiments (see chapter 6). Also, for simplicity, I will define:

$$\xi \equiv q/r. \tag{4.22}$$

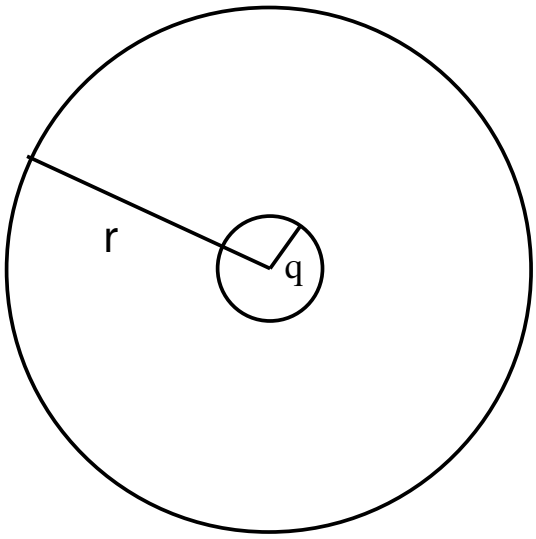

Figure 4.1: Molecularly specific binding of a microsphere to the surface considered as a diffusion governed reaction. The larger circle with radius r represents the size of the diffusion space and the smaller circle with radius q the size of the molecular target. The molecule can diffuse in the space between the two circles until it binds to the target at the outer boundary of the smaller circle. The picture is not drawn up to scale. In a realistic case $r >> q$ with a ratio of $\xi \equiv q/r \approx 0.1$.

Equation 4.21 consists conceptually of two terms. The first term, $r^2/D^{(n)}$, can be thought of as a distance factor. Apart from the diffusion constant $D^{(n)}$, it does not depend on the dimensionality of the diffusion space. It represents the time needed for a molecule to travel the distance r. The second term is a kind of correction factor which depends strongly on the dimensionality and the geometry of the problem.

The problem we are going to consider can be formulated in the following way. A molecule is located at a certain point A within the diffusion space and has to reach the target B. In the following, the dimension of the target B will be much smaller than the dimension of the diffusion space.

The time dependent diffusion equation takes the general form:

$$\sum_{i=1}^{n} \frac{\partial^2 c}{\partial x_i^2} = \frac{1}{D^{(n)}} \frac{\partial c}{\partial t}. \tag{4.23}$$

At time $t = 0$, let there be a concentration c_0. In the course of time the molecules are going to diffuse to the target and bind. The concentration of molecules $c(x_i, t)$ will thus decrease with time. The number of remaining molecules $P(t)$ can be obtained by integrating over the whole volume with the exclusion of the volume encircled by q at any given time:

$$P(t) = \int_V c \, dV. \tag{4.24}$$

Now, we can define the average time needed by a molecule to bind to the target. If $P(0)$ is the number of molecules at $t = 0$, we can write:

$$\tau = \int_0^\infty \frac{d}{dt} \left(1 - \frac{P(t)}{P(0)}\right) t \, dt. \tag{4.25}$$

In order to solve the time dependent diffusion equation we have to introduce boundary conditions. There are two types of boundary conditions which give rise to a unique and stable solution of the time dependent diffusion equation: Dirichlet and Neumann boundary conditions on open surface. Dirichlet boundary conditions specify the value of a function at the boundary, whereas Neumann boundary conditions specify the value of normal derivative at the surface. Translated to our problem, the boundary conditions will take the following form:

$$c = 0 \qquad \text{on the outer boundary of the target,} \tag{4.26}$$

and

$$\frac{\partial c}{\partial r} = 0 \qquad \text{on the boundary of the diffusion space.} \tag{4.27}$$

The imposition of the first boundary condition 4.26 is intuitive: when the molecules bind to the surface they disappear from the solution. The second boundary condition, 4.27, has essentially been invoked to prevent the

molecules from escaping to infinity.

The general solution of the diffusion equation satisfying these boundary conditions can thus be written [1]:

$$P(t) \;=\; P(0)\sum_k B_k \exp(-\frac{t}{\tau_k}). \tag{4.28}$$

From the definition of τ in 4.25 one can write further:

$$\tau = \sum_k B_k\, \tau_k. \tag{4.29}$$

The result 4.29 tells us that the average binding time consists of a series of exponential terms. In the further discussion we neglect all but the highest term in the series of τ_k, because this subpopulation represents the large majority of the molecules in the case where the target is very small compared to the size of the diffusion space.

The results for the diffusion in a two dimensional ring are obtained subject to the above boundary conditions. Let q be the radius of the target and r the radius of the diffusion space:

$$\tau^{(2)} \;=\; \frac{r^2}{D^{(2)} y_1^2} \tag{4.30}$$

The parameter y_1^2 has been numerically calculated in reference [1] with an accuracy of better than 7% with respect to the exact solution for $\xi \leq 0.1$.

Next, we consider the special case of three dimensional diffusion in a spherical shell. Again the radius of the smaller sphere is q and that of the larger one r. With the same initial conditions as for the two dimensional ring one obtains the solution for P(t) [1]:

$$P(t) \;=\; P(0)\sum_{k=1}^{\infty} B_k^{(3)}\, \exp\left(-\frac{D_1^{(3)}}{r^2}\, x_n^2 t\right) \tag{4.31}$$

By following a similar procedure as in the case of the two dimensional ring we obtain an expression for $\tau^{(3)}$:

$$\tau^{(3)} \;=\; \frac{(1-r/q)^2}{3qD^{(3)}}\, r^3 \tag{4.32}$$

In summary, by considering the time dependent diffusion equation, an approximate solution for the average time it takes for a molecule to bind

to the target was obtained. The geometry of the diffusion space and of the target were considered to be spherical (3D) or circular (2D). The essential step in the above given approximations is the small value of the ratio ξ; $\xi = q/r$. This approximation is similar to the experimental conditions when considering the size of the diffusion space and that of the molecular target immobilized at the surface.

Chapter 5

Basics of optical tweezers

5.1 Optical forces in a single beam gradient laser trap

A highly focused laser beam can generate forces on dielectric particles. To achieve a stable laser trap the exerted forces have to point towards an equilibrium position. When a dielectric particle is illuminated by a highly focused laser beam the force can be understood in terms of gradient and scattering forces. In addition to optical forces there are also thermal excitations which cause local position fluctuations for a trapped particle. A proper balance of the terms has to be achieved in order to obtain a stable laser trap.

Optical forces depend on the following parameters: diameter of the particle and its refractive index. Furthermore, light scattering depends on the ratio of r/λ, where r is the radius of the particle and λ is the wavelength of the laser light. If $r << \lambda$, the trapped particle behaves as a Rayleigh scatterer. A theoretical description in this regime uses the electromagnetic wave description for the laser light [53]. In the case when $r >> \lambda$ the trapped particle behaves as a Mie scatterer. One can apply geometrical optics to describe the forces acting on the bead [7]. The highest forces have been measured in the regime where $r \approx \lambda$ [57]. In my experiments I used particles with $r < \lambda$.

The physical origin of optical forces can be found in the electromagnetic description. A highly focused laser beam with large numerical aperture creates a diffraction limited focus spot whose diameter is $\approx \frac{\lambda}{n_m}$. Here, n_m is the refractive index of the surrounding medium. In our case it was an aqueous solution with $n_m = 1.33$. Because the beam is tightly focused there is a strong intensity gradient in the proximity of the focus. If a dielectric particle

passes through the focus it will experience an attractive gradient force and a repulsive scattering force.

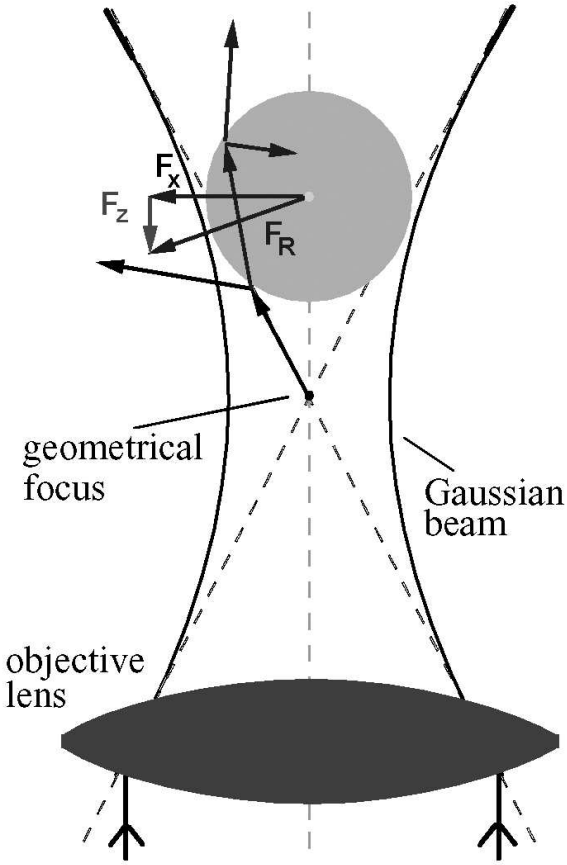

Figure 5.1: Optical forces in a single gradient laser trap. A dielectric sphere is trapped in an equilibrium position slightly behind the geometrical focus of the laser trap. The laser beam has a gaussian profile. The force acting on the microsphere is generated by the transfer of momentum of the refracted laser light to the microsphere.[1]

A dipole moment is induced in a dielectric particle because of its susceptibility when it passes through an electromagnetic field. Let n_p be the refractive index of the particle. In my experiments I used polysterene (Latex) particles whose refractive index is $n_p = 1.57$. The particle susceptibility can be written in the Born approximation by using CGS units:

[1]Figure 5.1 illustrates the geometrical interpretation of optical trapping. The interpretation is valid in *Mie* regime: i.e. $\lambda << r$.

$$\mathbf{p}_p = \frac{\epsilon_p - 1}{\epsilon_p + 2} r^3 \epsilon_m \mathbf{E}_m \tag{5.1}$$

Here $\epsilon_p = n_p^2$, $\epsilon_m = n_m^2$ and r is the particle radius. Furthermore, $\mathbf{p}_p$ is the dipole moment and $\mathbf{E}_m$ is the external electric field. If we introduce a polarizabilty of the particle [34]:

$$\alpha_p = \frac{\epsilon_p - 1}{\epsilon_m + 2} r^3 \tag{5.2}$$

then the equation 5.1 can be simplified to:

$$\mathbf{p}_p = \alpha_p \, \epsilon_m \, \mathbf{E}_m \tag{5.3}$$

The total Lorenz force acting on the particle can then be written [34]:

$$\mathbf{F} = (\mathbf{p}_p \cdot \nabla)\mathbf{E}_m + \frac{1}{c} \partial_t \, \mathbf{p}_p \times \mathbf{B}_m \tag{5.4}$$

By using the Maxwell equation:

$$\nabla \times \mathbf{E} + \partial_t \, \mathbf{B} = 0 \tag{5.5}$$

and the identity:

$$(\mathbf{E} \cdot \nabla) = \frac{1}{2} \nabla \, \mathbf{E}^2 - \mathbf{E} \times (\nabla \times \mathbf{E}) \tag{5.6}$$

the equation 5.4 can be further simplified to:

$$\mathbf{F} = \alpha_p \, \epsilon_m \, \nabla |\mathbf{E}_m|^2 + \alpha_p \, \epsilon_m \, \partial_t \, (\mathbf{E}_m \times \mathbf{B}_m) \tag{5.7}$$

It should be noted that the right term in the above equation is proportional to the time derivative of the *Poynting* vector $\mathbf{S}$. The Poynting vector is proportional to $\mathbf{S} \sim (\mathbf{E} \times \mathbf{B})$ and it has a dimension of $[Energy/(Area \cdot Time)]$. It represents the total momentum carried by an electromagnetic wave. The time average of this term in the equation 5.7, $\partial_t \, (\mathbf{E}_m \times \mathbf{B}_m)$, will vanish for a stationary wave [17]. There would be a contribution only if one uses a pulsed laser and not a continuous one. So, we are left with only a gradient term and the question arises: "Where has the scattering term of the force disappeared?"

In order to obtain the correct force, one has to rewrite the expression for the total force exerted on a microsphere in terms of *force densities per volume.* After a rather lengthy calculation one arrives at the following expression [56]:

$$\mathbf{F} \;=\; \int \frac{\alpha\, n_m}{2cV}\, \nabla\, I_0(\mathbf{r}')dV' \;+\; \frac{n_m}{c}\, I_0\, \left[C_{ext}\, \langle \cos\theta_i \rangle - C_{sca}\, \langle \cos\theta_s \rangle\right] \frac{\mathbf{k}}{|\mathbf{k}|} \tag{5.8}$$

where I_0 is the incident intensity at the location of the scatterer:

$$I_0 \;=\; \frac{c\,\epsilon}{2\, n_m}\, |\mathbf{E_i}|^2 \tag{5.9}$$

C_{ext} and C_{sca} represent the extinction and the scattering cross-section, respectively. The terms $\langle \cos\theta_{i,\,s} \rangle$ represent asymmetry factors [56]. The equation for the total force exerted on a trapped microsphere can finally be written as a sum of a *gradient* and a *scattering* term:

$$\mathbf{F} \;=\; \int_V (\mathbf{f}_{grad} + \mathbf{f}_{scatter})dV \tag{5.10}$$

In summary, an equilibrium of the optical forces is achieved by the balance between the attractive gradient part and the repulsive scattering part. This balance of force is superposed by thermal fluctuation forces which are responsible for the finite dimension of the localization volume, i.e. a trapped particle is not completely confined. It exhibits small thermal position fluctuations in a finite three dimensional space around the center of optical trap.

Part III

Experimental Procedures and Results

Chapter 6

Experimental Setup: Photonic Force Microscope

Scanning force microscopy (SFM) has been introduced in 1986 with the advent of atomic force microscopy (AFM) by Binning *et al.* [11]. They used a very sharp tip of the atomic force microscope to measure the interaction forces between the tip and the surface. This method enabled mapping of the topography of the surface with atomic resolution.

Biological organelles would not exist without boundaries. They are enclosed by membranes which consist of lipids and proteins. This is a natural example where surfaces play a vital role. Cell membranes are filled with proteins which carry out specific functions: cell signalling, receptors, membrane fusion, etc. There is abundant evidence that the cell membrane contains functional clusters of proteins. A special class of protein clusters in the membrane are referred to as *rafts*. They have recently been investigated by the SFM [53].

A different field of applications for SFM is the study of mechanical properties of individual molecules. First measurements of intermolecular forces between a ligand and a receptor have been done with an AFM [24, 47]. These early attempts were soon followed by measurements of intramolecular forces which were interpreted in terms of protein unfolding [54, 55].

AFM was not to remain the only SFM technique used in biophysical applications. Alternative experimental approaches include optical tweezers and bio-force-probe (BFP). The first direct measurement of energy landscapes between individual ligand-receptor pairs was performed on this apparatus [21, 44].

In my thesis, I used an optical experimental technique: optical tweezers with three-dimensional position detection. Such an experimental setup was introduced in 1997 by Florin et al. as Photonic Force Microscope (PFM) [25] as a tool to image biological material and to characterize its mechanical properties. The basis for this very promising field was created in 1970 when Ashkin successfully demonstrated that particles can be accelerated and trapped by radiation pressure [5]. Sixteen years later he showed that a three-dimensional trapping of a particle is possible with a single beam [6, 7]. Here, a single beam gradient laser trap is used to manipulate small dielectric particles with diameters ranging from $10nm$ to $10\mu m$. Since the invention of the optical tweezers there have been many applications to biological problems. Examples include trapping of viruses and bacteria [6], induced cell fusion [60], studies of chromosome movement [10].

A trapped microsphere is thermally activated by the aqueous environment. Consequently, it experiences thermal fluctuations having an energy on the order of $k_B T$. Thermal energy of $k_B T$ at room temperature is equivalent to the work performed by a constant force of $\approx 4pN$ applied over a distance of $1nm$. It has been demonstrated that forces which are exerted on a trapped microsphere can be detected and applied by optical tweezers in the range of several piconewtons. [13, 14, 25, 62, 63].

Thermally activated conformational fluctuations of individual biomolecules are expected to occur on the nanometer length scale and thereby exert forces on the order of piconewton. The experimental setup has to be sufficiently stable in order to detect and measure such small fluctuations.

The are two aims of the following sections of this chapter. The first aim is to give a description of the experimental setup. Section 6.1 introduces the design of this setup and section 6.2 the position detection system. The second aim consists of an introduction of quantitative methods for the calibration of position measurements and a discussion of its range of applicability. This is done in sections 6.3 and 6.4, respectively.

6.1 Experimental design of PFM

Optical tweezers use a strongly focused laser beam to generate force in order to trap a dielectric particle in three dimensions. The laser beam has two important functions: **(i)** for position detection and **(ii)** as a force transducer.

This method differs significantly from other SFM techniques in the way the force is transduced on the probe. It does not require a direct mechanical support because the laser light is used to generate necessary force.

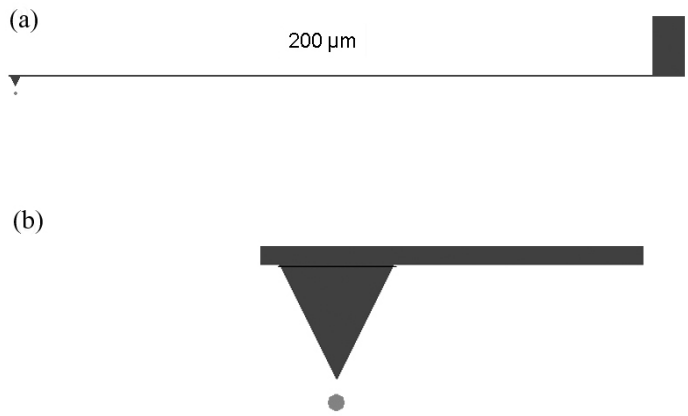

Figure 6.1: Comparison of scanning probes. Atomic Force Microscope uses a cantilever arm to apply and measure force, whereas PFM utilizes optical forces which are exerted on a trapped dielectric microsphere. (a) An AFM cantilever and a bead are drawn to scale. The cantilever arm of an AFM is typically 200 μm long, which surpasses the dimension of a microsphere (bead) used in PFM by two orders of magnitude. (b) The tip of an AFM is amplified and shown in comparison with a typical microsphere. The main difference between the two consists in the geometry of the contact surfaces. The AFM tip is sharper at the end but bulkier in size. The bead is smaller in the overall size and more flat at the surface of contact.

There are several important aspects which make this method unique. First, it is possible to apply and detect very small forces in the piconewton range and below. Second, submicrometer beads can be used to probe biological material. On the one hand, this offers a radically different local experimental geometry as compared to an AFM (see Figure 6.1). On the other hand, the thermal fluctuations of an optically trapped microsphere can be used to image soft environments such as the interior of a cell or a polymer network [64]. An AFM uses a very long lever arm, $\approx 200\mu m$ long. There is a scanning tip attached at the end of the arm. The dimensions of such a device surpass the dimensions of an individual microsphere significantly (see figure 6.1a). The latter is used as a force transducer in the optical tweezers. A magnification showing only a typical microsphere in comparison to the tip of an AFM is shown in figure 6.1b.

PFM offers another important advantage, it allows imaging and manip-

ulation in transparent biological materials. Because there are no mechanical constraints one can access the inside of a cell without causing any severe damage to the tissue or to any other vitally important part of the cell [53].

The design of the experimental setup is illustrated in Figure 6.2. In the following sections I will describe in detail those physical principles and individual experimental components which are fundamental for the understanding of the PFM setup.

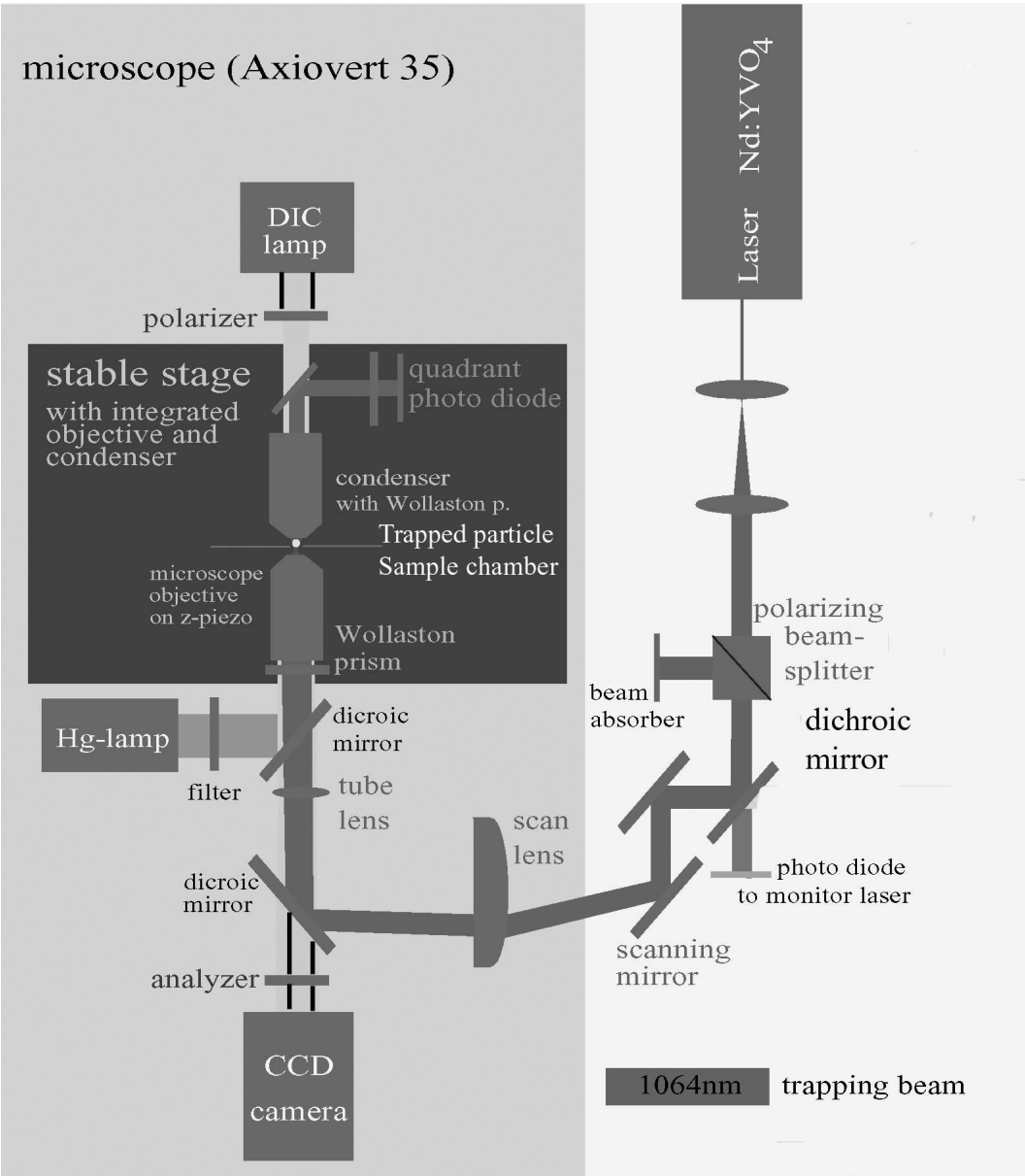

Figure 6.2: Schematic representation of the experimental design for a PFM. The trapping laser beam is first expanded by a system of two lenses. Several mirrors are used to direct the beam into the *Axiovert 35 Microscope*. The laser beam is then directed into the objective lens by a scan lens and a tube lens. The sample chamber is located between the objective lens and the condenser. The lateral position of the sample chamber is controlled by the scanning table (see appendix A.1 for details). Upon leaving the condenser the laser beam is directed onto the QPD by a dichroic mirror. The Axiovert 35 microscope is additionally equipped with differential interference contrast (DIC) optics. At the top of the microscope there is a DIC illumination. At the bottom of the microscope there is a CCD camera which is used to image microspheres and biological samples.

6.2 Position detection of a trapped dielectric microsphere

There have been different attempts to introduce detection systems for optical tweezers. Early attempts were limited to measurements along one axis in lateral direction only. Svoboda *et al.* [63] used an interferometer and polarized laser light to measure position displacements. The idea of using a quadrant photodiode (QPD) to measure two dimensional lateral position displacement was mentioned by Svoboda and Block as described in a review paper in 1994 [62]. By using intense illumination and nonimaging detection, e.g. fast photodiodes, position measurements with a precision on the order of nanometer were performed by Denk *et al.* [19].

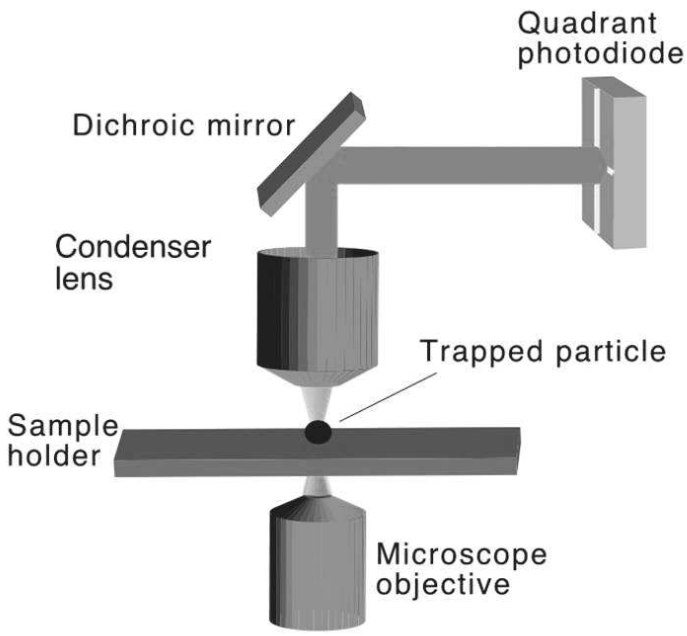

Figure 6.3: Schematic drawing of the experimental setup for the position detection of a trapped particle. A highly focused laser beam enters into the sample chamber. A microsphere is trapped and the laser light is partly transmitted and partly scattered. A condenser lens collects the transmitted and the scattered parts of the laser beam which are finally projected onto a QPD. These two parts of the laser beam create an interference pattern on the QPD.

Our experimental setup uses a QPD for the position detection as illustrated in figure 6.3. A theoretical description of the laser light intensity dis-

tribution which is recorded on the quadrant photodiode was given by Gittes *et al.* in 1998 [27]. Changes in the intensity of the light pattern, which is detected in the back focal plane, were described in terms of interference between scattered and transmitted light (see figure 6.3). This formed the basis for the development of a three dimensional position detection system based on a QPD position detector.

A three dimensional detection system requires three independent signals; one for each dimension. Since the interference pattern from scattered and transmitted laser light is projected onto the quadrant photo diode, one can define two orthogonal position signals as:

$$I_x = (a + c) - (b + d) \tag{6.1}$$

$$I_y = (a + b) - (c + d) \tag{6.2}$$

where a, b, c, d are the four measured signals, one from each quadrant of the photodiode, respectively (see Figure 6.4).

The phase of the axial beam becomes sensitive to the axial particle displacements because of the Gouy-phase shift (see figure 6.5). This inherent property in highly focused beams makes it also possible to measure the axial position of a trapped particle [58]. The signal in this direction corresponds to the total intensity of the laser beam:

$$I_z = a + b + c + d \tag{6.3}$$

The three signals I_x, I_y and I_z define the position of the particle. Since the QPD records the intensity of the incident light in voltage units [V], one must introduce a calibration method in order to translate the voltage signal into units of displacement meters [m]. Thermal position fluctuations of a trapped microsphere are typically on the order of several 100 *nanometers*. It is therefore most convenient to calibrate the position measurement in nanometers [nm]. Different calibration procedures are the subject of the following section.

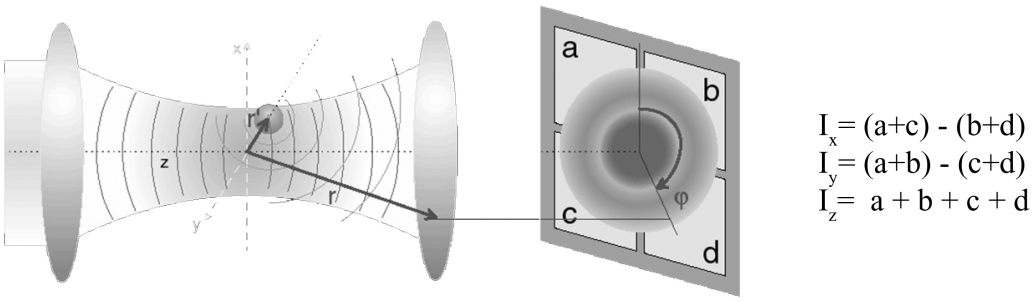

Figure 6.4: Basic mechanism of the three-dimensional interferometric position detection. The interference pattern of the forward scattered and transmitted light is projected onto the quadrant photo diode. The measured voltage signals on each quadrant can be used to construct three independent position parameters (see equations 6.2, 6.3).

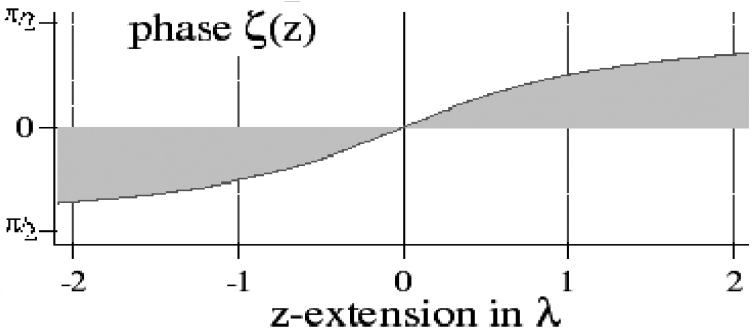

Figure 6.5: Gouy-phase shift. The Gouy-phase shift, also referred to as phase anomaly, is a continuous shift of the phase over the focal region. It is an intrinsic peculiarity of convergent and divergent waves.

6.3 Calibration of the position detector and characterization of the optical trap

A single beam gradient optical trap has its own characteristic parameters which have to be calibrated in order to give a quantitative interpretation of the measured results. There are several ways how to calibrate the detector signal. I discuss different approaches below. The emphasis is given on the calibration method used in my project, where the power spectral density of position fluctuations of a trapped particle is used.

A confined microsphere in aqueous solution behaves as an overdamped harmonic oscillator because of its low Reynolds number. In section 4.1.1 it was shown that the power spectral density for an overdamped particle can be written as:

$$I_x(f) \;=\; \frac{k_B T}{\gamma\,\pi^2\,(f_C^2 + f^2)} \;\equiv\; \frac{I_0}{f_C^2 + f^2}, \tag{6.4}$$

where $I_x(f)$ is the power spectral density, f_C is the Corner frequency, γ is the Stokes drag and $I_0 = k_B T/(\pi^2\gamma)$. $I_x(f)$ is a Lorentzian with respect to the frequency f (see figure 6.6).

Since the position measurement of the microsphere consists of voltage signals that were registered on the QPD, we have to find a calibration factor for converting these voltage signals V into position coordinates x. Let us define the inverse of the detector sensitivity β as:

$$V \;\equiv\; \beta\, x. \tag{6.5}$$

The power spectral density for the voltage signal is obtained from equations 6.4 and 6.5:

$$I_V(f) \;=\; \frac{k_B T}{\gamma\,\beta^2\,\pi^2\,(f_C^2 + f^2)} \;\equiv\; \frac{A}{f_C^2 + f^2}, \tag{6.6}$$

where A has been introduced to simplify the notation. For high frequencies f, that is for $f \gg f_C$, the power spectral density behaves as $1/f^2$. By multiplying the power spectral density $I_V(f)$ by f^2 we can approximate equation 6.6:

$$I_V(f)\cdot f^2 \;=\; \frac{k_B T}{\gamma\,\beta^2\,\pi^2} \;\equiv\; A_{Plateau}, \tag{6.7}$$

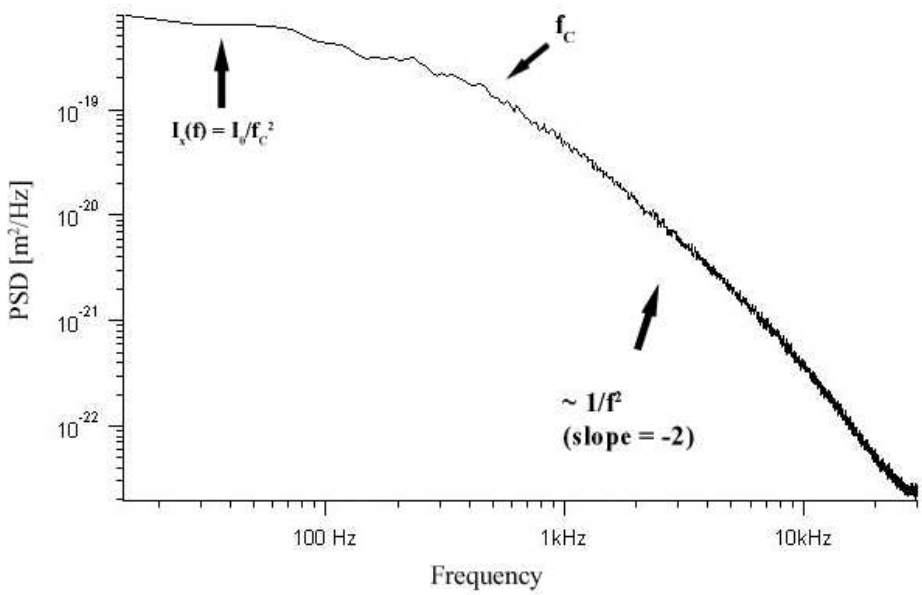

Figure 6.6: Power spectral density of a trapped microsphere. An optically trapped microsphere behaves as an overdamped harmonic oscillator. The power spectral density is a Lorentzian with a characteristic corner frequency f_C. For frequencies lower than f_C the power spectral density is a constant and contains the information about the trap stiffness. For frequencies that are higher than f_C the power spectral density falls off as $1/f^2$. In this regime the microsphere experiences the free diffusion. The bandwidth of the detection system was 70kHz.

where $A_{Plateau}$ is independent of f. The detector sensitivity β^{-1} can then be expressed:

$$\beta^{-1} = \sqrt{\frac{\gamma\,\pi^2\,A_{Plateau}}{k_B T}}, \tag{6.8}$$

The above equation contains only one unknown variable $A_{Plateau}$, which can be determined directly from the measurement of position fluctuations of a trapped particle (see figure 6.7). The remaining constants can be calculated. Therefore one can determine the calibration factor β directly from equation 6.8.

It should be mentioned that the above calibration procedure is valid only when the microsphere is trapped far away from the glass surface, i.e. the distance should be one order of magnitude bigger than the radius of the

bead. If this is not the case one has to include a hydrodynamic correction term in the expression for the Stokes drag γ as:

$$\gamma = 6\,\pi\,\eta\,r\,\epsilon, \tag{6.9}$$

where ϵ represents the hydrodynamic correction factor. It can be expressed in powers of r/h, where r represents the radius of the microsphere and h the distance of the microsphere from the glass surface [29]. The hydrodynamic correction factor varies with respect to the direction of motion. Displacements which are parallel to the surface experience different Stokes drag from those which are perpendicular to the surface. I will denote the hydrodynamic factor for motions parallel to the surface by $\epsilon_{\parallel}$ and for motions perpendicular to the surface by $\epsilon_{\perp}$. A detailed calculation and discussion of the formulas can be found in [29]. An expression of up to the fifth order in (r/h) is provided for $\epsilon_{\parallel}$:

$$\epsilon_{\parallel} = \frac{1}{1 - \frac{9}{16}\left(\frac{r}{h}\right) + \frac{1}{8}\left(\frac{r}{h}\right)^3 - \frac{45}{256}\left(\frac{r}{h}\right)^4 - \frac{1}{16}\left(\frac{r}{h}\right)^5}, \tag{6.10}$$

and an expression up to the third order in (r/h) is provided for $\epsilon_{\perp}$:

$$\epsilon_{\perp} = \frac{1}{1 - \frac{9}{8}\left(\frac{r}{h}\right) + \frac{1}{2}\left(\frac{r}{h}\right)^3}. \tag{6.11}$$

By fitting a Lorentzian to the power spectral density $I_x(f)$ one can determine the corner frequency f_C. It is then straightforward to determine the trap stiffness κ from the relation:

$$\kappa = 2\,\pi\,\gamma\,f_C. \tag{6.12}$$

There is an alternative method to determine the trap stiffness directly from the position fluctuations. A histogram of position fluctuations can be created from the time series as shown in Figure 6.8 and transformed into an energy profile by using the Boltzmann distribution. From the equipartition theorem we also obtain a relation for the trap stiffness:

$$\frac{1}{2}\,\kappa\,\langle x^2\rangle = \frac{1}{2}\,k_b\,T \tag{6.13}$$

$$\kappa = \frac{k_b\,T}{\langle x^2\rangle}, \tag{6.14}$$

where κ is the spring constant and $\langle x^2\rangle$ the root-mean-square displacement of the microsphere from the equilibrium trapping position. Since all power

spectral information is discarded in this approach the presence of specific frequency modes or drift can cause a wrong estimation of the trap stiffness more readily. Therefore it is more reliable to estimate the trap stiffness from equation 6.12 than from 6.14 because one considers also the information from a part of the power spectral density that is not sensitive to mechanical noise or drift.

If a microsphere is moved relatively to a fluid with velocity $\mathbf{v}$, or the fluid is moved relatively to the microsphere with the same velocity, there will be a force exerted on the microsphere. This force is due to the hydrodynamic drag and is usually denoted by F_{Stokes}[1]. The Stokes force must be counterbalanced by the force generated from the optical trap. If it is further assumed that there is a linear relationship between the force exerted on the microsphere and the displacement x away from the equilibrium trapping position we have:

$$\mathbf{F}_{Stokes} = \mathbf{F}_{Trap} = 6\,\pi\,\eta\,r\,\epsilon \cdot \mathbf{v} = \kappa\,x. \tag{6.15}$$

Since the voltage signal is monitoring the position displacement from the equilibrium trapping position there is a linear relationship between the voltage signal V and relative velocity of the fluid $\mathbf{v}$:

$$V = \frac{6\,\pi\,\eta\,r\,\epsilon}{\kappa\,\beta} \equiv Y\mathbf{v}. \tag{6.16}$$

The detector response β can be expressed as a function of f_C and the slope Y, which can be both experimentally determined:

$$\beta = \frac{1}{2\pi f_C Y}, \tag{6.17}$$

Furthermore, if β is expressed in terms of the amplitude A from equation 6.6 we obtain:

$$A = \frac{k_B T}{\gamma \pi^2} \cdot (2\pi Y f_C)^2, \tag{6.18}$$

so that also the viscous drag γ can be determined from the experiment because f_C, Y and A can all be measured. The equation 6.9 defines the relationship between the viscous drag γ and the viscosity η.

[1] I will use this notation in the following.

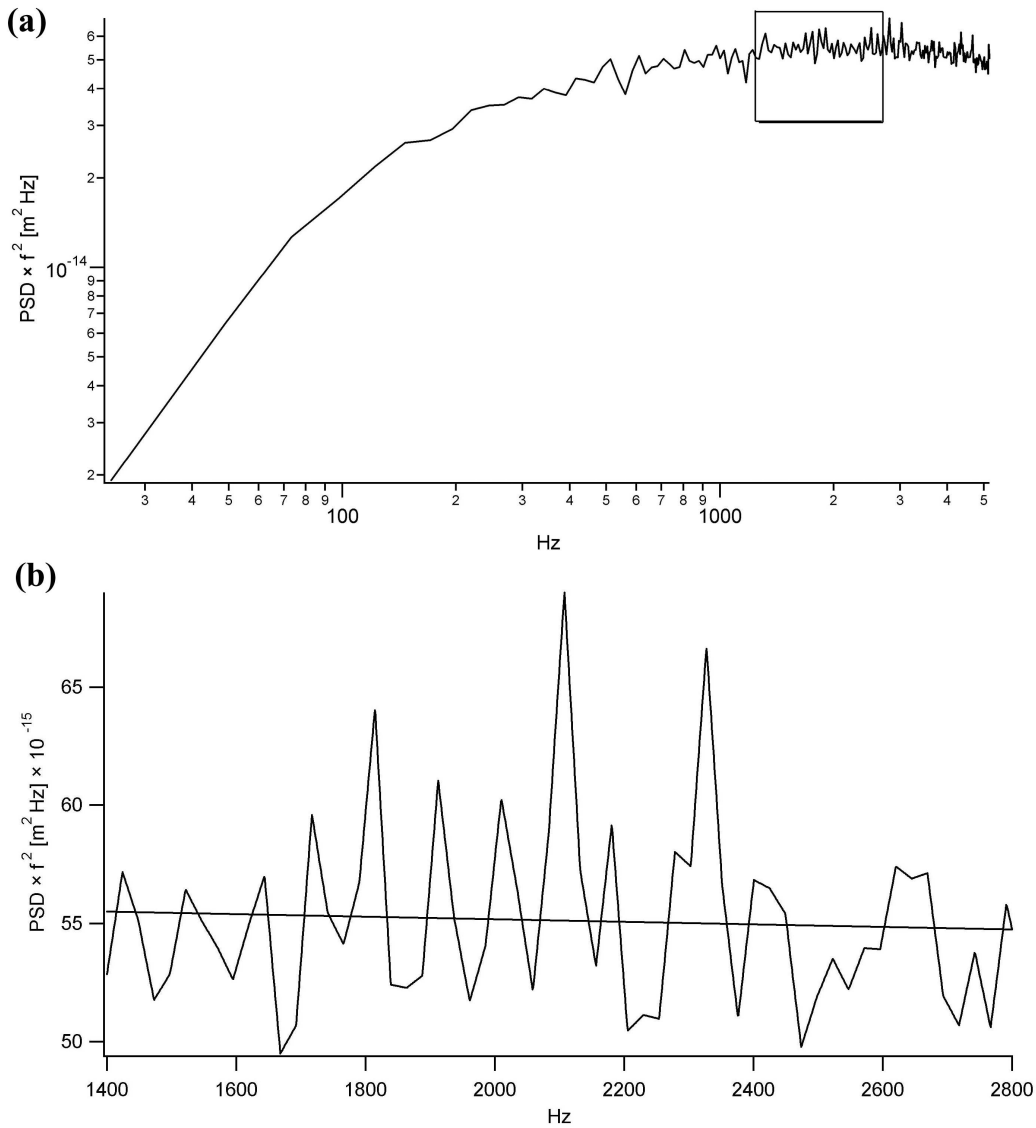

Figure 6.7: Detector calibration via the plateau value $\mathbf{A_{Plateau}}$. (a) The power spectral density of position fluctuations has been multiplied by f^2. A box has been drawn to indicate that part of the spectrum which has a constant value, i.e. it is independent of f. This interval defines $A_{Plateau}$ and is used for the calibration of the optical trap. **(b)** The part of the spectrum defining $A_{Plateau}$ has been magnified. $A_{Plateau}$ is obtained by fitting a line of the form $a + bf$ to the data, where a and b are the sought coefficients determined by the fit. The parameter a defines $A_{Plateau}$ and could be determined with accuracy of better than 1%.

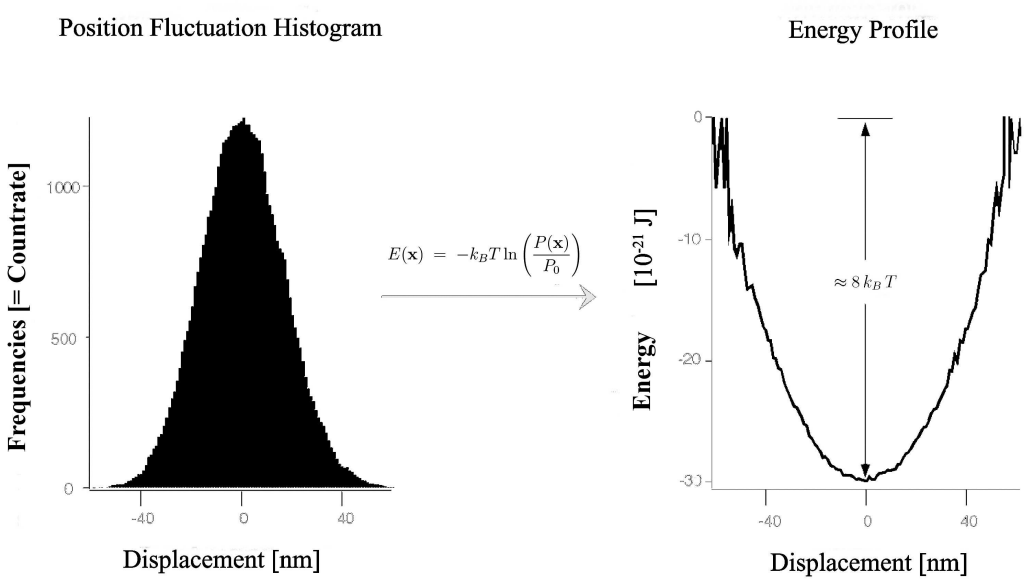

Figure 6.8: Position histograms and energy profiles. (a) A distribution of position fluctuations was calculated from the measured positions. It defines the probability $P(x)$ to find a trapped microsphere at a position x. The origin of the position coordinate coincides with the trapping equilibrium position. **(b)** The energy profile E(x) was calculated from the normalized probability distribution as shown in the formula above.

In this section it was shown how to calibrate the position detector from the measurement of thermal position fluctuations of an individual confined microsphere in bulk solution. This method requires the information contained in the power spectral density of position fluctuations. Since a trapped microsphere can be described by the Langevin equation for an overdamped oscillator the resulting power spectral density is a Lorentzian with a characteristic Corner frequency f_C. For frequencies higher than the Corner frequency, i.e. $f \gg f_C$, the power spectral density falls off as $1/f^2$. By multiplying this part of the spectral density by f^2 one obtains a constant line with a value denoted by $A_{Plateau}$. $A_{Plateau}$ contains the information to calibrate the position detector. This procedure was also used for calibration in my experiments.

Alternative methods for detector calibration do not make an explicit use of the power spectral density. The microsphere is fixed to the glass coverslip and the laser focus is scanned over the microsphere. Since the displacement steps can be well defined on a nanometer length scale it is possible to calibrate the linear detector response. The linear range of the detector response is typically on the order of several hundred nanometers. This method has already been applied in several studies [3, 53].

The characterization of the trap-stiffness can also be achieved in an alternative way which does not require any explicit information contained in the power spectral density. By using the Stokes force on a trapped microsphere, which is moving with respect to the fluid with a well defined velocity, one can characterize the trap stiffness. While the microsphere is in the trap there is a balance between two forces: hydrodynamic Stokes force and the force which is generated by the laser trap. The characterization of the trap stiffness is then achieved by assuming that the optical trap behaves as a linear spring. If the hydrodynamic Stokes force becomes too large, the balance of the forces is disrupted. The microsphere will be dragged out of the trap by the Stokes force and one can determine the maximum force which can be exerted on the microsphere by the laser trap.

6.4 Stability of the experimental setup

In the previous section it was shown how to calibrate the position detector from thermal position fluctuations of a trapped microsphere. However, it was assumed that the detected laser signal reflects solely the nature of the thermal fluctuations. This would be true only in the case if there was no additional source of noise in the experimental setup. The goal of this section is to consider possible sources of noise which can affect the position measurement of a microsphere. Furthermore, an experiment was designed to test the stability of the experimental setup and give an estimation for the precision of our position measurements.

Several types of noise are discussed in some detail below. The emphasis is on the terms with the highest contributions: shot noise, Johnson noise and amplifier noise.

As explained in section 6.2, the interference pattern between the scattered and the transmitted light is detected on the QPD detector. The laser light interacts with the semiconducting material of the detector: the incident photons are converted into electric current by the QPD through creation of electron-hole pairs. The resulting noise which is coming from the QPD is referred to as *shot noise*. Since the creation of electron-hole pairs is a random process governed by the Poisson statistics, the variance in the number of the detected electrons $\langle \triangle n^2 \rangle$ equals its average value $\langle n \rangle$. If we denote the time resolution of the measurement by $\triangle t$, then the bandwidth is simply $B = 1/(2\triangle t)$. Therefore we can write:

$$\langle \triangle n_e^2 \rangle \;=\; \langle n_e \rangle \;=\; \frac{\triangle t\, I_p}{q_e} \tag{6.19}$$

where I_p is the photo-diode current and $q_e = 1,6 \times 10^{-19}\, C$ is the elementary charge. Therefore the variance in the current is the root-mean square of the shot noise $\langle \triangle I_s^2 \rangle$:

$$\langle \triangle I_s^2 \rangle \;=\; \frac{q_e^2\, \langle \triangle n_e^2 \rangle}{\triangle t^2} \;=\; 2\, q_e\, I_p\, B \tag{6.20}$$

where the spectral density of the white shot noise is $2q_eI_p$. The minimal current I_p is referred to also as the dark current which reaches typical values of $50\, nA$ for good quality photo diodes. The dominating part stems usually from the shot noise. At a bandwidth of 100 kHz and an I_p of 5mA one gets a root-mean-square shot noise on the order of tens of nA, which is on the

order of ppm (parts per million) in comparison with the photodiode current I_p.

Since the emitted photodiode current is rather low it has to be amplified, i.e. the electrons have to be transported through electronic circuitry. The resistance offered by the transport material is the source of the so called Johnson noise, which is produced by every resistor because of thermal motion of the electrons. It manifests itself as voltage fluctuations over the terminals of a resistance or as current fluctuations if the terminals are connected by circuitry.

Johnson noise is also white noise with a constant power spectral density which is proportional to the resistance R. The power spectral density of white noise S_ν has a constant value and is given by the following relation (see chapter 4 for a hydrodynamic analogon):

$$S_\nu \;=\; 4\,k_B\,T\,R \tag{6.21}$$

The variance in the current, denoted by $\langle \triangle I_j^2 \rangle$, is then:

$$\langle \triangle I_j^2 \rangle \;=\; \frac{4\,k_B\,T\,B}{R} \tag{6.22}$$

where B is the bandwidth of the detection system. By choosing a very high shunt resistance one can minimize this source of noise. Typically, shunt resistances are in the range of $10\,k\Omega$ - $1M\Omega$. If the bandwidth is 100 kHz this leads to root-mean-square currents $\triangle I_j$ in the range between 10 pA - 1 nA. The resistors produce also noise of their own, which is dependent on the type and quality of the material used for the construction and it is important to choose low noise material for the construction.

Amplifiers have their own internal parts and each one of them is the source of noise. Altogether, the noise produced in an amplifier can be thought of as a combination of shot-noise and Johnson noise. For a high quality amplifier the noise is of the order of 1 nA, which is an order of magnitude less than the shot noise produced by a photo diode.

The position detection depends also on the experimental design. Instead of a single laser one can use two lasers: one for trapping and one for position detection. Such a design would have the advantage to use one laser for measuring the bead position and the other one for the manipulation of the probe. On the other hand, such a system would introduce an additional source of

noise because of relative fluctuations of the one laser beam with respect to the other one.

When focusing a laser beam on a microsphere in aqueous solution several additional sources of noise are introduced. Lasers produce fluctuations in beam pointing, frequency and laser power. Beam pointing stability is the most crucial for position measurements.

Mirrors, the laser and other components of the detection setup show some drift. We estimated the drift by scanning over the beads which were immobilized on the surface. The values obtained were on the order of $1\,\mu\,m/hour$ ($\approx 1\,\mathring{A}/s$). A high quality optical bench was taken in order to reduce these vibrations and drifts.

The rest of this section describes an experiment for characterizing those sources of noisy fluctuations which are not due to thermal noise fluctuations of the aqueous environment. They can be characterized only if the position of the bead is fixed very tightly, i.e. the bead is *effectively trapped* in a much stronger potential than the optical trap can generate. Such a situation can be experimentally realized with sulfate beads, which we found to bind to the *plain glass surface*[1] very strongly.

The experimental procedure to test the mechanical stability is very general and has also been used in the following experiments with individual molecules (see Chapter 7). Therefore I will outline the central stages of this procedure:

1. The bead is trapped by using the computer directed position control of the scanning stage as described in Appendix A.1. The axial trapping position is located very far from the glass coverslip, at least 10 times the bead radius.

2. Position fluctuation data are recorded for several seconds. These data are needed for the calibration of the position detection.

3. The bead is taken towards the glass coverslip by displacing the axial position of the laser focus.

4. Finally, the bead binds to the glass surface when coming into contact with the surface.

[1]Neither proteins nor any other biomolecules were attached to the glass surface.

The binding event of the bead is detected by the reduction of the axial position fluctuations. When a contact between the bead and some other surface is formed the position fluctuations have to significantly decrease along the axial direction. Because the fluctuation space is several hundred nanometers along the axial direction for a trapped bead, there is a significant reduction in the axial fluctuations upon binding to the surface (see figure 6.9). The position fluctuations of a bead, which is trapped but not bound to the surface, are approximately 100nm peak to peak. Upon binding to the surface, the position fluctuations decrease by an order of magnitude to about 10nm. Because of optical reasons the precision along the vertical axis is worse than the precision along the lateral axis. Therefore we cannot resolve position fluctuations significantly below 10nm along the axial direction. This is an upper estimate for the actual position fluctuations of the bound bead.

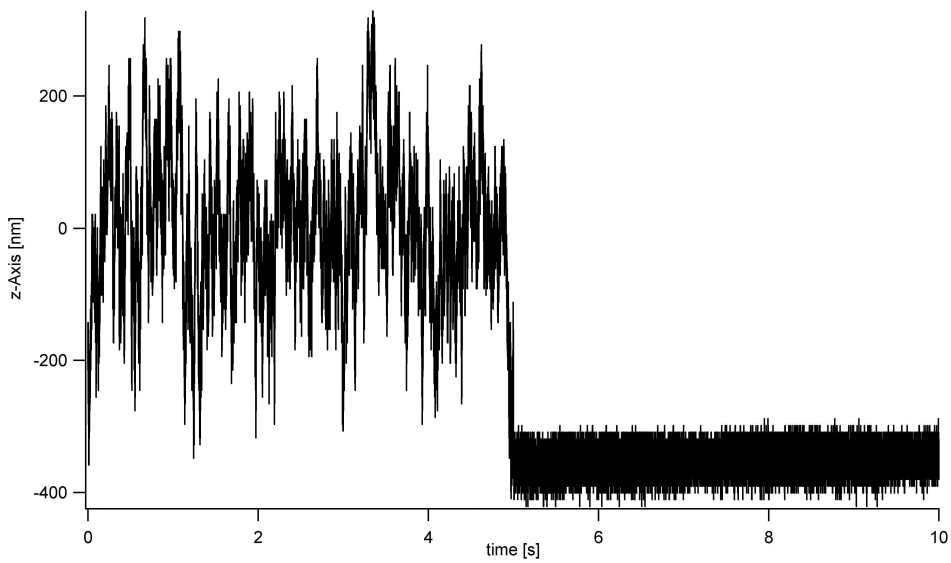

Figure 6.9: Axial position fluctuations of a trapped bead reveal the binding event. Position fluctuations in the axial direction of a trapped bead are shown in the figure above. The point of discontinuity defines the binding event of the bead to the glass surface. The peak to peak magnitude of the position fluctuations for a trapped bead above the surface is on the order of 100nm and for the surface bound bead it is below 10nm.

This is not the case for the lateral position fluctuations. As shown in graph 6.10, the lateral position fluctuations also decrease significantly after binding to the surface.

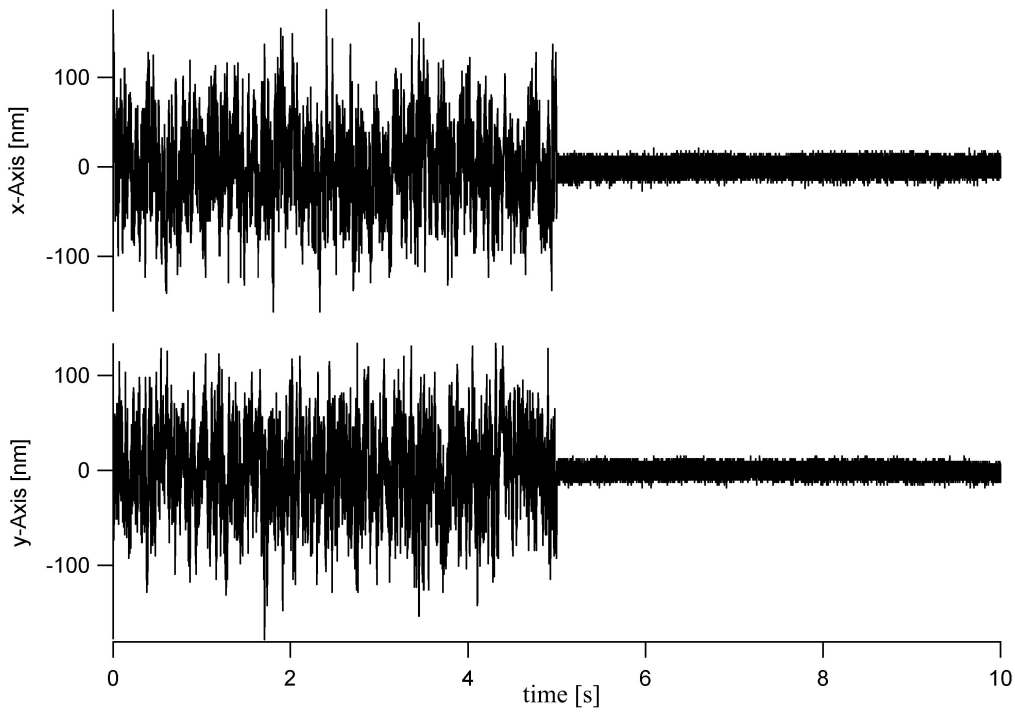

Figure 6.10: Lateral position fluctuations of a trapped bead before and after binding to the glass surface. The above graph shows the lateral position fluctuations of a bead. The bead is initially confined in the laser trap, which is faraway from the surface (approximately $10\mu m$). Position fluctuations are on the order of 100nm in peak to peak magnitude. The right half of the graph shows the lateral position fluctuations of a bead which has bound to the glass surface after the optical trap has been displaced towards the glass surface. The lateral position fluctuations have decreased in magnitude by more than one order of magnitude.

One can represent the lateral position fluctuations as a two dimensional histogram. A procedure was written by using Igor software in order to transform the data from a wave representation into a 2D histogram. Such a representation is advantageous because it gives a first estimation for the strength of binding to the surface. Furthermore, one can easily spot the presence or lack of symmetry in the measured position fluctuations (see Figure 6.11).

The relevant parameter for the estimation of the mechanical stability of the experimental setup is the magnitude of the lateral position fluctuations. We have already shown in the section 6.3 that the position fluctuations of a trapped bead take a Gaussian form. This is also true for the case when the bead binds to the molecularly prepared surface (see section 7.1 for further

information). There are two equivalent possibilities to estimate the width of the lateral position fluctuations:

- A two dimensional Gaussian fit to the 2D position fluctuation histograms (see figure 6.11).
- Extraction of a one dimensional position fluctuation profile and subsequently fitting one dimensional Gaussian to it (see figure 6.12).

The data was fitted according to the procedures described above. On a time scale of 10s a standard deviation of 5nm was obtained for the sulfate bead which was immobilized onto the glass coverslip by adhesion. For comparison, the lateral fluctuations of the same bead, which was trapped far away from the surface, were 64nm. The contribution of background noise and drift on total lateral position fluctuations, as measured by our experimental setup, is less than 1nm in magnitude. Therefore it is reasonable to conclude that the measured position fluctuations are due to thermal excitations and not to other possible sources of noise.

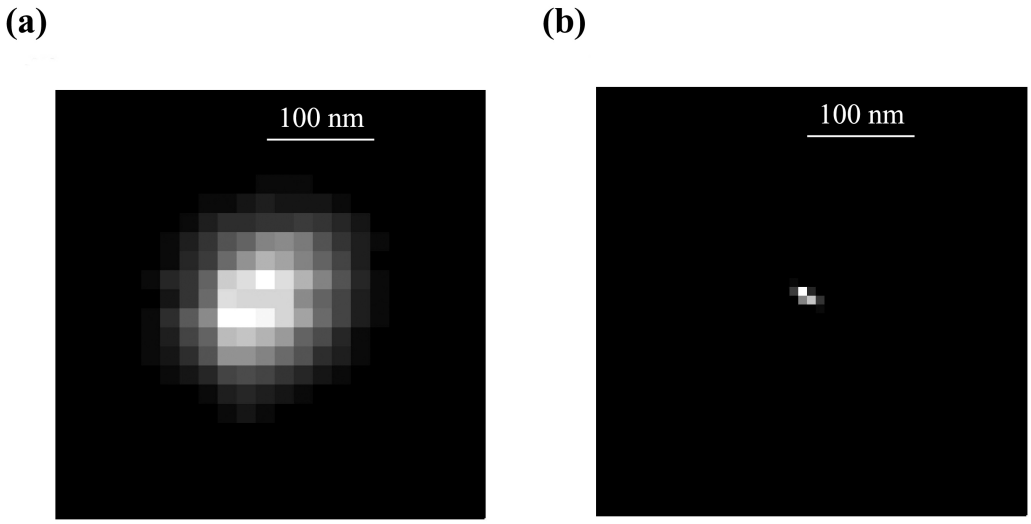

Figure 6.11: 2D histograms of lateral position fluctuations. The position fluctuations are recorded as one-dimensional time traces along each axis. A representation in form of two-dimensional histograms displays the symmetry or lack of symmetry in the recorded data. **(a)** The bead is confined only in the optical trap. **(b)** The bead has bound to the surface.

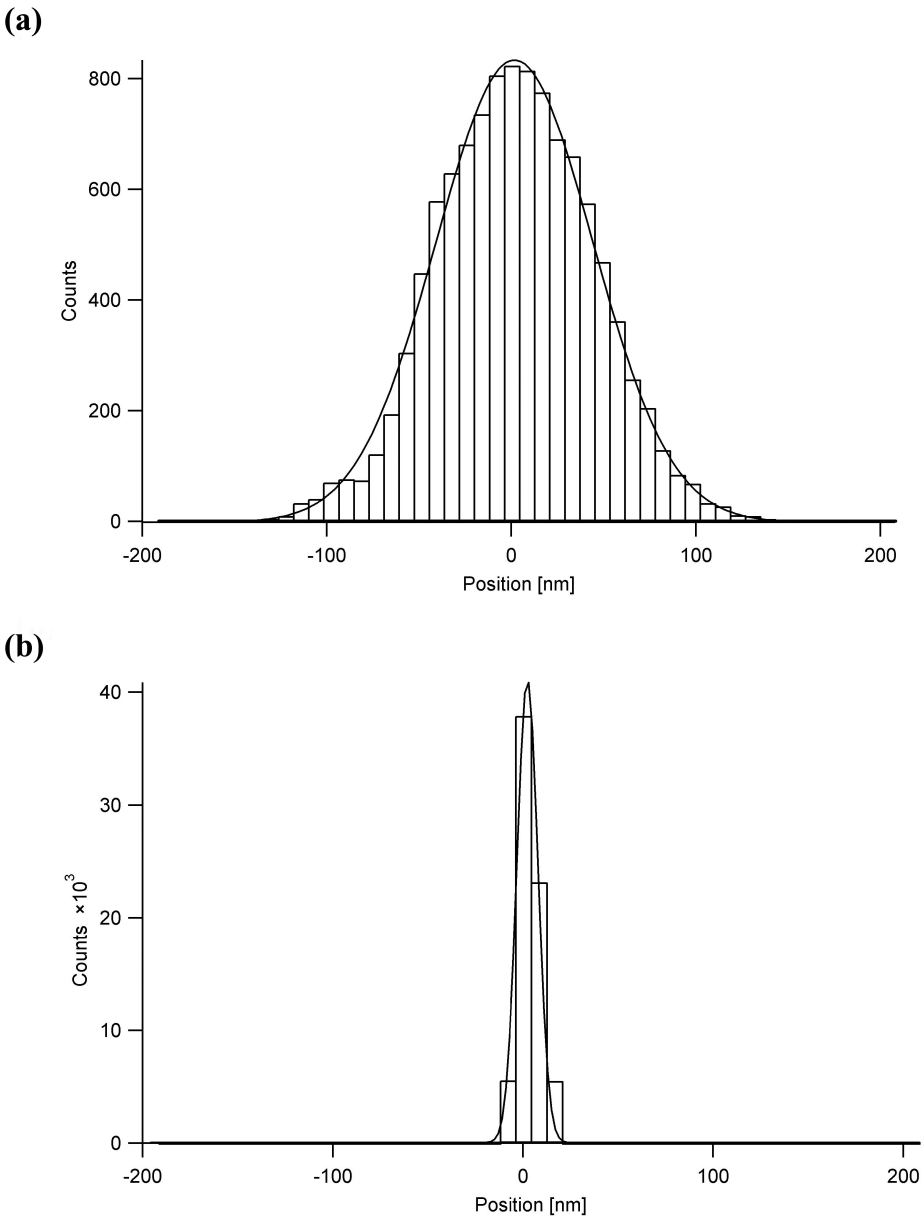

Figure 6.12: 1D lateral position fluctuations profile. The 1D position fluctuation profiles were extracted from the 2D position histograms. **(a)** The trapped bead is far away from the surface. **(b)** The bead has bound to the surface. The position distribution histograms were fitted with a Gaussian. The width of the fitted curve is: **(a)** 64nm and **(b)** 5nm.

In summary, we have discussed different sources of external noise which can affect a position measurement of an optically trapped microsphere in aqueous solution. It was estimated that the experimental setup experiences a drift of ca. $1\,\mathring{A}/s$.

An experiment was designed in order to estimate the stability and the precision of our experimental setup. The strong binding property of sulfate covered polystyrene microspheres was exploited in order to estimate the effect of background noise in the experimental setup. These beads bind very strongly to the glass surface. The magnitude of lateral position fluctuations has been determined by fitting a Gaussian to the position fluctuation profile. The lateral position of a bound bead could be estimated with an accuracy of $\pm$5nm over a time scale of several tens of seconds. We take this value as an upper estimator for the accuracy of the lateral position measurement.

Chapter 7

Experiments on Individual Molecules

Most of quantitative biochemical and biological experiments are performed on an ensemble of molecules. The properties of individual molecules are then inferred circumstantially from averaged macroscopic values obtained from these experiments [8]. With the introduction of scanning probe microscopies (SPM) and powerful optical methods [5, 11, 62], a possibility to observe and to manipulate individual molecules was created. These experimental techniques have opened a new and exciting interdisciplinary field which is situated at the interface between physics and biochemistry.

A very common question is raised by experts from other disciplines: *"When is molecular individuality important?"* For example, experiments in high energy physics deal with elementary particles. They are believed to behave in identical manner because they possess no internal structure. In high energy physics the experiments are designed to detect these particles as discrete individual events. Since the events are expected to occur with a very low probability, one can describe the occurrence of events as a stochastic process with a stochastic variable which obeys the Poisson probability distribution function. Therefore the average behavior and the variance are described by the same parameter. The Gaussian probability distribution function is the limiting case of the Poisson probability distribution function for a large number of detected events.

A similar description is also possible in biological sciences if one wants to observe events with a very small probability of occurrence. However, molecules — and especially biomolecules — have an extended three dimensional structure, which shows a remarkable degree of complexity. Consequently, the be-

havior of these molecules is often very complicated because the individual components do not necessarily behave in the same way. There reasons for the origin of complex molecular behavior can be divided into two classes: a molecule has either a very complicated structure or it has a simple structure but is a part of a very complex environment. Both factors can be also present simultaneously, as exemplified by the cell and its constituents.

Individual biomolecules can range in size over several orders of magnitude: from microns to several nanometers. Since biomolecules and biomolecular complexes perform specific functions in living organisms, they provide a natural example for *molecular machines*. Our understanding of biomolecular function and structure has been largely shaped by biochemical and structural analysis. Therefore the understanding and characterization of individual building blocks at the level of individual molecules is necessary for further development.

Different techniques were used to measure properties of individual biomolecules. On the one hand there are optical techniques for observation of suspended individual biomolecules in bulk solution and on the surfaces immobilized molecules. The molecule species of interest is labelled by fluorescent markers. In combination with a microscope one can then study conformational dynamics or diffusive properties on the scale of individual molecules [45, 46]. On the other hand there are methods for mechanical characterization of molecules. Here, the molecule species of interest is immobilized on a surface in order to apply a force to it. These techniques include atomic force microscopy (AFM) [11], optical tweezers or photonic force microscopy (PFM) [7, 62], scanning tunneling microscopy (STM) and bioforce probes (BFP) [21, 44]. These experiments have in common that the force and the distance are measured along the same axis. The application of an external force to the molecule will result in the deformation of the molecule. The aim of our work was to develop a method to characterize the nature of the molecular contact at the level of individual molecules and to minimize external perturbations which are induced on the observed molecule by the experimental technique.

This chapter has been divided into two parts. In the first part, section 7.1, I establish a method which characterizes the molecular specificity of the binding contact between molecularly prepared glass coverslips and polystyrene microspheres. A model system, consisting of receptor avidin and ligand biotin, was chosen for this purpose. The second part of this chapter, section 7.2, is an application of the newly developed method to measure the mechanical properties of an individual SNARE complex.

7.1 Avidin-Biotin model system

There are several reasons for choosing the ligand-receptor pair consisting of biotin and avidin as a model systems. First, the interaction has already been experimentally studied with *conventional* biochemical methods on the one hand and at the *single molecule* level on the other hand [24, 44, 47]. These measurements were accompanied by theoretical studies and simulations [9, 20, 33]. Second, both molecules are robust against changes in chemical and mechanical parameters; they are relatively easy to handle. Finally, the dimension of the complex is very small even by protein standards. Avidin molecule is a tetramer. Each monomer consists of eight strands of β-sheets which form together a β-barrel (see figure 7.1). Biotin is a comparatively simple molecule. Its structure is also shown in figure 7.1.

7.1.1 Sample preparation

Glass coverslips[1] were initially thoroughly cleaned. Afterwards, they were stored in a glass container and were held in a vertical position by a specially designed teflon holder. In this respect, great care was taken in order to prevent unwanted adsorbate from assembling on the surface of a freshly cleaned coverslip. The glass container was also needed during the cleaning procedure which is summarized by the following protocol:

1. Glass coverslips were immersed in 2% Helmanex solution.

2. They were put in an ultrasound bath for 15 minutes.

3. 2% Helmanex solution with remaining adsorbates[2] was washed for approximately 5 minutes by bi-distilled water from Milipore-Filtering-System. Afterwards the liquid was exchanged with clean water twice, each time washing the coverslips for approximately 5 minutes.

4. Glass coverslips were immersed in clean water and put in the ultrasound bath for 15 minutes.

5. The same procedure as under step No. 3 was repeated.

[1] Glass coverslips were ordered from the company Marienfeld. They measured 15mm in diameter. They carry a label according to the hardness of the material: *Nr.1*

[2] Adsorbates consisted of lipids and other molecules which were washed from the glass surface by ultrasound bath.

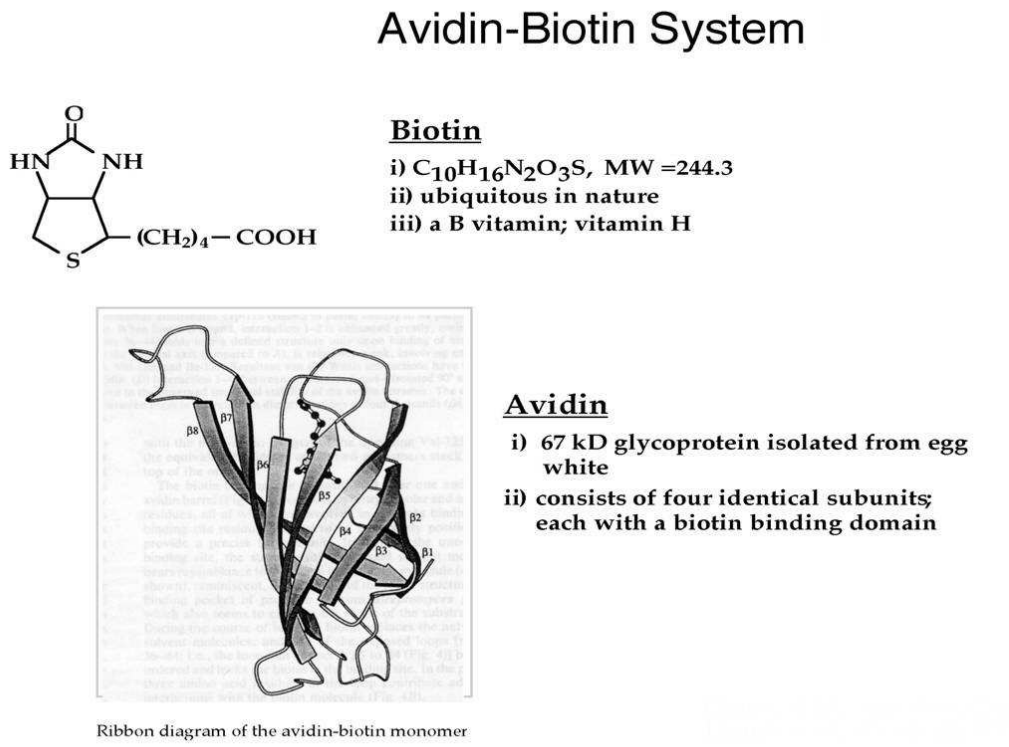

Figure 7.1: Molecular structures of avidin and biotin. Biotin is a very small molecule whose chemical formula is shown at the top of the picture. A monomer of avidin is shown above. It has a β-barrel like structure, which enables a biotin molecule to enter into the specially designed pocket. This interaction is energetically stabilized by a formation of several hydrogen bonds between the two molecules. Avidin appears in nature as a tetramer. The size of the molecule is estimated from its crystal-structure to ca. 7nm [42].

The above procedure was applied several times before the coverslips were dried and stored. The glass holder containing the coverslips was put into an oven which was held constantly at 70° Celsius. It was left there to dry overnight and collected on the next day for storage.

The next step consisted of properly functionalizing the coverslips with desired molecules. I chose to functionalize the surface with biotin molecules and keep avidin molecules on latex beads. In this way, a dilution series could be performed on the concentration of biotin (see section 7.1.2). Biotinylated-BSA[3] was diluted at a concentration of 2mg/ml in PBS buffer. The reason for choosing BSA was twofold. On the one hand, BSA screens off unspecific electrostatic interactions between the coverslip and bead. On the other hand the adhesion of BSA to glass is very strong, a necessary condition for an experimental assay designed to mechanically probe the properties of individual molecules [12].

Furthermore, a procedure for immobilizing biotinylated-BSA on the glass surface was established. Droplets of $100\mu l$ were used to cover the glass surface in a uniform manner. Prepared coverslips were deposited into a plastic dish, which was covered with a wax film for easier handling of coverslips. The plastic dish was closed and sealed. This was followed by a 2 hours long incubation at 37° Celsius and a constant humidity of 70%. Finally, the coverslips were washed with PBS (see appendix B.1).

Latex beads used in this experiments were $1\mu m$ in diameter. They were supplied by Molecular Probes. NeutrAvidin molecules were covalently coupled to the surface of the latex microsphere. The density of avidin on the surface of polysterene microspheres can be calculated from the saturation data with biotin. 7.69 nmol of biotin is needed to saturate 1 mg of Neutravidin coated microspheres[4]. The number of microspheres — denoted by N_{Beads} — which are contained in one milligram can be estimated:

$$N_{Beads} = \frac{m_{total}}{m_{bead}} = \frac{m_{total}}{\rho_{polystyrene} V_{bead}} = \frac{m_{total}}{\rho_{polystyrene} \times \frac{1}{6}\pi\,\phi^3} \tag{7.1}$$

where:

- m_{total} = the total mass of microspheres involved in the reaction (1mg).

[3]BSA - Bovine Serum Albumin

[4]See the official technical product specifications from the supplier of our beads: Molecular Probes, Inc

- m_{bead} = the mass of an individual microsphere
- V_{bead} = the volume of an individual microsphere
- ϕ = diameter of microspheres in μm
- $\rho_{polystyrene}$ = density of polymer in g/ml (1.05 for polystyrene, i.e. latex)

By substituting the numerical values into the equation 7.1 I obtain for N_{Beads}:

$$N_{Beads} = \frac{1mg}{1.05 \times 10^{-9} mg/(\mu m)^3 \times \frac{1}{6}\pi\, 1\mu m^3} = 1.82 \times 10^9 \tag{7.2}$$

7.69 nmol of biotin molecules corresponds to 4.6×10^{15} biotin molecules. Therefore, there are N_{BB} biotin molecules which are on average needed to saturate all active avidin binding sites per individual bead:

$$N_{BB} = \frac{4.6 \times 10^{15}}{1.82 \times 10^9} = 2.53 \times 10^6 \tag{7.3}$$

An individual NeutrAvidin molecule is coupled to the bead as a tetramer: therefore there are four biotin binding sites per one NeutrAvidin molecule. Due to steric hindrance of NeutrAvidin molecules on the surface of the bead, it is very likely that there are on average less than four active binding sites per individual NeutrAvidin molecule[5]. Thus, I will estimate the surface density of active biotin binding sites by assuming either three (ρ_{BS}^{Max})or four (ρ_{BS}^{Min}) active biotin binding sites per NeutrAvidin molecule. First, by combining the preceding considerations and equation 7.3, we obtain an estimation for the number of NeutrAvidin molecules per individual microsphere:

$$N_{Avidin}^{Max} = 8.4 \times 10^5 \tag{7.4}$$

$$N_{Avidin}^{Min} = 6.3 \times 10^5 \tag{7.5}$$

The surface area of a bead, which measures 1μm in diameter is:

$$S = 4\pi \times (0.5\,\mu m)^2 = \pi \times 10^6\, nm^2 \tag{7.6}$$

Finally, I can estimate the surface density of active biotin binding sites on the latex beads ρ_{BS}:

[5]Private communication with the supplier of the beads: Molecular Probes, Inc.

$$\rho_{Avidin}^{Max} = \frac{N_{Avidin}^{Max}}{S} = \frac{1}{\pi \times (1\,nm)^2} \tag{7.7}$$

$$\rho_{Avidin}^{Min} = \frac{N_{Avidin}^{Min}}{S} = \frac{1}{\pi \times (1.3\,nm)^2} \tag{7.8}$$

The surface density of active biotin binding sites is then approximately 1 molecule per circle with a radius of 1nm. As we can see, the surface of the microsphere is tightly packed with avidin molecules.

In summary, we have estimated the number of NeutrAvidin molecules which were coupled to the latex microspheres from the saturation concentration of biotin molecules. The estimated surface density of one active biotin binding site per circle area with a radius of 1nm indicates that the surface of the microsphere is tightly packed with NeutrAvidin molecules.

7.1.2 Molecular specificity of the interaction

A homogenous molecular monolayer on the surface of a microsphere and on the glass coverslip is a prerequisite for successful mechanical experiments with individual molecules. In this way it is guaranteed that the interaction between the probe and the surface is due to the formation of molecular bonds. Since the experiments with optical tweezers are very time consuming, it was necessary to develop an alternative and faster method for establishing the quality of molecular surface functionalization. The underlying idea was to follow the kinetics of the binding of avidin coated beads to the surface. The beads were diluted in PBS to the same concentration as used in the experiments with optical tweezers. A droplet of the bead solution was then added to the functionalized coverslip. After a well defined time interval the reaction was stopped by washing the coverslip with PBS; all non-bound beads were removed. Subsequently, the surface bound beads were imaged by wide field fluorescence microscopy. Five pictures, chosen at random, were taken with each sample by an Axiocam camera (Zeiss, Germany). A typical result is shown in Figure 7.2.

A procedure was developed to automate the indentification and count the beads by using available software packages from Igor[6]. The applied routine contains an algorithm for fitting Gaussian profiles to each identified particle.

[6]This software package is supplied by Wavemetrics, Inc., USA

The results are shown in Figure 7.3.

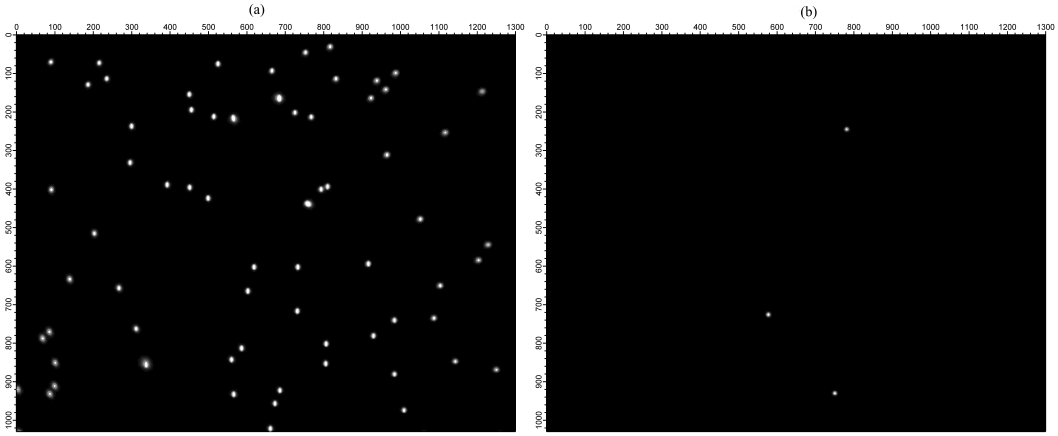

Figure 7.2: Molecularly specific and unspecific adsorption of avidin coated polystyrene beads to BSA-biotin coated glass coverslips. The figure shows photographs of fluorescent microspheres measuring $1\mu m$ in diameter. The microspheres were coated with NeutrAvidin. The above snapshots were taken 30 min. after the microspheres have been injected into the sample chamber. **(a)** The photograph shows a fluorescent image of microspheres which bound to the glass surface covered by biotinylated-BSA. **(b)** This snapshot shows the negative control experiment: the glass surface was covered only with BSA.

The data in Figure 7.3b reflect three processes simultaneously at work. The initial phase of the graph is dominated by the diffusion and sedimentation process of beads. Since the dilution of beads was considerable there are only a few beads per field of view of observation area which manage to reach the surface during the first 15 min. of the adsorption process. The error bars are correspondingly bigger for early detected points. Second, once the beads have reached the surface they can bind to the surface. The interaction potential is affected by the presence or absence of biotin molecules on the surface. One can define a specificity as the difference after the same time interval in the number of adsorbed beads between a glass coverslip coated with biotinylated-BSA and a glass coverslip coated only with BSA. After approximately 30 min. this specificity reaches its maximum value of 90% (see Figure 7.3b). Third, as reaction progresses in time the magnitude of specificity starts to decrease. This effect is due to increase in the amount of unspecifically bound beads. Hence, the unspecific interaction gains in importance with respect to the specific interaction as time of the reaction increases.

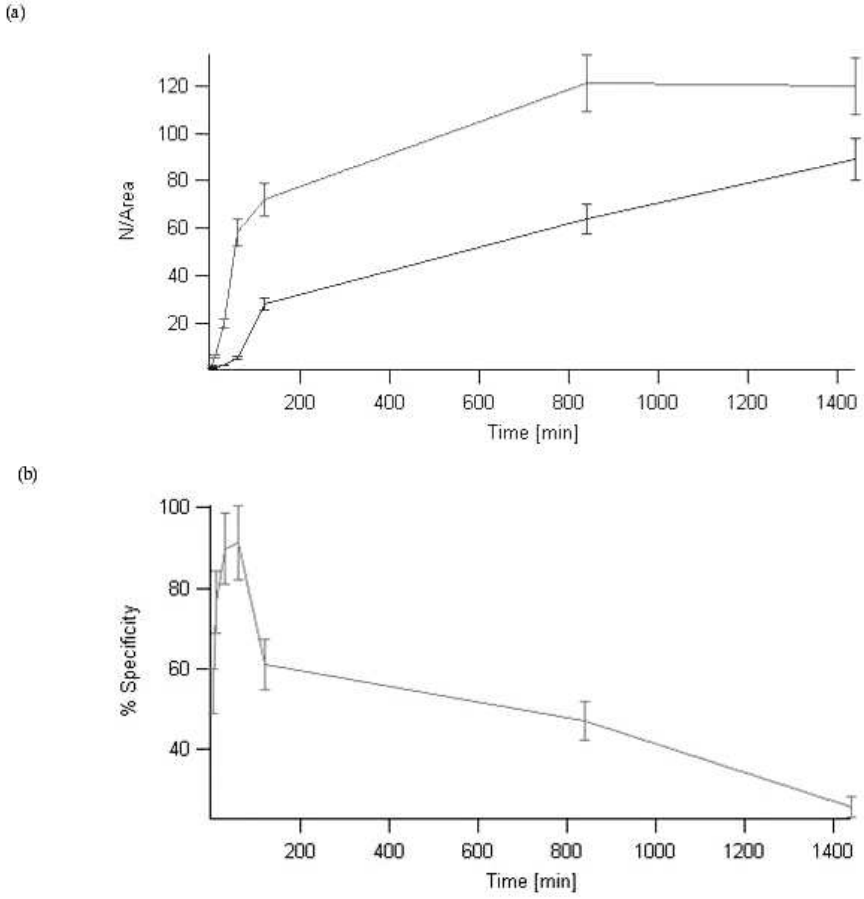

Figure 7.3: Kinetics of adsorption of avidin coated beads. The average value of bound microspheres is shown as a function of time. **(a)** The upper curve represents the dynamics of avidin coated microspheres binding to the biotin-functionalized coverslip. The lower curve shows dynamics of the negative control experiment; no biotin on the glass coverslip. **(b)** A *specificity* was defined as the fraction of beads which bound to the biotin-functionalized surface with respect to the total number of bound beads. The specificity reaches its peak of 90% after approximately 30 min. The error bars shown in the graph arise from the statistical analysis of the data. The magnitude of the error bar is $1\ \sigma$.

In summary, the first experimental goal of preparing a specifically coated glass coverslip was achieved. Furthermore, the kinetics of specific binding of avidin coated beads to this molecularly functionalized glass coverslip was quantitatively characterized. A remarkable specificity of 90% in peak value was achieved with this assay. The contribution of the unspecific interactions becomes the dominant factor for longer incubation times. The time interval of two hours is therefore an upper estimate for achieving molecularly specific binding with this method.

7.1.3 Preliminary experiments with avidin-biotin

Instead of letting avidin coated microspheres to diffuse freely towards the surface and bind one can also use optical tweezers. The main advantage to perform this experiment by optical tweezers is the ability to localize the position of the microsphere on a $100nm - 1\mu m$ scale and to bring the microsphere into close contact with the surface in a controlled manner. After the bead has been trapped one can displace the laser focus along the vertical axis in well defined steps on the order of magnitude of 10nm (see chapter 6)[7]. Thermal position fluctuations of the bead were then recorded on the quadrant photo diode. The trapping of the bead was always performed in the bulk solution. The distance to the surface was approximately 10 times the radius of the microsphere; typically several μm. Hydrodynamic couplings between the microsphere and the surface were excluded (see section 6.3).

After the calibration procedure was performed, the trapped bead was displaced in small steps of 10 -50 nm towards the glass surface. The glass surface was coated with biotin molecules as described in section 7.1.2. When the bead reached the surface, it bound to the glass coverslip in a discrete step. A recorded time trace of position fluctuations during this process is shown in Figure 7.4.

After the bead has been successfully brought into contact with the surface a question arises whether such a contact can also be ruptured by applying force to the bead. A constant force of 10 pN was defined by displacing the laser focus vertically away from the surface. The time to rupture the contact under this force was measured. The results of this experiment are shown in Figure 7.5. To our surprise we found that there were two phenomenologically different groups appearing in the spectrum, whereas only one continuous his-

[7]The individual settings for the vertical step size can vary.

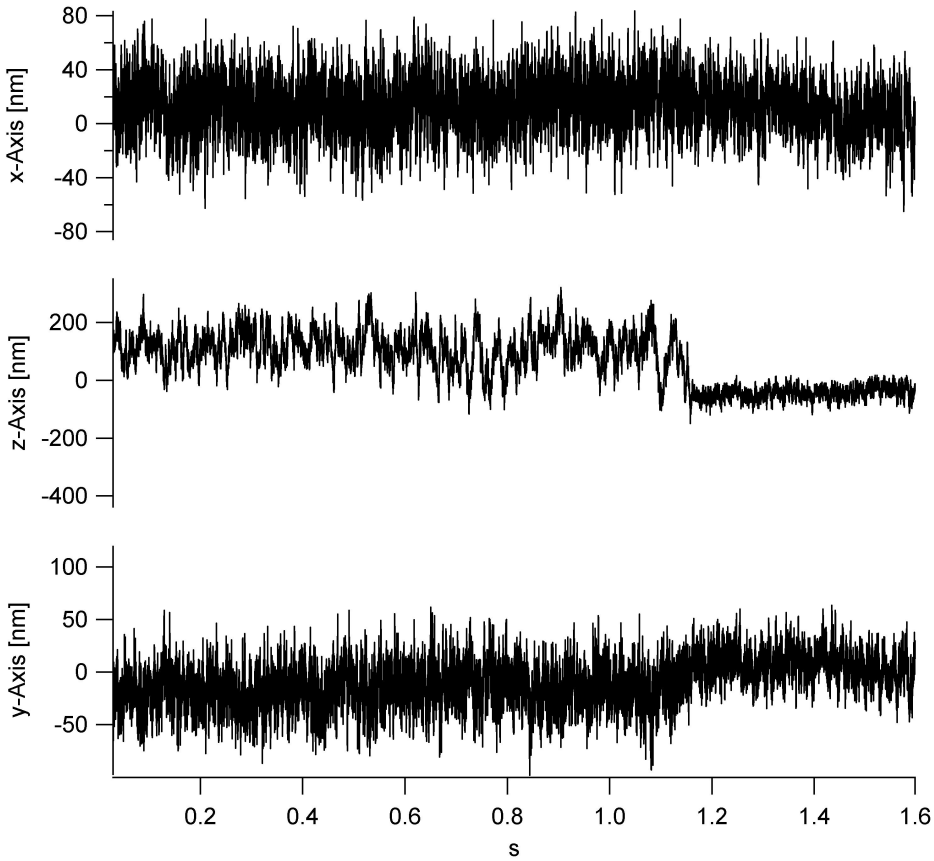

Figure 7.4: Formation of a specific molecular contact. The bead was held in the optical trap while the vertical position of the laser focus was displaced in steps of 25nm towards the coverslip surface. When the bead forms a contact with the surface the magnitude of fluctuations along the vertical (z-axis) is considerably reduced and appears as a discrete event. The time resolution of the position measurement was $10\,\mu s$. The fluctuations in the lateral direction remain essentially unaltered after the bead has bound to the surface.

togram would be expected if the interaction was due to a single avidin-biotin pair. The first group shows a significant variance with respect to time. The second group consists of a single histogram and contains all those beads which could not be ruptured after 2 min of constantly applying force. The question is then: *"What causes the beads to behave in at least two completely different ways while the experimental circumstances have not been altered?"*

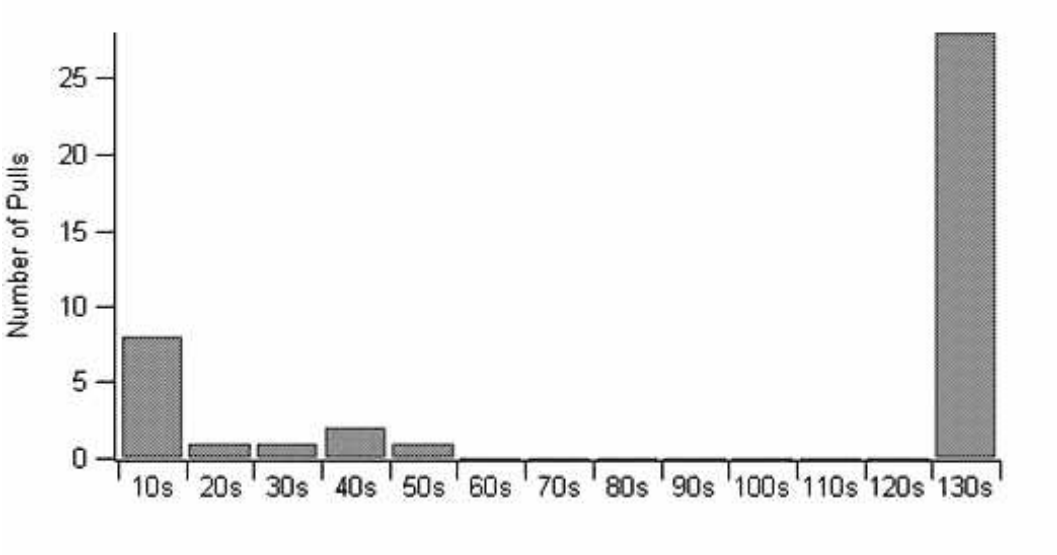

Figure 7.5: Number of ruptured contacts as a function of time. A constant force was applied to a bound bead by displacing the laser focus along the vertical direction. The force was held constant when applied to different beads. The number of ruptured surface contacts in the histogram has been measured as a function of time. There are two different phenomenological groups of surface contacts. One group could be pulled away from the surface by rupturing the contact. The other group, which contains the majority of the beads, could not be ruptured within 2 min. of constantly applying force to the bead.

7.1.4 Molecular specificity measured by optical tweezers

One of the main reasons to use optical tweezers was that by trapping a small bead one can restrict diffusion of the bead to a small volume. The thermal fluctuations of a trapped bead are restricted to several hundreds of nanometers. On the contrary to the experiments described in section 7.1.3, one can bring the bead into close proximity with the surface in a controlled manner

(see Figure 7.6). The bead requires a certain amount of time before it binds to the surface. The experiments described in this section show that the time needed for the binding reaction is a function of molecular surface coverage. Furthermore, by applying the theoretical description described in section 4.2 we estimate the effective size of the molecular binding center at medium surface coverage. The estimation is in good agreement with the size of the molecule as estimated from the structure of the molecule.

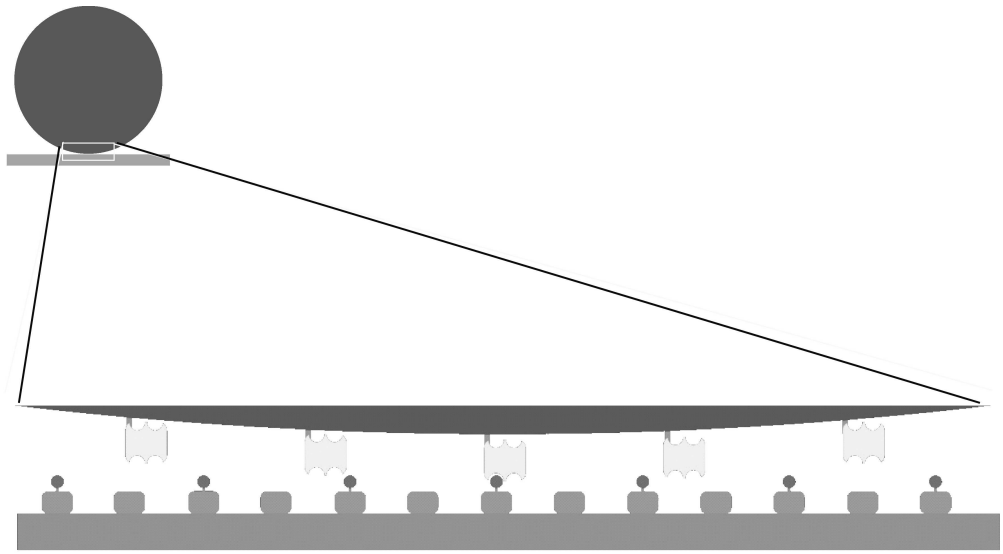

Figure 7.6: The local geometry between an avidin coated bead and a BSA-biotin coated glass surface. The graph shows the local geometry in an experiment with microspheres measuring $1\mu m$ in diameter and optical tweezers. In the left corner there is an illustration of a bead which has bound to the surface. The region of contact has been magnified and displayed at the bottom of the picture. Avidin molecules are attached to the microspheres. BSA molecules have been immobilized on the glass surface by adsorption. Biotin molecules were covalently attached to the BSA molecules. On average, there were 8 Biotin molecules per individual BSA molecule.

The experimental procedure for molecular surface functionalization was identical to the one developed in section 7.1.1. A dilution series of biotinylated-BSA with pure BSA was performed prior to the incubation. Diluted biotinylated-BSA was immobilzied on the glass surface by following the same incubation procedure as described in section 7.1.1. This procedure defines the surface in two important aspects. First, only a fraction of the molecularly functionalized surface can act as a specific binder for avidin molecules. This is necessary if

one is to determine the specificity of a reaction. Second, the concentration of BSA molecules was kept constant, only the concentration of biotin molecules varies through the dilution series. The glass surface was always completely covered with BSA molecules.

Avidin molecules were immobilized on the latex beads. The same beads, as in experiments described in section 7.1.1, were used also in this experiment. The radius of the beads was 500nm.

The binding part of the experiment was performed in three steps. First, the bead was captured sufficiently far away from the surface, i.e. several microns. Thermal position flcutuations were measured and used to perform a position calibration in nanometers. Second, the bead was displaced in large steps towards the surface by changing the position of the laser focus. It was still held far enough from the surface, several hundred nanometers, to prevent a binding reaction. Third, the final steps in approaching the surface were 25nm long, much smaller than the thermal position fluctuations of a trapped bead along the vertical axis.

A series of 15 independent measurements (beads) was chosen representative for each surface coverage. The reaction time is defined as the time needed for binding after the focus has been displaced in such a way that the diffusion space of the trapped bead and the molecularly covered glass surface intersect. The results were averaged over all independent measurements for a specific surface coverage. They are shown in figure 7.7.

What do these data tell us about the molecular specificity of the binding reaction? We considered a model in section 4.2 which describes the connection between a local geometry of the reaction to the mean time of binding. We recall the general expression for $\tau^{(n)}$ from the section 4.2:

$$\tau^{(n)} = \frac{r^2}{D^{(n)}} \cdot \mathrm{f}^{(n)}(r/q) \tag{7.9}$$

where (n) is the dimensionality of the diffusion space, r is the diameter of the large diffusion space and q is the diameter of the small molecular target.

In the case of a full surface coverage with biotin, the reaction time is so short, that we could not resolve any significant details in time. This is not the case for lower surface coverage, where it takes longer to bind to the surface and the average time of the binding to the surface could be well resolved by our method. Because the microspheres are pressed against the

glass coverslip the thermal fluctuations in the vertical direction are severely constrained — the position of the bead fluctuates essentially along the two lateral directions. The kinetics of the binding can be then understood in terms of a two dimensional diffusion governed process. In section 4.2 we obtained an expression for the average time needed to bind, denoted by $\tau^{(2)}$, under similar circumstances. Since $\tau^{(2)}$ was measured we use the expression 4.30 in order to estimate the parameter y_1^2:

$$y_1^2 = \frac{r^2}{D^{(2)}\tau^{(2)}} \tag{7.10}$$

The parameter y_1 depends on the ratio $\xi = q/r$ where q is the size of an effective molecular reaction center and r is the size of the diffusion space for the molecules. Since biotinylated-BSA represents the molecule which reacts specifically with avidin coated microspheres, we can assume in the further discussion that ξ equals the average surface coverage ratio between biotinylated-BSA and BSA.

The diffusion constant $D^{(2)}$ is the same as that of a polystyrene microsphere because the diffusing molecules were immobilized on the polystyrene microsphere. When a microsphere is close to the surface the lateral diffusion coefficient decreases by a factor of 1/3 compared to its bulk value [29, 53]. The size of the diffusion space r is approximated as one standard deviation in the lateral position fluctuations of the trapped microsphere. With this approximation $r = 65nm$ and the equation 7.10 simplifies to:

$$y_1 = \sqrt{\frac{1.27}{\tau^{(2)}}} \tag{7.11}$$

In reference [1] this factor has been numerically evaluated for values of ξ in the range between $10^{-1} - 10^{-4}$.

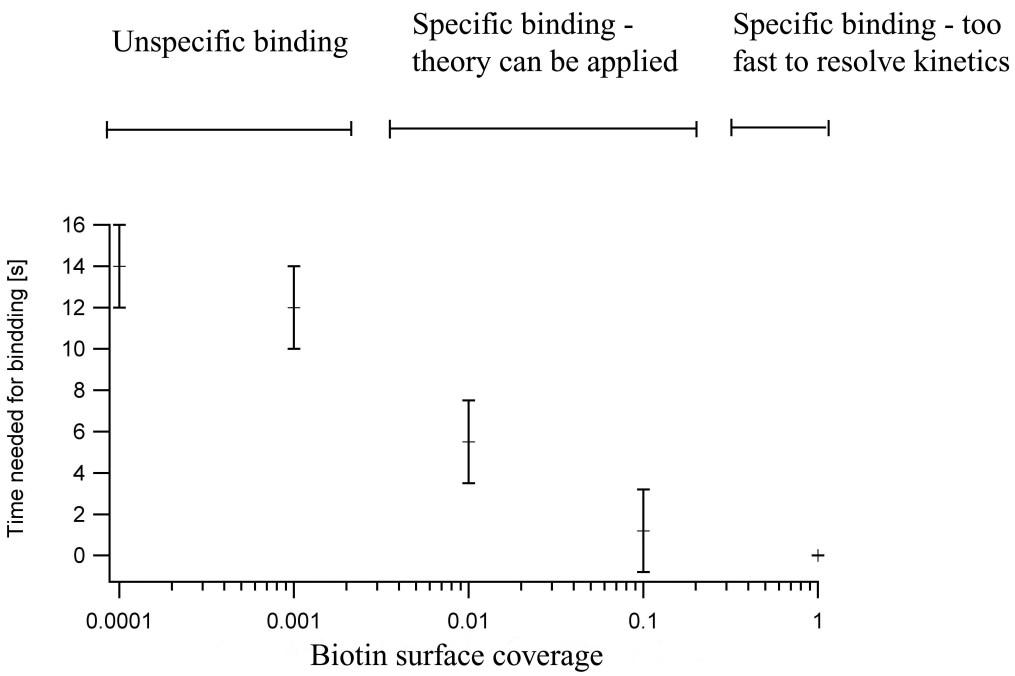

Figure 7.7: Time of the binding reaction as a function of the molecular surface coverage. Average time of a binding reaction has been measured for different surface coverages of biotin. The units of the biotin surface coverage refer to that fraction of BSA molecules which were functionalized with biotin. Surface coverage 1 implies that all BSA molecules contain biotin, whereas surface coverage 0 means that there was only pure BSA covering the surface. The results can be categorized into three groups: **(a)** When the surface is fully covered by biotinylated-BSA, the beads bind to the surface *immediately* after arriving into contact with it. Immediately means faster than the temporal resolution of 10 μs. **(b)** In the intermediary range of surface coverage between 0.1 - 0.2, there is a direct correlation between the average binding time and the molecular surface coverage. **(c)** When there is no biotinylated-BSA on the surface, i.e. surface coverage is 0, the average reaction time increases to approximately 14s.

The experimental results are shown in figure 7.7 and table 7.1 shows a comparison between theoretically estimated and measured values for $\tau^{(2)}$. The theoretical estimation agrees very well with the measured value for small values of ξ, i.e. $\xi = 0.1$. Since the radius of the diffusion space is $r = 65nm$ we obtain a value of $6.5nm$ for the size of the reactive molecule. This is slightly less than the size of an individual BSA molecule, with a deviation of several nanometers only. It is surprising that such a simple model predicts the size of an individual molecule so well. For lower values of ξ the deviation

Theoretically estimated $\tau^{(2)}_{theo}$	Measured $\tau^{(2)}_{exp}$	$\xi = q/r$
—	—	1
1.0s	$1.2 \pm 0.7s$	0.1
2.4s	$5.5 \pm 2.9s$	0.01
4.7s	$12.0 \pm 4.1s$	0.001

Table 7.1: Comparison of calculated and measured values for the average reaction time. The table shows a comparison of calculated and measured average reaction times $\tau^{(2)}_{theo}$ and $\tau^{(2)}_{exp}$ as a function of ξ. As explained in chapter 4.2 the parameter ξ is a measure for the relative size of the reactive molecule which is immobilized at the surface. When the surface is fully covered by biotinylated-BSA, i.e. surface coverage is 1, then the theoretical description becomes meaningless.

between the theoretical results and measurements becomes more apparent. The measured average binding times are underestimated by theoretical predictions. For lower biotinylated-BSA surface coverage ratios the probability of finding a reactive molecular center at the surface is significantly reduced. In this regime the non-specific interaction dominates the kinetics.

In summary, we were able to measure a correlation between the specific molecular surface coverage and the average time needed for the binding reaction. A model has been used to estimate the average binding time and compared to the measured values. The agreement is good for relatively high surface coverage of 0.1. From our model we were also able to estimate the size of an individual BSA molecule to 6.5nm, which agrees on the order of magnitude with the size of an individual BSA molecule as determined by x-ray crystallography.

7.1.5 Geometrical Amplification Effect

If the bead forms a *point-like* contact with the surface then the lateral position fluctuations decrease only slightly after the binding process. Hence, one can interpret the contact formation in terms of single molecular complex formation. There is one major experimental characteristic which defines such a condition. The two dimensional lateral position fluctuations have to be circularly symmetric in shape. The magnitude of these fluctuations is then essentially the measure for the combined length of the molecular complex which has formed under the bead. Because the position of the bead is fixed only at the point of contact with the surface, there is a magnification of small lateral fluctuations at the surface towards the lateral fluctuations of the center of the bead. This effect has been termed *the geometrical amplification effect*. It is discussed in detail later in this section.

However, there is a possibility that the bead which has already bound to the surface forms an additional molecular bond. If this is the case, then the lateral position fluctuations contain information about the distance between molecular complexes at the surface.

Essentially, small displacements on the order of molecular dimensions, $\geq 1\ nm$, at the surface of the bead are magnified through the size of the bead. The measured lateral position fluctuations of the center of the bead are much bigger than the lateral displacement at the surface (see figure 7.1.5a). The geometrical amplification effect offers a conceptual link between the magnitude of lateral position fluctuations and the length of the molecular complex.

In case of single bond formation, one would expect that lateral position fluctuations are circular symmetric in shape. From the maximum lateral position fluctuations it is possible to estimate the linker length. Let R be the bead radius, l the molecular linker length and $\triangle x$ the magnitude of lateral position fluctuations. Then there is a quadratic approximation relating the three parameters (see figure 7.1.5a).

$$(R + l)^2 - R^2 = \triangle x^2 \tag{7.12}$$

or:

$$\triangle x = \sqrt{2Rl + l^2} \tag{7.13}$$

In the performed experiments the radius was always one to two orders of magnitude bigger than the length of the molecular linker, i.e. $R >> l$. Thus,

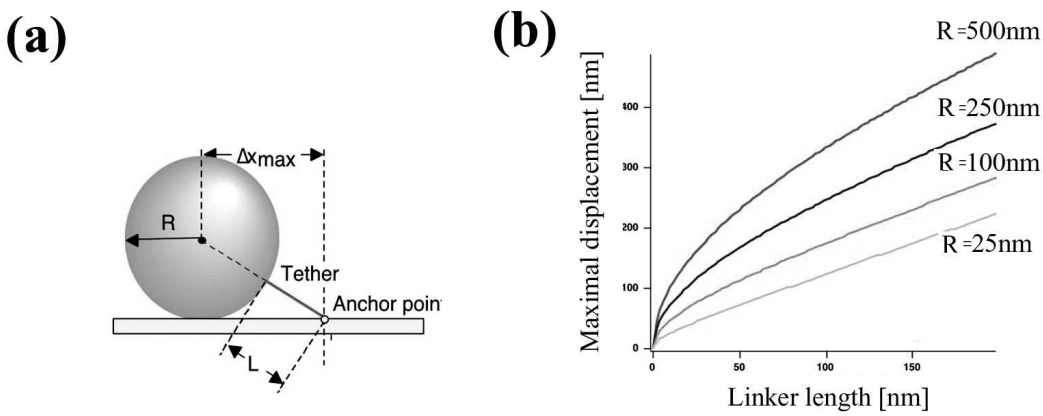

Figure 7.8: Geometrical amplification effect. (a) Lateral position fluctuations of the bead can be used to determine the length of the molecular complex between the surface of the bead and the glass surface. **(b)** Shows the maximal lateral displacement of a bound bead as a function of the linker length for different bead radii.

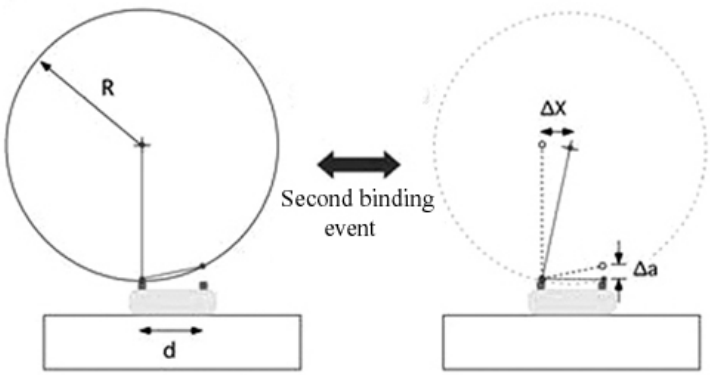

Figure 7.9: Multiple Binding. (a) The bead forms initially an individual molecular bond to the surface. Lateral position fluctuations of the bead can be used to estimate the length of the molecular complex between the surface of the bead and the glass surface. **(b)** If one contact has already been formed and the bead forms an additional molecular contact with the surface, then the distance between the two molecular complexes is $\langle x \rangle / 2$, where $\langle x \rangle$ is the average lateral displacement of the center of the bead due to the formation of the second molecular bond.

we obtain an approximate expression for l:

$$l \approx \frac{\triangle x^2}{2R} \tag{7.14}$$

The above discussion applies only to a bead which forms a single molecular contact with the surface. The experimental results showed that this is not always the case. Occasionally, the bead will form additional contacts which can be interpreted in terms of multiple bond formation. If multiple molecular bonds have been formed, one has to consider a slightly modified approximation in order to interpret the measured lateral position fluctuations. The situation is illustrated in figure 7.9. By assuming that two cotacts are formed by identical molecules, one can obtain the distance between the two molecular contacts at the surface as half of the lateral position displacement between the single-bound bead and the double-bound bead.

7.1.6 Mapping of individual binding sites

In this section I present a case for the feasibility of observing multiple individual molecular contacts with our experimental technique. Furthermore, this result is interpreted in terms of multiple binding sites on an individual protein.

The surface has been prepared according to the procedure for specific surface coverage as described in section 7.1.1. The bead was trapped and subsequently brought in a controlled manner into contact with the surface by displacing the optical focus. Figure 7.10 shows the 2-D lateral position fluctuations of a microsphere which was bound to the surface. The first binding event shows lateral position fluctuations with a circularly symmetric shape whereas the second binding event displays elliptic lateral position fluctuations as shown in figure 7.11.

In addition to the normal position fluctuations which occur on the fast time scale, there is a slower oscillation superposed. This very interesting effect of slow lateral position fluctuations of the center of the bead is attributed to the formation and rupture of an individual avidin-biotin bond. A graphical model for the formation and rupture of this individual molecular contact is shown in figure 7.12.

If the structure of the individual avidin molecule is explicitly taken into account we can estimate the distance between individual biotin binding sites

in the range between 4.5nm - 7.5nm. This distance is in accord with the size of an individual BSA molecule and we interpret the result in terms of multiple avidin-biotin bond formation on an individual BSA protein. To our knowledge this is the first observation of multiple individual binding sites located on a single protein. However, the individual binding sites could have been located on two neighboring BSA molecules. Although this is very improbable because of the high dilution of biotynilated-BSA at the surface, it cannot be excluded.

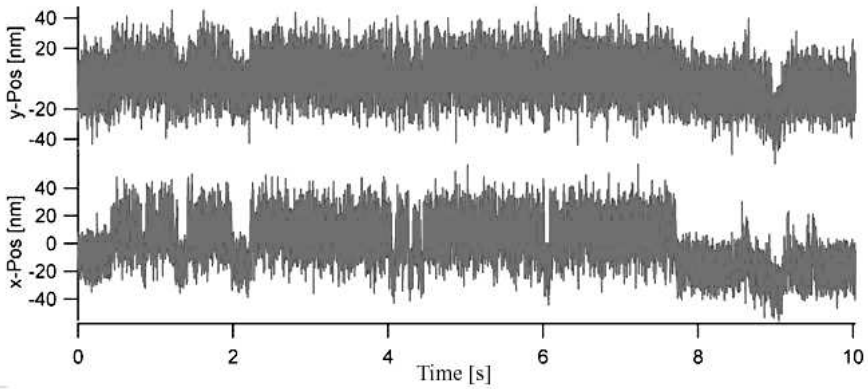

Figure 7.10: A surface bound bead is oscillating between two well defined states. The measured time series of lateral position fluctuations is shown. After the bead has bound to the surface a force was applied in the vertical direction. A surprising oscillation between two well defined states of the bead was observed. We interpret this observation in terms of multiple molecular bond formation.

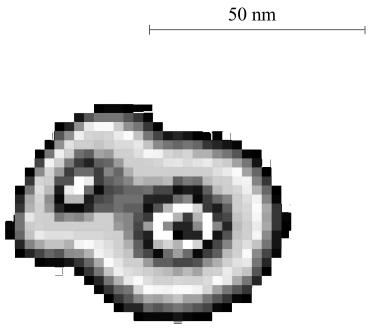

Figure 7.11: 2-D position fluctuation histogram for the oscillating surface bound microsphere. The lateral position fluctuations of a surface bound bead are shown as a 2-D histogram. By fitting a 2-D Gaussian profile to the curve it turns out that the circular symmetric position fluctuations are reduced by one half upon the formation of an additional bond-formation. This result strongly suggests that the two bound states are separated by an individual avidin-biotin bond.

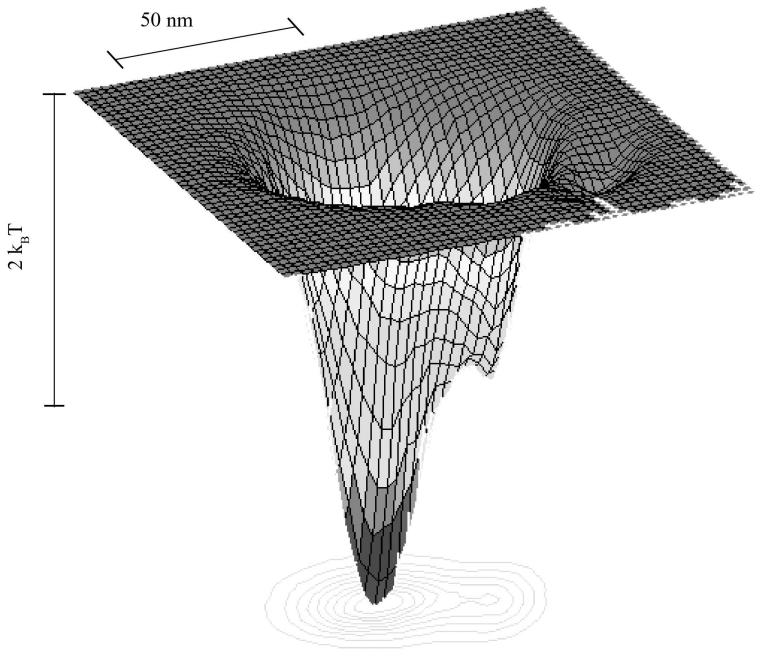

Figure 7.12: The energy landscape of a bound bead oscillating between two molecularly bound states. The lateral position fluctuation histogram is shown as a 3-D surface plot. The lateral axis corresponds to the position of the center of the bead and the vertical axis corresponds to the energy landscape.

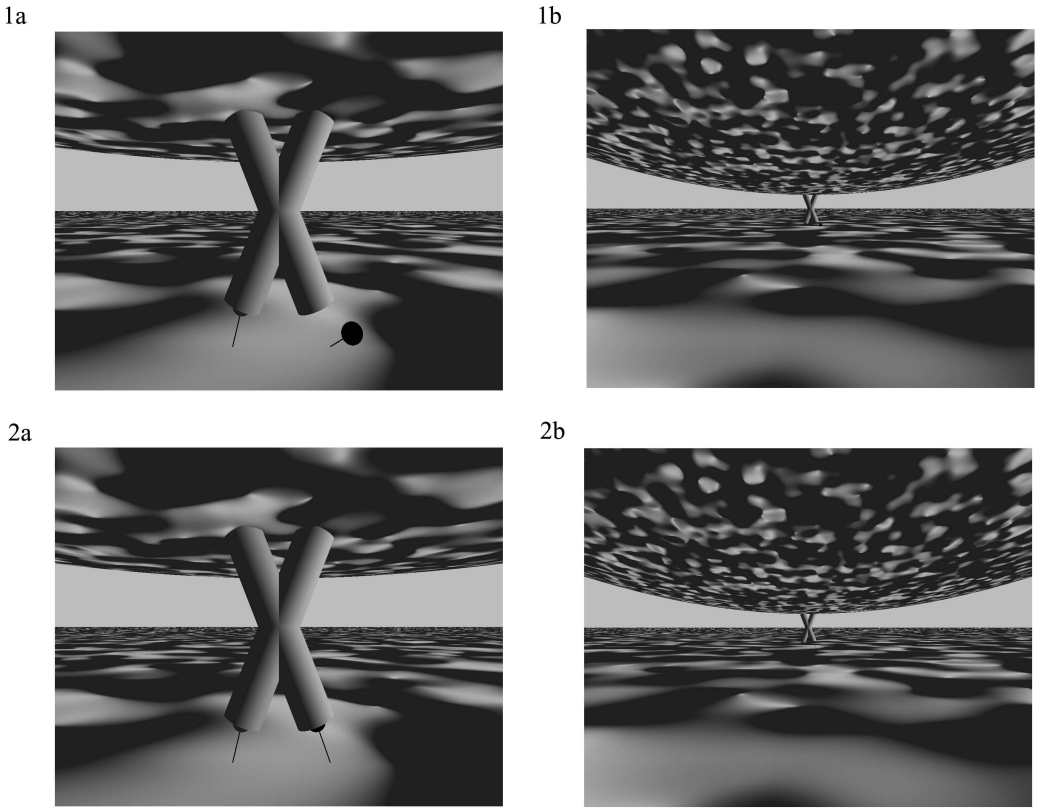

Figure 7.13: A graphical model for the formation of an individual molecular contact. Avidin is a tetramer whose monomeric subunits possess the structure of a β-barrel. More precisely, the structure of avidin molecule shows that the individual monomeric subunits intersect at an angle of $45°$. In order to reflect this structural feature, the avidin molecule is schematically represented by two intersecting cylinders which form together the letter X. Biotin molecule is represented by small black spheres. They are covalently attached to the BSA-coated surface by a linker which is shown as a black ribbon. The BSA-covered glass surface is shown as a black and white pattern without any periodic structure. The shading reflects the approximate roughness of the surface. This applies also to the polystyrene microsphere where avidin is covalently attached to its surface. Only an individual avidin molecule is shown in order to present the basic principle more clearly. Under realistic experimental circumstances the surface of the microsphere is densely covered by avidin molecules. **(1a)** An individual avidin-biotin bond was formed. **(1b)** The bead attached to the surface by the individual avidin-biotin bond is shown from a distant perspective. **(2a)** A double avidin-biotin bond was formed. **(2b)** The bead which is attached to the surface by two avidin-biotin bonds is shown from a distant perspective.

7.2 Elucidating the mechanism of SNARE complex formation

The SNARE complex is one of the essential molecular components during the membrane fusion [35]. Since the membrane fusion reaction is very complex and requires a simultaneous participation of several molecules it is not exactly clear what kind of molecular mechanism is responsible for the fusion. There is very good evidence that the SNARE complex can lower the energetic barrier of membrane fusion reaction. Possibly, this occurs by exerting mechanical force on the opposite layers while the complex is being formed. I have already introduced the hypothetical role of the SNARE complex during the membrane fusion process in section 3.6. Here, I will discuss in more detail the specifics concerning the architecture and function of the SNARE complex.

The SNARE complex consists of three proteins: Syntaxin (Sx), Synaptobrevin (Sbr) and SNAP-25. One of the major breakthroughs in the study of the SNARE complex came with the determination of the crystal structure of the SNARE complex by Sutton *et al.* in 1998 [61, 4]. The structure of this protein complex is shown in figure 7.14. It is a highly twisted and parallel four-helix bundle. More specifically, the structure of the complex shows a conserved leucine-zipper like motive at the center of the complex. Each individual protein from the SNARE complex displays a distinct secondary structure (see figure 7.14). Syntaxin and Synaptobrevin are completely α-helical. SNAP-25 consists of two α-helices which are connected by an unstructured loop. Furthermore, there is an ionic layer located also at the center of the complex. The structure of the SNARE complex differs from that of known virus membrane fusion proteins like haemagglutinin or HIV/SIV.

Sutton *et al.* [61] have also determined the surface charge density maps. It turns out that the surface is highly grooved with distinct hydrophilic, hydrophobic and charged regions (see Figure 7.15). Local charge densities of the protein are important for the membrane fusion as well as for the binding of other regulatory factors involved in neurotransmission.

The structural features of the complex have interesting implications for the mechanistic properties for SNAREs. Because the SNARE complex is a trimer, it is very unlikely that all three proteins would merge into the complex simultaneously. Instead, it would be reasonable to expect the complex formation in a couple of steps. A model has been proposed for the formation of the SNARE complex [61], which assumes several stages. First, a binary complex

is being formed between Syntaxin and SNAP-25 on the surface of the target membrane. Subsequently, synaptobrevin binds to the preformed binary complex. When the proteins coalesce into the four-helix bundle structure, there is a significant change in the electrostatic potentials of the SNARE complex (see Figure 7.15). This electrostatic potential may considerably affect the neighboring membrane bilayers and consequently the process of membrane fusion itself.

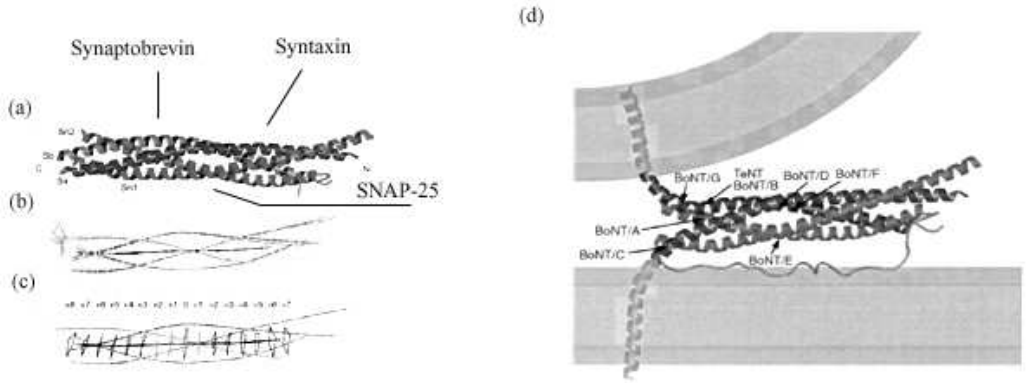

Figure 7.14: Structure of the SNARE complex. The illustration shows the structural organization of the SNARE complex. **(a)** Backbone drawing of the synaptic fusion complex. Syntaxin and Synaptobrevin display secondary structure in form of an α-helix. SNAP-25 consists of two α-helices. The three proteins form together a four-helix bundle. **(b)** Conformational variabilty. The residues show much less deviation in the middle of the complex as at the edges. **(c)** Organization of the SNARE complex. C_α atoms are shown as the bright traces, they are superimposed by the axis of local helices (Synaptobrevin, Syntaxin, SNAP-25). The superhelical axis is indicated by the dark traces. The numbers $0, \pm 1, \pm 2, \ldots$ refer to different layers. **(d)** The x-ray structure of the SNARE complex suggests that the molecular complex could generate mechanical force on the the opposing membranes during the membrane fusion process. Syntaxin and synaptobrevin are anchored into one of the opposing membranes by a transmembrane helix.

The knowledge of the exact reaction pathway of the SNARE complex is not yet well understood as discussed in section 3.6. It is impossible to infer about the exact energy landscape for the SNARE complex formation only from the structure of the protein, and the computational complexity for the problem is too large to be handled by current computer power. Therefore an experiment at the level of individual molecules can give new insights about

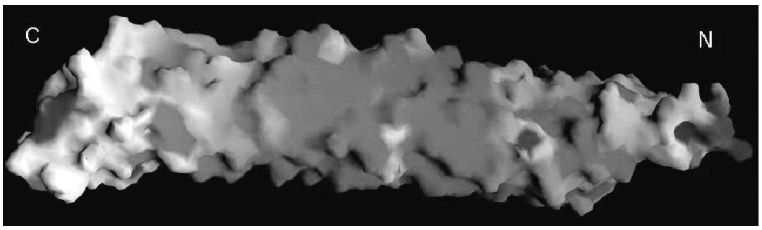

Figure 7.15: The surface charge distribution for the SNARE complex. The above surface plot shows the electrostatic charge distribution for a fully formed SNARE complex. The dark regions show areas of negative charges whereas the bright regions show areas of positive charges. Clearly, the positively charged regions are at the end of the complex, whereas the negatively charged regions are in the center of the synaptic fusion complex (SNARE).

the mechanism of SNARE-complex formation and improve our understanding of membrane fusion.

Fasshauer *et al.* [22] have recently reported from their studies concerning the thermodynamic properties of the SNARE complex. They concentrated on assembly and disassembly of the SNARE complex (see Figure 7.16). The reaction coordinates for assembly and disassembly pathways of the complex were defined either by urea concentration or by the temperature. The results were surprising because the complex exhibits a very pronounced hysteresis. The authors conclude that the kinetic pathways are very different for assembly and disassembly reaction, respectively. Furthermore, assembled and disassembled native states appear to be separated by a huge kinetic barrier which cannot be equilibrated on biological time scales. These data suggest that the process of SNARE-complex formation is very likely far away from the thermal equilibrium.

In summary, we can say that the pathway of SNARE complex formation remains an open question. It is directly related to our understanding of membrane fusion process in general. Whether the SNARE complex can generate even mechanical forces during the complex formation or not is a central question which was addressed in this work.

The experimental method, which was established with the avidin-biotin model system, as described in section 7.1, was applied to the study of mechanical properties of the SNARE complex. There are important similarities as well as differences between the two molecular systems, which are best reflected by the structure of the two molecular complexes. Avidin is a receptor

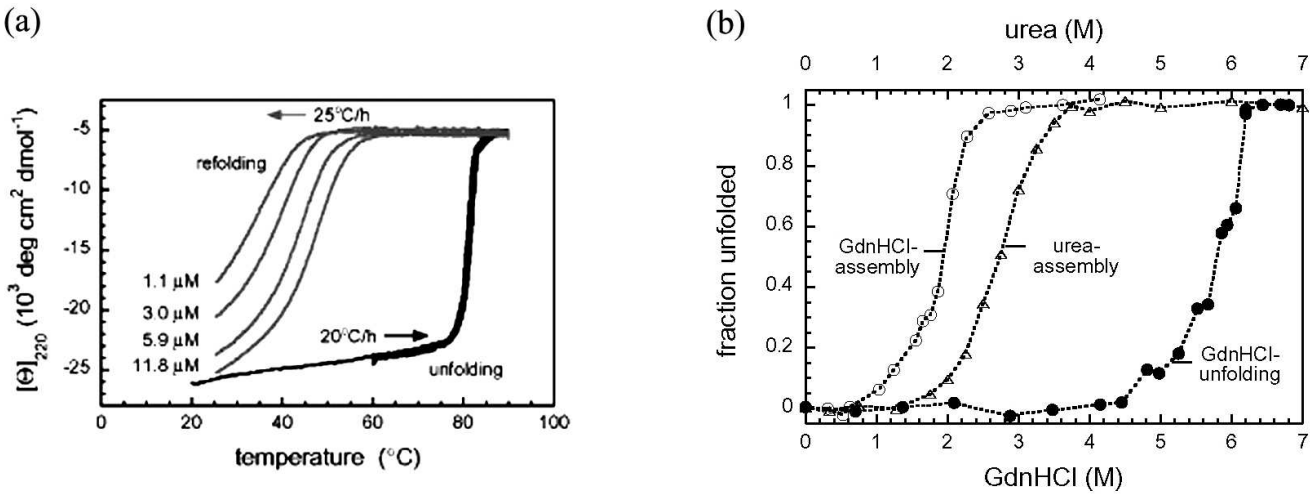

Figure 7.16: Thermodynamic properties of the SNARE complex. Disassembly and assembly of the synaptic SNARE complex show a very pronounced hysteresis. **(a)** Thermal unfolding of the SNARE complex monitored by CD spectroscopy at 220nm. The ellipticity θ is plotted against the temperature. Unfolding occurs at a very high temperature of $\approx 82°C$. Refolding has been controlled by a very slow temperature decrease. Refolding is dependent on the concentration of the protein. **(b)** The ellipticity θ was monitored at 220nm by CD spectroscopy. The independent parameter in this case was the concentration of the denaturant. The refolding rate was again concentration dependent.

molecule which is much larger in size than the ligand biotin. The SNARE-complex consists of three approximately equally sized proteins. Although the overall dimensions of both complexes in their respective native states are similar, the specific structural architecture reflects a different function of each protein-complex. The focus in this work was given to the detection of SNARE complex formation and the associated conformational changes.

7.2.1 Sample preparation

For several reasons, we had to modify the experimental assay used for avidin-biotin model system. The glass surfaces were covered with small gold particles measuring 5 nm in diameter and small amounts of BSA. Synaptobrevin (Sbr) was coupled covalently to the gold particles which were immobilized on the glass surface. Syntaxin (H3) was coupled covalently either to latex beads,

ranging from 200-1000 nm in diameter, or to the gold covered glass surface (see Figure 7.17). The coupling density on the beads was adjusted to yield approximately 1-3 molecules per $100\,nm^2$.

SNARE molecules had to be immobilized onto the beads and onto the glass surface. We developed a procedure, in collaboration with Olga Vites[1], whose purpose was to couple the molecules covalently to the respective surface. Since we expect large forces during the formation of this complex we had to eliminate the weakest point in the experimental assay by covalently coupling the molecules to the bead surface and to the glass surface. Synaptobrevin (Sbr1-96 97Cys) was coupled covalently to the bead surface. The glass surface was initially prepared with BSA and colloidal gold nanoparticles. This assay enabled coupling of both SNARE molecules, Synaptobrevin (Sbr) and Syntaxin (Sx), to the glass surface via a covalent bond to the gold particles. Since the gold particles measured only 5nm in diameter this ensured a very low probability that more than one SNARE molecule would bind to the gold particle. The experimental assay is illustrated in Figure 7.17. A more detailed description of the specific preparation procedure is given in appendix B.2.

With above defined experimental procedures we started to perform experiments involving different bead sizes. There are two critical effects which depend directly on the bead size. If the contact area between the bead and the glass surface is large, one can generally expect stronger non-specific interactions with the glass surface than in the case where the contact area is small. Therefore, we have finally chosen 200 nm beads for the experiments. The disadvantage of small beads consists in strongly reduced pulling force generated by optical tweezers. One can partially compensate for this effect by applying the forces laterally instead of axially.

The specific surface preparation led to slightly repulsive forces and in turn to a low probability of bond formation. It was necessary to scan the bead across a larger surface area before a binding event would occur. The low probability of binding is already a significant difference between the experimental assay with the SNARE molecules and other systems studied so far. It causes experimental problems in two different ways:

1. Specific and non-specific bond formation compete with each other.

[1] Olga Vites was working on her PhD project which is related to the study of the SNARE complex. She was working in the group of Reinhard Jahn from the Max-Planck Institute for Biophysical Chemistry in Göttingen.

2. Relatively slow kinetics of SNARE complex formation increases the probability of non-specific interactions.

Therefore the recording of statistically significant data is a very time consuming process with the current strategies.

7.2.2 Experimental results

After choosing latex beads with 200nm in diameter for generic experiments with SNARE molecules, we performed a series of experiments where the molecular surface coverage was varied in a systematic way. We classified the results in a quantitative way as shown in table 7.2. The observations are discussed in the following paragraphs.

We observed four different types of binding events (see table 7.2). At the one extreme the bead didn't bind at all, though it was several minutes in contact with the surface, at the other extreme it bound very tightly. Those cases where binding occurred could be classified roughly by the lateral bead fluctuations, although the distribution of these fluctuations was very broad. At the low spectrum of mechanical stiffness resulting from a formation of bond with the surface were those beads whose contact with the surface consisted rather of a tethering by a long elastic filament to the surface. This binding was clearly not the result of a molecular interaction with the surface caused by a formation of the SNARE complex. On the other side, there were cases where the bead bound to the surface and behaved as if the contact was formed by a single molecular bond. These situations resembled the specific binding in the avidin-biotin experiment. Unfortunately, due to limited unbinding statistics we couldn't notice any statistical differences in the mechanical properties of contacts among different experimental binding assays.

Since the data was statistically limited each individual time series of measured position fluctuations was investigated for details. If the formation of SNARE complex is a very specific process which can generate force, then one can investigate this reaction pathway also from an individual time series.

	No binding	Tethering	Small binding events	Bound beads ruptured by applying force	Irreversible binding
H3, Sbr, SNAP25	$\approx 50\%$		$> 75\%$	$< 15\%$	$> 75\%$
H3, Sbr	$50\% - 75\%$	$> 75\%$	$> 75\%$		$\approx 50\%$
H3, H3, SNAP25	$\approx 50\%$	$\approx 50\%$	$< 25\%$	$< 30\%$	$50\% - 75\%$
H3, H3	$\approx 50\%$	$\approx 50\%$	$< 30\%$	$< 15\%$	$50\% - 75\%$

Table 7.2: A quantitative classification of experimental results. Comparison between SNARE assays: The above table summarizes the results from the experiments performed with 200nm latex beads. Four different combinations of SNARE proteins have been immobilized on the gold covered glass surface and latex beads. They are shown in the column to the left. The top row indicates different binding events, which were observed during the experiments. The strength of the binding event is ascending from left to right. Smaller lateral position fluctuations imply stronger coupling of the bead to the surface. Percentages in the table show how many of the beads displayed a certain behavior. Blank spaces indicate that the specific phenomenon was not observed at all. The stiffness of the laser trap was set to maximum and was not varied during the experiments. Lateral trap constants were 2pN/m, the vertical trap constant was an order of magnitude lower 0.3pN/m. In a typical experiment the force exerted on the bead laterally by pulling was 1pN on a time scale of 1s.

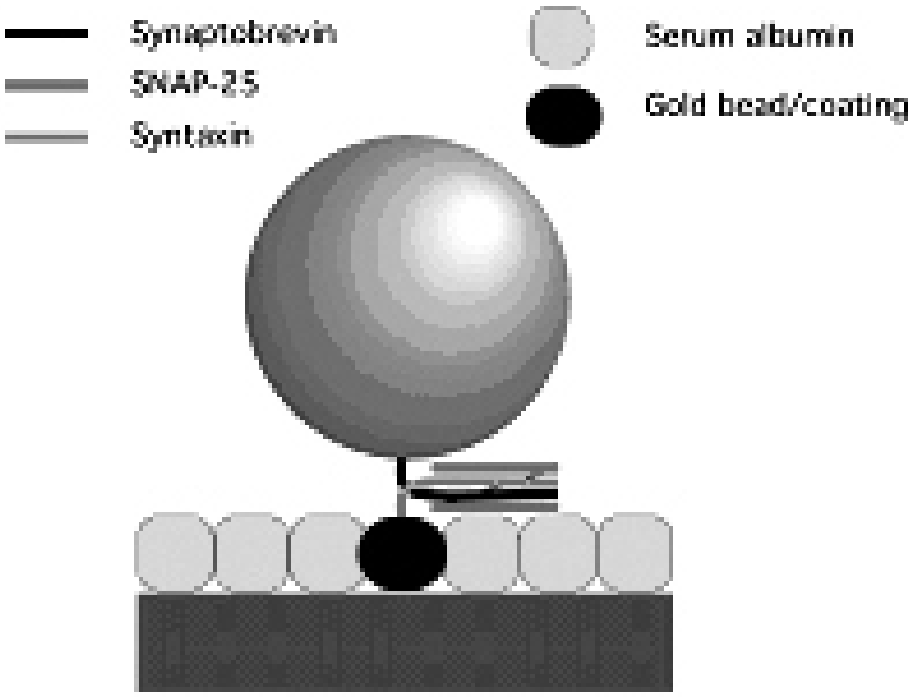

Figure 7.17: Experimental Assay for studying the mechanical properties of an individual SNARE complex. (a) The figure illustrates a generic molecular composition in the experimental assay involving SNARE molecules. The glass coverslip has been covered by gold nanoparticles measuring only 5nm in diameter. The surface has been in addition covered also by BSA in order to block off those spots which are causing unspecific interactions. The specific SNARE-molecules were then immobilized covalently on specifically prepared glass surface or beads.

7.2.3 Towards the observation of an individual SNARE complex formation

The results discussed in this section are very speculative. A very interesting effect was noticed specifically in the combination where H3 was coupled to beads and to the surface in the presence of SNAP-25. The binding process is phenomenologically distinguished from what has been observed in other SNARE assays. After binding, a relatively slow relaxation like process — of the order of seconds — pulls the bead towards the surface, despite the force that was applied to the complex (Fig. 6). It even continues after the force was released. Finally, the contact to the surface ruptured without external stress — a phenomenon we never observed in any other system. The length of the complex can be estimated from the lateral position fluctuations of the particle. According to these calculations, the complex reduces its length from more than 7 nm at first contact to less than 1 nm before the rupture event occurs. These data agree reasonably well with the expected structural dimensions and changes of the SNARE complex. The increasing asymmetry of the lateral position fluctuations during the complex formation was also expected, because the complex has to fit into the gap between the bead and the surface, which generates especially strong steric hindrance when the complex is fully assembled.

These are the first measurements that hint towards the proposed zipper like mechanism for the formation of the SNARE complex. The process seems to be continuous but surprisingly slow (second timescale), which is consistent with our observation that the probability for the formation of a SNARE complex is very small. The slow formation of the complex and the high forces involved, point towards a strong non-equilibrium process. This finding agrees well with recent thermodynamic data from Fasshauer et al. [22] and shows also that the reverse experiment, i.e. rupturing the formed complex by applying an external force, will not provide the forces that are generated during membrane fusion.

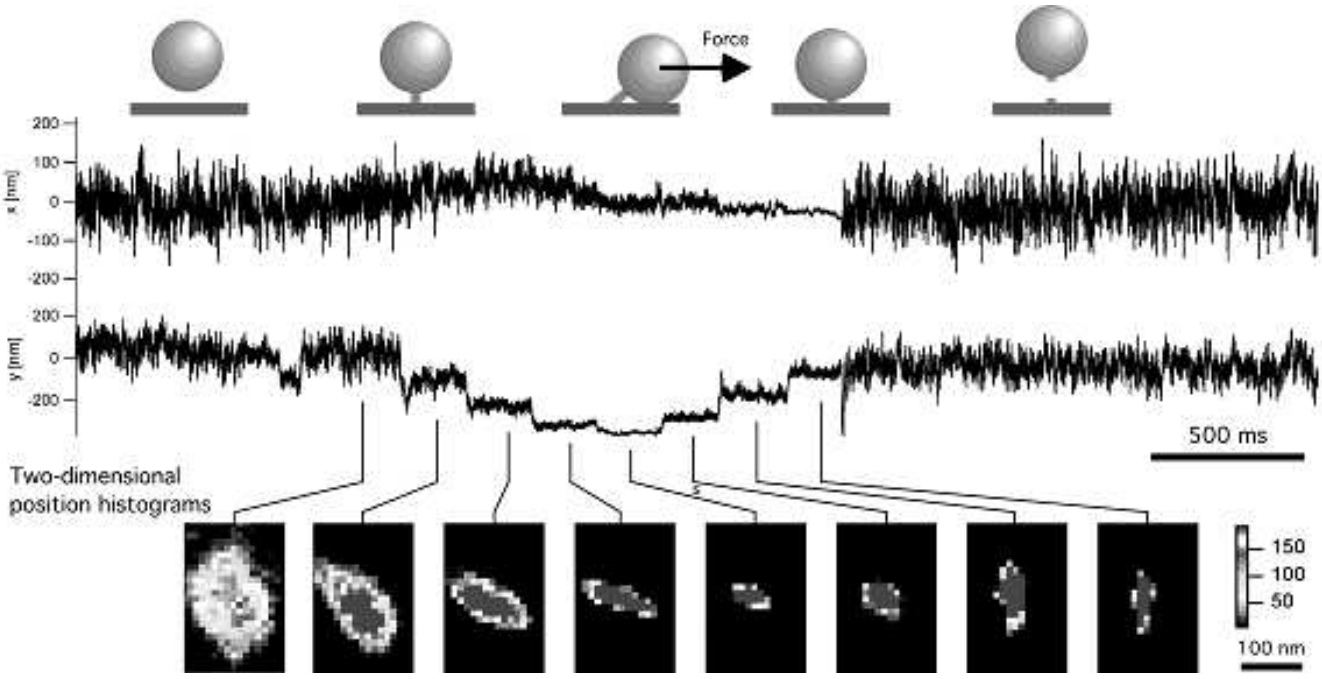

Figure 7.18: Formation of an individual SNARE complex. Dynamics of SNARE complex formation. H3 was coupled to beads and to the surface in the presence of SNAP-25. The above figure shows the center of lateral bead position fluctuations. After the binding of the bead to the surface, the sample was displaced laterally in 100 nm steps in order to apply a lateral force to the complex (see downward steps in the y-direction). This force was then released (upward steps). The histograms were calculated from the position data of each step as indicated.

Chapter 8

Summary and Discussion

The goal of the project was to develop a method to observe and manipulate the mechanical properties of individual small biomolecules under physiological conditions. Molecular model system of avidin-biotin was chosen in order to establish the experimental technique. This experimental technique was applied to the characterization of mechanical properties of individual SNARE-complex formation.

There are several technical constraints imposed on the experimental apparatus for experiments on individual molecules. First, the required precision of the position measurement is defined by the size of the biomolecule or biomolecular complex of interest. Since biomolecules measure from several nanometers to several tens of nanometers, the precision of position measurement has to be at least on the same length scale. Second, the resolution and the bandwidth of the measurement are constrained by the dynamics of molecular processes. A biomolecule is a part of an aqueous environment under physiological conditions. Therefore it is also subject to thermal fluctuations of this environment. Since biomolecules are in general well ordered three dimensional objects it is expected that the function of a molecule will manifest itself through a conformational change. Protein folding and protein-protein interactions are mainly governed by non-covalent interactions. Typical time scale for such a process can range from micro-seconds to minutes.

In this work we have chosen optical tweezers with a three dimensional interferometric position detection for experiments on individual biomolecules. There are several advantages of using this experimental setup. One can apply very small forces[1] to the biomolecule in a controlled manner. This reduces

[1]Small forces with respect to other experimental techniques like AFM or BFP.

the risk of damaging a biomolecule. Furthermore, the mechanical probes are optically trapped microspheres. The radius of a microsphere can range from several tens of nanometers to several tens of micrometers. For observation of the mechanical properties of individual molecules one should choose small microspheres in order to minimize unspecific interactions to the surface. This can provide direct access to the fast conformational changes in proteins and protein complexes. However, using small microspheres is disadvantageous in pulling experiments because the maximal pulling force is reduced. These considerations led us to use mainly polystyrene microspheres with radii in the range from 100nm to 500nm throughout the experiments.

In order to establish our experimental technique we needed a molecular model-system which had to be experimentally well characterized and mechanically robust. These requirements were best fulfilled by a molecular complex of ligand biotin and receptor avidin.

First, a binding assay was developed in order to obtain a faster feed-back about the molecular specificity of the surface. Biotin molecules were not immobilized directly onto the glass coverslip but were first attached covalently to BSA molecules. The biotinylated-BSA contained on average 8 biotin molecules per one BSA molecule and was subsequently immobilized onto the glass coverslip by adhesion. Avidin molecules were covalently attached to polystyrene microspheres in such a way that the surface was densely packed by avidin molecules. A solution of latex microspheres which were coated by avidin molecules was injected into the sample chamber. The number of bound fluorescent beads has been counted after well defined time intervals. It turned out that the molecular specificity of the binding was a time dependent quantity. Furthermore, the glass coverslips were prepared in such a way that a maximal specificity of 90% was achieved after 30 minutes of incubation with avidin-coated microspheres. For longer incubation times the influence of non-specific binding was becoming stronger. The molecular specificity of the binding disappeared entirely for incubation times of 2 hours and longer. This experiment clearly showed the time limitations and experimental constraints for performing molecularly specific experiments on individual molecules.

By solving the problem of preparing a molecularly specific surface our focus shifted towards a demonstration that the contact was due to individual molecules. An experiment with optical tweezers was developed to measure the average binding time of individual avidin coated microspheres to the biotin-BSA coated glass coverslips. We showed that there was a correlation between the average binding time and the specific surface coverage.

A theory for diffusion governed reactions was used to calculate the average binding times as a function of the size of the diffusion space and local molecular geometry. For low surface coverage in the range of 0.05 - 0.15 this theory is in good agreement with the measured values. By using this theory it was also possible to estimate the size of an effective molecular binding center to 7nm ± 3nm.

For lower surface coverage the theory underestimates the measured values. There are two reasons for this. First, the diffusion space of the molecularly covered microsphere is limited by the optical trap. By decreasing specific surface coverage also the probability of finding a specific molecule is decreased. Second, the non-specific interaction is not vanishingly small but has a finite value. Although the time scale of non-specific binding is several orders of magnitude smaller it becomes the dominating effect for surface coverages of less than 0.001.

The newly developed assay opened the way to more sophisticated experiments with individual molecules. An individual molecule can be used itself as a microscope. In analogy to an optical microscope where the light paths cross before a magnification is achieved, one can also use a molecule to magnify the molecular distance between individual binding sites at the surface. The specific molecular binding reaction at the level of individual molecules was also observed as a time series of forming and rupturing an individual molecular bond. In section 7.1.6 this was observed as an oscillation between two bound states of different stiffness. The first state could be characterized by circular symmetric lateral position fluctuations, whereas the second state showed elliptic position fluctuations. By using a simple geometrical amplification effect the length of the molecular linker was estimated to 0.5nm. This result is too small by an order of magnitude in comparison to the length of avidin-biotin complex. The size of a monomeric avidin unit as estimated by x-ray crystallography is approximately 7nm. The discrepancy between this two results disappears if the information about the detailed molecular structure of avidin is considered. Avidin is a tetramer whose monomeric subunits cross at an angle of 45°. When avidin molecule forms a second molecular bond to the surface the lateral position fluctuations are reduced only along one axis. The distance between the molecular binding sites on the surface was estimated in the range between 4.5 - 7.5 nm. This distance is of the same order of magnitude as the size of an individual BSA molecule. However, one cannot conclude with absolute certainty that the individual biotin binding sites were located on the same BSA molecule. If they were situated

on neighboring BSA molecules such a binding oscillatory behavior would still be possible. This experiment is a wonderful example of the relationship between the structure and the function of a molecule. The specific molecular architecture of avidin was used to magnify very small distances on the order of several nanometers between individual molecular binding sites.

In the second part we applied the above developed method to the study of protein-protein interaction. There were several reasons for choosing the SNARE complex for this study. This complex is among the best candidates to explain the molecular mechanism of membrane fusion. The structure of the complex has been solved prior to the beginning of the project. The complex is a trimer with a four-helix bundle like structure. The monomeric protein units which compose the complex are Syntaxin, Synaptobrevin and SNAP-25. A zipper-like mechanism for the formation of the complex has been suggested, which implies a conformational change on the order of several nanometers.

A new assay had to be developed for the molecularly specific surface functionalization. One species of SNARE monomers was covalently attached to small gold particles measuring only 5 nanometers in diameter. The gold particles were immobilized onto the glass surface by adhesion and also incubated with SNAP-25. The remaining molecular SNARE component was then covalently attached to the polystyrene microspheres. The final assay represented a compromise between the bead size and the maximal force generated on the bead. The smaller beads have a smaller contact area. The unspecific binding is therefore less frequent and weaker.

Since the specific molecular surface coverage was much lower than in the avidin-biotin assay we could not measure average binding times. The experiment was performed so that the bead was held in the vicinity of the glass surface by optical tweezers and rolled over the surface until a binding event occured. If there was no binding even after several minutes then the bead was discarded. Although the statistics of the experiments was very low we observed semi-quantitative differences among molecular assays. The percentage of ruptured contacts by force was with only one exception always below 15% of the total contacts formed. The SNARE complex is mechanically very stable. Higher than the maximal forces in our setup would be needed to obtain a statistically significant amount of ruptured contacts. However, our data do not contradict the proposed role for the SNAREs during the membrane fusion. On the contrary, the high mechanical stability suggests that the SNARE complex can in principle withstand very high mechanical forces.

Further experimental work with the SNAREs was focused on the direct observation of complex formation. Only microspheres with a radius of 100nm were used to ensure a very fast response time to the molecular conformational changes. The interactions between four SNARE components were tested. The binding of the beads to the surface could be classified according to the lateral position fluctuations. The sample size consisted of several tens of events in each experiment.

Because of the low statistics the position fluctuation measurements were analyzed individually. In the specific experiment, where syntaxin (H3) was coupled to the surface and to the beads, we noticed a completely new phenomenon. Such a phenomenon was observed neither in earlier experiments with avidin-biotin model system nor in experiments with other SNARE components. When the microsphere bound to the surface a lateral force was applied in an attempt to rupture the bond. The force was increased in discrete steps for approximately 1 second and subsequently decreased for 1 second again. On the contrary to our expectations, the final state significantly differed from the original one. The lateral position fluctuations decreased during this process, implying an increased mechanical coupling between the bead and the surface. The shape of the lateral position fluctuation histograms changed from circular symmetric to elliptic and was accompanied by a rotation. Since the result was unique it is rather difficult to draw any conclusions. A speculative interpretation of the result in terms of individual SNARE complex formation would imply that the complex can generate mechanical forces and is accompanied by a rotation.

Part IV

Appendices

Appendix A

Positioning system for the sample chamber

A.1 Queensgate scan table

Sample chamber and scanning table fulfill an important function in the experimental setup. The scanning table is used as a holder for the sample chamber. Therefore, the relative position of the sample chamber with respect to the optical trap is defined by the scanning table. Since the scanning table could be operated only in the lateral direction we implemented a PiFoc for the control of the axial position. A very accurate and stable positioning control is crucial for experiments on individual molecules. The purpose of this appendix is to explain how this was achieved in our experimental setup.

A scanning system with the lateral position resolution of better than 1nm was implemented. The movement of the scanning table is controlled by piezo elements. There is a major advantage in displacing the scanning table instead of the optical focus, because one does not have to interfere with the optical path of the laser beam. The table was connected to a three axis controller *NPS3330* from Queensgate Instruments. The controller was connected to a PC either via a normal serial RS232 port or via a fast parallel port.

The first step in an experiment with optical tweezers consists of trapping a microsphere. The concentration of microspheres in the fluid suspension is normally kept very low because one wants to minimize the probability of an additional sphere to pass in the vicinity of the laser focus for two reasons. First, a microsphere passing in the vicinity of the laser focus can distort the laser beam. Second, one wants to maintain a single microsphere in the op-

tical trap during the experiment. If there are multiple microspheres in the optical trap one cannot rely on the position detection system any longer. In practice this meant that the initial 1% solid solution of microspheres had to be diluted in the range between 200 times and 1000 times[1].

Optical tweezers experiments were performed in combination with standard confocal microscope (see section 6.1 figure 6.2). A differential interference contrast (DIC) optics was used to image suspended microspheres in aqueous solution. One possibility to trap a microsphere is to position the laser focus in aqueous solution and wait until a microsphere falls into the trap. If the concentration of microspheres is very low it takes a considerable amount of time to trap a microsphere. Therefore a computer controlled positioning of the scanning table would enable a *directed search* for a microsphere within the field of view[2] and also considerably speed up the trapping part of the experiment.

Initially, a procedure for direct control of the Queensgate scan table[3] was written in C programming language and implemented as an external operation into Igor software package[4]. This specific scanning table was chosen because of a positioning system with subnanometer precision. The resulting computer program was capable of controlling the scanning table in two modi: *discrete* and *continuous*. The discrete modus of operation enables positioning with subnanometer precision in well defined discrete steps. The great advantage of this modus is that one can run the controller either as a scanning device following a preprogrammed two dimensional path or as a realtime controlled interactive scanning device. The continuous mode can only follow a certain predefined path for a certain time interval. One can choose a function for each independent axis. There are several different functions at disposal: trigonometric, ramp, linear, etc ...

In order to trap the microsphere one needs the relative information about the position of the particle, the position coordinates are taken as input parameters for the above mentioned computer program.

Since the beads, which range from $100\,nm - 1\,\mu m$ in diameter, can be easily imaged by an optical microscope which is using DIC. The approximate position of a microsphere can be estimated directly from the DIC signal. A

[1]The microspheres were supplied by Molecular Probes, Inc.
[2]In our setup this field of view is approximately 60×40 microns.
[3]Scan Table NPS-XY-100A, Queensgate Instruments
[4]Igor version 4, Wavemetrics Inc.

CCD camera which is recording this signal is connected to the computer. In combination with the software it provides a real time picture of microspheres which are suspended in the sample. Since the area of the field of view is known to be 60×40 microns one can calibrate the total picture area to the same dimensions. The accuracy of this estimation should be on the order of the laser focus width, i.e. in the μm range.

Since the microspheres are suspended in an aqueous solution they diffuse. In order to dynamically capture a microsphere one needs a *realtime procedure* to follow the coordinates of a diffusing microsphere. This is achieved by using the coordinates of a computer mouse. The relative position coordinates are then supplied upon the mouse click on the input for the scanning table software.

Since the scanning table can be used only for the lateral position control it was necessary to introduce a PiFoc[5] for the control of the axial position of the laser trap. The position is controlled also by a piezo element, which causes a mechanical displacement in response to an applied voltage. The voltage control for the PiFoc was also programmed as a part of the above mentioned software package. The output from the computer was controlled by an AdWin board.

The objective lens is positioned onto the PiFoc. The position of the laser focus along the vertical axis is then controlled by displacing the objective lens with the PiFoc. The precision of this positioning system was on the nanometer length scale.

In summary, a system for computer directed position control of the scanning table was implemented. The control of the lateral position is achieved by the queensgate scanning table, which allows a subnanometer precision of the sample chamber placement. The position control along the vertical axis was achieved by placing the objective lens onto the PiFoc, which allows a precision of the position control on the nanometer length scale. Furthermore, a software routine was designed to automate the positioning of the sample chamber for fast trapping. Since the position of the microspheres can be monitored by the CCD camera, the coordinates of a microsphere were extracted directly from the camera display by using the computer mouse. These coordinates were used as the input for the positioning software. The response in position of the scanning table was in *real time*.

[5]Supplied by Physik Instrumente.

Appendix B

Specification of biochemical materials and preparation protocols

B.1 Chemical composition of a PBS buffer

PBS (1×)		
1l of buffer contains:		
	0.2 g	KCl
	0.2 g	KH_2PO_4
	1.15 g	Na_2HPO_4
	8 g	NaCl

Table B.1: This buffer was used during the experiments to mimic the physiological environment in the cell. There were no Ca^{2+} or Mg^{2+} ions in the buffer.

B.2 Preparation of the SNARE binding assay

This appendix describes in a detailed way the materials used during the preparation of the SNARE binding assay.

First, a sufficiently low concentration of the beads was determined. This was necessary in order to prevent the trapping of multiple beads during the experiment.

- The original bead concentration which contained 2% solids was diluted in the range from 1:10 - 1:100. The beads were supplied by Molecular Probes (2% solids, carboxylated groups COOH).

In order to couple Synaptobrevin (Sbr) to carboxylated latex beads, one had to modify the beads. This was achieved in several steps listed below:

1. $200\mu l$ of beads (2% solids) were washed in 50mM MES (buffer) at pH = 7.0 for approximately 20 minutes.
2. $50\mu l$ of 5× PDPH crosslinker at 5mM concentration was added in corresponding buffer.
3. $50\mu l$ of 5× EDC (5 mM concentration) was added in corresponding buffer.
4. Tween 20 surfactant at 0.1% concentration was added.
5. This mixture was left to rotate in an Eppendorf tube which was fixed on a small table for about 2h.
6. $10\mu\,l$ of 10× glycine were added at 100 mM concentration. The tube was left again to rotate for about 2 hours.

Before starting the incubation of the beads with the molecular components from the SNARE complex, the beads had to be washed:

- The beads were washed 3 times by 500 $\mu\,l$ 0.1% buffered solution of Tween 20.
- After the washing they were resuspended in 100 $\mu\,l$ of 50 mM buffered 0.2% Tween and 40 mM Glycine.
- The final volume of the solution with beads was $100\mu\,l$

After this preliminary treatment the beads were ready for the incubation with molecules from the SNARE complex. The following components were added to the $100\mu\,l$ of the above prepared suspension of beads:

1. 178 $\mu\,l$ of Sbr-Cys (Synaptobrevin with a Cys residue at the end) in PBS buffer at pH = 7.3. The concentration of Sbr molecules was 1.4 mg/ml. This lead to a final concentration of 0.25 mg/ml.

2. 200 $\mu\,l$ of BSA at a concentration of 5 mg/ml.

3. Finally, the beads were incubated either at $4°C$ overnight or at room temperature for 2 hours.

4. The beads were washed from the solution in the centrifuge

The second part of the surface coverage with SNARE molecules consisted of coupling the molecules specifically to the glass surface. A procedure was developed to cover glass coverslips with Synaptobrevin (Sbr) or Syntaxin (Sx). Cleaning of the glass coverslips was accomplished by following the same procedure which has already been developed for avidin-biotin model system as described in section 7.1.1. The protocol used functionalize clean glass coverslips with specific SNARE molecules was the following:

1. Clean glass coverslips were covered with droplets of 10% BSA (concentration of 0.2 mg/ml) which was diluted in buffered 1× PBS. Subsequently, the coverslips were placed into a humidistat. The incubation lasted for 2 hours at $37°C$ and 70% humidity.

2. The coverslips were taken out of the humidistat and washed with 1× PBS.

3. Colloidal gold particles were incubated. The paricles were measuring 5nm in diameter and were supplied by BBInternational. After droplets of colloidal gold were added onto the coverslip, they were let to incubate for 1 hour at $37°C$ and 70% humidity.

4. The coverslips were washed with 1× PBS.

5. Droplets of solutions containing Syntaxin (H3-Cys) or Synaptobrevin (Sb-Cys) were added onto the coverslip. This was followed by an incubation for two hours. The detailed conditions for the proteins were: $40\mu\,M$ in 50 mM Hepes buffer at pH = 7.0, 150 μM NaCl and 2M urea.

6. The coverslips were washed again by 1× PBS.

7. Blocking those parts of the surface which cause unspecific interactions by adding droplets of diluted BSA. BSA was diluted in 1× PBS with a ratio 1:10 respectively (10% BSA). The coverslips were put on a table which was rotating for 2 hours.

8. The coverslips were washed with 1× PBS.

Bibliography

[1] G. Adam and M. Delbrück. Reduction of dimensionality in biological diffusion processes. In Alexander Rich and Norman Davidson, editors, *Structural Chemistry and Molecular Biology*, pages 198–215. W.H. Freeman, San Francisco and London, 1968.

[2] B. Alberts, D. Bray, A. Johnson, J. Lewis, M. Raff, K. Roberts, and P. Walter. *Essential Cell Biology: An Introduction to the Molecular Biology of the Cell.* Garland Publishing Inc., New York, 1998.

[3] Miriam W. Allersma, Frederick Gittes, Michael J. deCastro, Russell J. Stewart, and Christoph F. Schmidt. Two-dimensional tracking of ncd motility by back focal plane interferometry. *Biophys J*, 74:1074 – 1085, 1998.

[4] W. Antonin, D. Fasshauer, Stefan Becker, R. Jahn, and Thomas R. Schneider. Crystal structure of the endosomal snare complex reveals common structural principles of all snares. *Nat Struct Biol*, 9(2):107–111, 2002.

[5] A. Ashkin. Acceleration and trapping of particles by radiation pressure. *Physical Review Letters*, 24:156–159, 1970.

[6] A. Ashkin. Optical trapping and manipulation of viruses and bacteria. *Science*, 235(4795):1517–1520, 1987.

[7] A. Ashkin, J.M. Dziedzic, J.E. Bjorkholm, and S. Chu. Observation of a single-beam gradient force optical trap for dielectric particles. *Optics Letters*, 11:288–290, 1986.

[8] Chunli Bai, Chen Wang, Sunney X. Xie, and Peter G. Wolynes. Single molecule physics and chemistry. *Proceedings of National Academy of Sciences*, 96:11075–11076, 1999.

[9] M. Balsera, S. Stepaniants, S. Izrailev, Y. Oono, and K. Schulten. Reconstructing potential energy functions from simulated force-induced unbinding processes. *Biophys J*, 73(3):1281–7, 1997.

[10] M.W. Berns, W.H. Wright, B.J. Tromberg, G.A. Profeta, J.J. Andrews, and R.J. Walter. Use of laser-induced optical force trap to study chromosome movement on the mitotic spindle. *Proceedings of National Academy of Sciences*, 86:7914–7918, 1989.

[11] G. Binnig, C.F. Quate, and C. Gerber. Atomic force microscope. *Physical Review Letters*, 56(9):930–933, 1986.

[12] A.S: Blawas, T.F. Oliver, M.C. Pirrung, and W.M. Reichert. Step-and-repeat photopatterning of protein features using caged-biotin-bsa: Characterization and resolution. *Langmuir*, 14(15):4243–4250, 1998.

[13] S.M. Block, D.F. Blair, and H.C. Berg. Compliance of bacterial flagella measured with optical tweezers. *Nature*, 338(6215):514–518, 1989.

[14] S.M. Block, L.S. Goldstein, and B.J. Schnapp. Bead movement by single kinesin molecules studied with optical tweezers. *Nature*, 348(6299):348–352, 1990.

[15] C. Branden and J. Tooze. *Introduction to Protein Structure*. Garland Publishing, Inc., 1991.

[16] Avijit Chakrabartty and Robert L. Baldwin. Stability of α-helices. *Advances in Protein Chemistry*, 46:141–176, 1995.

[17] P.C. Chaumet. Comment on "trapping force, force constant, and potential depths for dielectric spheres in the presence of spherical aberrations".

[18] T.E. Creighton. *Proteins*. Freeman, New York, 1993.

[19] W. Denk and W.W. Webb. Optical measurements of picometer displacements of transparent microscopic objects. *Applied Optics*, 29:2382–2391, 1990.

[20] E. Evans and K. Ritchie. Dynamic strength of molecular adhesion bonds. *Biophys J*, 72(4):1541–55, 1997.

[21] E. Evans, K. Ritchie, and R. Merkel. Sensitive force technique to probe molecular adhesion and structural linkages at biological interfaces. *Biophys J*, 68(6):2580–7, 1995.

[22] D. Fasshauer, W. Antonin, V. Subramaniam, and R. Jahn. Snare assembly and disassembly exhibit a pronounced hysteresis. *Nat Struct Biol*, 9:144–151, 2002.

[23] S. Fišinger. *Theoretische und experimentelle Analyse der spezifischen Seitenketten-Seitenketten Wechselwirkungen in der α-Helix. Eine Studie anhand der poly-Alanin basierten α-Helix.* Diploma thesis, Fakultät für Physik und Astronomie, Ruprecht-Karls Universität, Heidelberg, 1999.

[24] E. L. Florin, V. T. Moy, and H. E. Gaub. Adhesion forces between individual ligand-receptor pairs. *Science*, 264(5157):415–7, 1994.

[25] E. L. Florin, A. Pralle, J. K. Horber, and E. H. Stelzer. Photonic force microscope based on optical tweezers and two-photon excitation for biological applications. *J Struct Biol*, 119(2):202–11, 1997.

[26] Hans Frauenfelder, Peter G. Wolynes, and Robert H. Austin. Biological physics. *Reviews of Modern Physics*, 71(2):S419 – S430, 1999.

[27] Frederick Gittes and Christoph F. Schmidt, editors. *Signals and Noise in Micromechanical Measurements*, volume 55 of *Methods in Cell Biology*. Academic Press, 1998.

[28] Peter Hänggi, Peter Talkner, and Michal Borkovec. Reaction-rate theory: fifty years after kramers. *Reviews of Modern Physics*, 62(2):251–341, 1990.

[29] John Happel and Howard Brenner. *Low Reynolds Number Hydrodynamics*. Prentice-Hall International Series in the physical and chemical engineering sciences. Prentice-Hall, Inc., Englewood Cliffs, N.J., 1965.

[30] F.U. Hartl and M. Hayer-Hartl. Molecular chaperones in the cytosol: from nascent chain to folded protein. *Science*, 295:1852, 2002.

[31] W. Helfrich. Elastic properties of lipid bilayers: theory and possible experiments. *Z. Naturforsch C*, 28:693–703, 1973.

[32] Jacob Israelachvili. *Intermolecular & Surface Forces*. Academic Press, San Diego, 8th edition, 2000.

[33] S. Izrailev, S. Stepaniants, M. Balsera, Y. Oono, and K. Schulten. Molecular dynamics study of unbinding of the avidin-biotin complex. *Biophys J*, 72(4):1568–81, 1997.

[34] John David Jackson. *Klassische Elektrodynamik*. Walter de Gruyter, Berlin, New York, 2. verbesserte auflage edition, 1982.

[35] R. Jahn and H. Grubmüller. Membrane fusion. *Current Opinion in Cell Biology*, 14:488–495, 2002.

[36] J. Kozlovsky, L.V. Chernomordik, and M.M. Kozlov. Lipid intermediates in membrane fusion: Formation, structure, and decay of hemifusion diaphragm. *Biophys J*, 83(5):2634–2651, 2002.

[37] Y. Kozlovsky and M.M. Kozlov. Stalk model of membrane fusion: Solution of energy crisis. *Biophys J*, 82(2):882–895, 2002.

[38] R. Kubo, M. Toda, and N. Hashitsume. *Statistical Physics II*, volume II of *Springer Series in Solid-State Sciences*. Springer, Berlin, Heidelberg, second edition edition, 1998.

[39] Emmanuel Lacroix, Ana Rosa Viguera, and Luis Serrano. Elucidating the folding problem of α-helices: Local motifs, long-range electrostatics, ionic-strength dependence and prediction of nmr parameters. *Journal of Molecular Biology*, 284:173–191, 1998.

[40] C. Levinthal. Are there pathways to protein folding? *J. Chim. Physique*, 65:44–45, 1968.

[41] C. Levinthal. How to fold graciously? In P. Debrunner, J. C. M. Tsibris, and E. Münck, editors, *Mossbauer Spectroscopy in Biological Systems*. University of Illinois, Urbana, 1968.

[42] Oded Livnah, Edward A. Bayer, Meir Wilchek, and Sussman; Joel L. Three-dimensional structures of avidin and the avidin-biotin complex. *Proceedings of National Academy of Sciences*, 90:5076–5080, 1993.

[43] V.S. Markin and J.P. Albanesi. Membrane fusion: Stalk model revisited. *Biophys J*, 82(2):693–712, 2002.

[44] R. Merkel, P. Nassoy, A. Leung, K. Ritchie, and E. Evans. Energy landscapes of receptor-ligand bonds explored with dynamic force spectroscopy. *Nature*, 397(6714):50–3, 1999.

[45] W.E. Moerner. Examining nanoenvironments in solids on the scale of a single, isolated impurity molecule. *Science*, 265:46–53, 1994.

[46] W.E. Moerner and Michel Orrit. Illuminating single molecules in condensed matter. *Science*, 283:1670–1676, 1999.

[47] V. T. Moy, E. L. Florin, and H. E. Gaub. Intermolecular forces and energies between ligands and receptors. *Science*, 266(5183):257–9, 1994.

[48] Victor Munoz and Luis Serrano. Intrinsic secondary structure propensities of the amino acids, using statistical ϕ-ψ matrices: Comparison with experimental scales. *Proteins: Structure, Function, and Genetics*, 20:301–311, 1994.

[49] Victor Munoz and Luis Serrano. Elucidating the folding problem of helical peptides using empirical parameters. ii. helix macrodipole effects and rotational modification of the helical content of natural peptides. *Journal of Molecular Biology*, 245:275–296, 1995.

[50] Victor Munoz and Luis Serrano. Elucidating the folding problem of helical peptides using empirical parameters. *Journal of Molecular Biology*, 245:297–308, 1995.

[51] Victor Munoz and Luis Serrano. Development of the multiple sequence approximation within the agadir model of α-helix formation: Comparison with zimm-bragg and lifson-roig formalisms. *Biopolymers*, 41:495–509, 1997.

[52] V.S. Pande, A.Yu. Grosberg, and T. Tanaka. Heteropolymer freezing and design: Towards physical models of protein folding. *Reviews of Modern Physics*, 72(1):259–314, 2000.

[53] A. Pralle. *Physical properties of the plasma membrane studied by local probe techniques*. Phd, Ludwig-Maximilians Universität, München, 1999.

[54] M. Rief, M. Gautel, F. Oesterhelt, J. M. Fernandez, and H. E. Gaub. Reversible unfolding of individual titin immunoglobulin domains by afm. *Science*, 276(5315):1109–12, 1997.

[55] M. Rief, M. Gautel, A. Schemmel, and H. E. Gaub. The mechanical stability of immunoglobulin and fibronectin iii domains in the muscle protein titin measured by atomic force microscopy. *Biophys J*, 75(6):3008–14, 1998.

[56] A. Rohrbach. Reply to comment on "trapping force, force constant, and potential depths for dielectric spheres in the presence of spherical aberrations". *Private communication*.

[57] A. Rohrbach and E. H. Stelzer. Optical trapping of dielectric particles in arbitrary fields. *J Opt Soc Am A Opt Image Sci Vis*, 18(4):839–53, 2001.

[58] A. Rohrbach and E. H. Stelzer. Three-dimensional position detection of optically trapped dielectric particles. *Journal of Applied Physics*, 91(8):5474–5488, 2002.

[59] G. E. Schulz and R. H. Schirmer. *Principles of Protein Structure*. Springer Advanced Texts in Chemistry. Springer-Verlag New York Inc., Heidelberg, 1979.

[60] R.W. Steubing, S. Cheng, W.H. Wright, Y. Numajiri, and M.W. Berns. Laser induced cell fusion in combination wih optical tweezers: the laser cell fusion trap. *Cytometry*, 12:505–510, 1991.

[61] Bryan R. Sutton, Dirk Fasshauer, R. Jahn, and Axel T. Brunger. Crystal structure of a snare complex involved in synaptic exocytosis at 2.4 ä resolution. *Nature*, 395:347–353, 1998.

[62] K. Svoboda and S.M. Block. Biological applications of optical forces. *Ann. Rev. Biophys. Biomol. STruct.*, 23:247–285, 1994.

[63] K. Svoboda, C.F. Schmidt, B.J. Schnapp, and S.M. Block. Direct observation of kinesin stepping by optical trapping interferometry. *Nature*, 365(6448):721–727, 1993.

[64] Christian Tischer, Stephan Altmann, Samo Fisinger, H.K.J. Hörber, E.H.K. Stelzer, and E. L. Florin. Three-dimensional thermal noise imaging. *Applied Physics Letters*, 79(23):3878–3880, 2001.

Acknowledgement

My PhD thesis was performed in the group of Dr. E.H.K. Stelzer at EMBL.

In particular, I would like to thank Prof. Dr. E.-L. Florin for his supervision during the experimental phase and during the analytical phase of my PhD thesis.

I would like to thank Prof. Dr. B. Povh who has kindly accepted to present my PhD thesis to the Faculty of Physics and Astronomy at the University of Heidelberg.

I would like to thank Prof. Dr. Markus Sauer for refereeing my thesis.

I also thank to my parents for constant support and encouragement during my PhD.